

---

# **Balls, beams and blocks:**

**In situ observation of colloidal particles in  
confinement and under electron irradiation**

---

**Front cover:** A 3D representation of spherical and cubic particles surrounding an illuminated spot.

**Back cover:** ‘Yolk-shell’ particles (spherical particles enclosed by thin spherical shells), some of which are being illuminated. Illumination causes the particles to initially expand, followed by a continuous decrease in size. The particles closer to the center of the illuminated region show further advanced stages of this transformation.

PhD thesis, Utrecht University, the Netherlands, November 2017.

ISBN: 978-90-393-6885-5

Printed by Repro De Derde Schinkel

The work described in this thesis was performed in the Soft Condensed Matter group, part of the Debye Institute for Nanomaterials Science, at Utrecht University.

A digital version of this thesis is available at <https://colloid.nl/>

**Balls, beams and blocks:  
In situ observation of colloidal particles in  
confinement and under electron irradiation**

---

Ballen, bundels en blokken:  
In situ observatie van colloïdale deeltjes in  
begrensde ruimte en onder elektronenbestraling

(met een samenvatting in het Nederlands)

Proefschrift

ter verkrijging van de graad van doctor aan de Universiteit Utrecht op gezag van de rector magnificus, prof. dr. G. J. van der Zwaan, ingevolge het besluit van het college voor promoties in het openbaar te verdedigen op woensdag 22 november 2017 des middags te 12.45 uur

door

**Wessel Simon Vlug**

geboren op 23 september 1985 te Amsterdam

**Promotor:** Prof. dr. A. van Blaaderen  
**Copromotor:** Dr. ir. M. A. van Huis

This work is part of the research programme of the Foundation for Fundamental Research on Matter (FOM), which is part of the Netherlands Organisation for Scientific Research (NWO).

---

# Contents

---

<b>1</b>	<b>Introduction</b>	<b>1</b>
1.1	The colloidal domain . . . . .	2
1.2	Colloid interactions . . . . .	2
1.3	Colloidal particle materials . . . . .	4
1.3.1	Stöber silica . . . . .	4
1.4	Microscopy . . . . .	6
1.4.1	Electron microscopy . . . . .	7
1.4.2	Liquid cell electron microscopy . . . . .	8
1.4.3	Electron beam induced effects . . . . .	9
1.5	Thesis outline . . . . .	10
<b>2</b>	<b>Synthesis of uncoated silica particles for studies of index-matched long-range repulsive systems</b>	<b>13</b>
2.1	Introduction . . . . .	14
2.1.1	Colloidal particles and interactions . . . . .	14
2.1.2	Charged particles in a gravitational field . . . . .	15
2.1.3	Radial distribution function and pair potential . . . . .	16
2.1.4	Materials for colloidal particles . . . . .	17
2.2	Experimental . . . . .	19
2.2.1	Chemicals . . . . .	19
2.2.2	Particle synthesis . . . . .	19
2.2.3	Solvent transfer . . . . .	21
2.2.4	Confocal microscopy and particle tracking . . . . .	22
2.2.5	Microelectrophoresis . . . . .	24
2.3	Results and discussion . . . . .	24
2.3.1	Particle synthesis . . . . .	25
2.3.2	Solvent transfer . . . . .	26
2.3.3	Confocal microscopy and particle tracking . . . . .	27
2.3.4	Microelectrophoresis . . . . .	32
2.4	Conclusions and outlook . . . . .	33
2.5	Acknowledgments . . . . .	34

<b>3</b>	<b>Synthesis of oppositely charged colloidal silica and yolk-shell particles</b>	<b>35</b>
3.1	Introduction . . . . .	36
3.1.1	Stöber silica structure . . . . .	37
3.1.2	Etching of Stöber silica . . . . .	38
3.2	Experimental Section . . . . .	39
3.2.1	Chemicals . . . . .	39
3.2.2	Particle synthesis . . . . .	40
3.2.3	HF etching . . . . .	42
3.2.4	NaOH etching . . . . .	42
3.2.5	Particle characterization . . . . .	43
3.3	Results and Discussion . . . . .	43
3.3.1	Synthesis . . . . .	43
3.3.2	HF etching experiments . . . . .	50
3.3.3	Base etching . . . . .	61
3.3.4	Combined etching . . . . .	62
3.3.5	Water etching . . . . .	64
3.4	Conclusions . . . . .	64
3.5	Acknowledgments . . . . .	65
3.6	Appendix: HF concentration . . . . .	66
<b>4</b>	<b>Diffusion of colloidal particles in spherical shells</b>	<b>67</b>
4.1	Introduction . . . . .	68
4.1.1	Diffusion, hydrodynamic drag and confinement . . . . .	69
4.1.2	Electrostatic interactions . . . . .	71
4.2	Methods . . . . .	73
4.2.1	Microelectrophoresis . . . . .	73
4.2.2	Solvent conductivity, salt concentration and Debye screening length . . . . .	74
4.2.3	Particle tracking . . . . .	74
4.3	Results and discussion . . . . .	75
4.3.1	Particle synthesis and etching . . . . .	76
4.3.2	Zeta potential measurements . . . . .	78
4.3.3	Confocal measurements and particle tracking . . . . .	80
4.4	Conclusions and outlook . . . . .	87
4.5	Acknowledgments . . . . .	88
<b>5</b>	<b>Beam induced dissolution of silica in Liquid Cell Scanning Transmission Electron Microscopy</b>	<b>89</b>
5.1	Introduction . . . . .	90
5.1.1	Silica structure and electron irradiation effects . . . . .	91
5.2	Experimental . . . . .	94
5.2.1	Particle synthesis . . . . .	94
5.2.2	TEM liquid cell assembly . . . . .	94
5.2.3	STEM measurements . . . . .	95
5.3	Results and discussion . . . . .	95

5.3.1	Electron beam induced changes to particle size of silica shells and enclosed spheres . . . . .	95
5.3.2	Effect of dose rate . . . . .	101
5.3.3	Effect of flow rate . . . . .	102
5.3.4	Particle elongation in the scanning direction . . . . .	103
5.4	Conclusions and outlook . . . . .	107
5.5	Acknowledgments . . . . .	109
5.6	Supporting Information . . . . .	109
<b>6</b>	<b>Hydration of MgO Nanocrystals to <math>\alpha</math>-Mg(OH)<sub>2</sub> Monitored at Ambient Pressure by In Situ TEM</b>	<b>111</b>
6.1	Introduction . . . . .	112
6.2	Experimental . . . . .	115
6.3	Results . . . . .	116
6.4	Discussion . . . . .	122
6.4.1	Electron beam activation . . . . .	122
6.4.2	Effect of Relative Humidity . . . . .	123
6.4.3	Formation of amorphous Mg(OH) <sub>2</sub> . . . . .	123
6.4.4	Reaction mechanism . . . . .	123
6.5	Conclusion . . . . .	126
6.6	Acknowledgments . . . . .	127
6.7	Supporting Information . . . . .	127
	<b>References</b>	<b>129</b>
	<b>Summary</b>	<b>145</b>
	<b>Samenvatting</b>	<b>149</b>
	<b>Acknowledgments</b>	<b>153</b>
	<b>List of publications</b>	<b>159</b>
	<b>About the author</b>	<b>161</b>



# 1

---

## Introduction

---

In this introductory chapter, I describe the necessary background to understand the topics that are discussed in later chapters. I define what colloidal particles are, what makes them interesting, why they are convenient as model systems, and the predominant ways through which they interact with one another. Additionally, the basics and general procedure of the Stöber method are explained, as nearly all the particles that were investigated and are described in this thesis were synthesized using this method. I also made use of a relatively new technique whereby liquid specimens can be observed in the electron microscope. Therefore, this technique is described, followed by some of the known implications of irradiating a liquid sample with an electron beam. Finally, a brief overview of the other chapters of the thesis is presented.

## 1.1 The colloidal domain

Matter comes in a variety of sizes, and some of the properties of materials are affected by their dimensions. As a result, nanomaterials are commonly separated into different categories based on their size. One such category is the colloidal scale, ranging from approximately 10 to 1000 nm (the IUPAC defines it from one to 1000 nm<sup>1</sup>). Under 10 nm, quantum effects such as quantum confinement and tunneling become apparent or even dominant, while particles that are larger can (usually) be described classically. Molecules from the medium in which the nanoparticles are dispersed impart energy to the nanoparticles through collisions, which is proportional to the temperature. This allows the particles to diffuse,<sup>2</sup> arrange in ordered structures and display rich phase behavior.<sup>3</sup> However, when particles become too large, they can no longer be significantly affected by thermal fluctuations at temperatures and timescales typical to humans, i.e. close to room temperature and on the order of minutes. Thus, between these two approximate borders lies the colloidal domain; a range where matter is large enough that it behaves classically, while still small enough for thermal fluctuations to be sufficient to probe available thermodynamic states and reach equilibrium. The ability to explore and change configurations means that colloidal particles exhibit thermodynamic quantities such as free energy and entropy, similar to atomic systems.<sup>4</sup> However, as colloids are much larger, they can be observed directly in real space with visible light and their dynamics are slower such that they occur on human timescales. Additionally, the properties of colloids are less restricted than those of atoms. For example, colloidal size and charge can be changed gradually, whereas those of atoms are fixed.<sup>5</sup> This makes colloidal particles excellent model systems for the study of fundamental properties of matter. Moreover, particles in the colloidal size range have numerous technological applications, such as paints, coatings, optical switches, cancer treatments, and are abundantly present in food.

## 1.2 Colloid interactions

Colloidal particles can interact with each other in a variety of ways. The most common interactions are steric, van der Waals, and electrostatic interactions. The steric interactions, or excluded volume interactions, describes the repulsion between particles when they begin to overlap. This interaction is very short ranged, only becoming important when particles physically touch, although long polymer chains grafted on the surface of particles can extend the range considerably. Van der Waals forces arise from fluctuating dipoles. The strength of the interaction depends on the difference in refractive index between the particles and the medium. When considering two identical particles, this interaction is always attractive. If

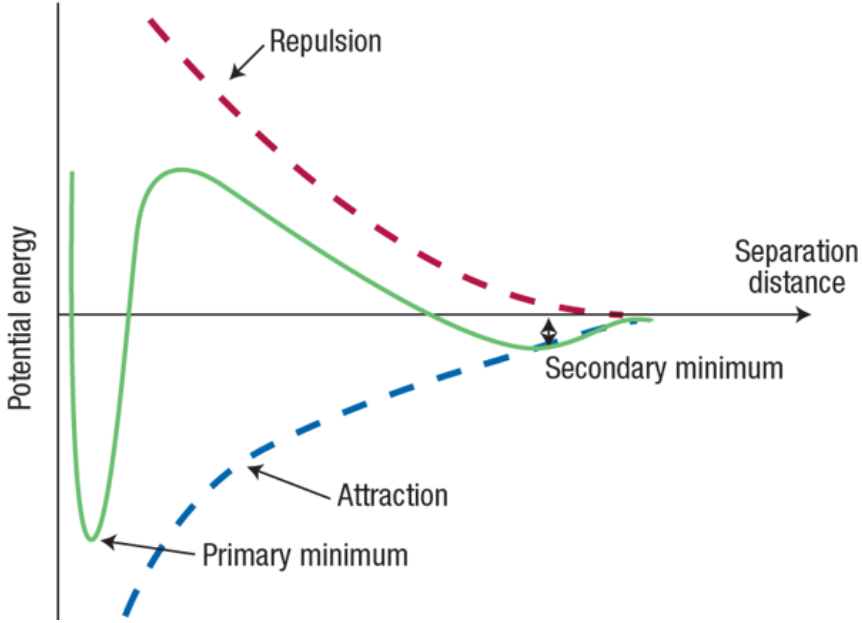


Figure 1.1: DLVO potential as a function of interparticle distance. The sum of the van der Waals attraction and electrostatic repulsion gives rise to two potential energy minima separated by an energy barrier. Taken from Ref. [6].

particles are dispersed in a medium with the same refractive index, called ‘index matching,’ then the van der Waals force vanishes. Finally, particles can (and usually do) carry a net charge. For identical particles, the charge will result in a repulsion. In vacuum, this interaction energy decays proportional to the inverse distance between the charged particles:  $1/r$ .

However, in a liquid medium with ions, the potential between the particles is screened by ions in the solution, resulting in an additional exponential decay characterized by the Debye screening length,  $\kappa^{-1}$ . In this case, the potential between the particles,  $V_{ij}$ , can be accurately described using DLVO theory,<sup>5</sup> named after two pairs of scientists who independently reported it (Derjaguin and Landau, and Verwey and Overbeek<sup>7,8</sup>):

$$\frac{V_{ij}}{k_{\text{B}}T} = Q_i Q_j \lambda_{\text{B}} \frac{e^{\kappa(a_i + a_j)}}{(1 + \kappa a_i)(1 + \kappa a_j)} \frac{e^{-\kappa r}}{r}, \quad (1.1)$$

where  $k_{\text{B}}$  is the Boltzmann constant,  $T$  is the absolute temperature (K),  $Q$  is the number of charges on the particle,  $i$  and  $j$  denote the different particles,  $\lambda_{\text{B}}$  is the Bjerrum length (m),  $a$  is the particle radius (m), and  $r$  is the distance between the centers of the particles (m). Full DLVO theory takes into account van der Waals attraction and electrostatic repulsion. However, these attractions can be eliminated by index matching,

as stated above, leaving only the repulsive electrostatic contribution. In general, the particles attract one another at close distances due to the van der Waals forces, resulting in a steep energy minimum called the ‘primary minimum.’ Conversely, the weaker and longer ranged electrostatic repulsion acts to prevent the particles from coming in close proximity of one another. This combination can result in an energy barrier and the formation of a second energy minimum at larger separation, as shown in Figure 1.1. If the energy barrier is sufficient, then the particles will not be able to overcome it and they will be kept at a distance from each other. However, if the electrostatic repulsion is weak, e.g. by addition of ions, then the particles can cross the barrier and reach the primary minimum. At this point, they become stuck together at close proximity: they have aggregated.

## 1.3 Colloidal particle materials

Colloidal particles can be composed of a great variety of materials. The most common materials are plastics, such as polystyrene<sup>9</sup> and polymethylmethacrylate (PMMA),<sup>10,11</sup> oxides such as silica<sup>12</sup> and titania,<sup>13,14</sup> and hydrogels such as poly(*N*-isopropylacrylamide) (pNIPAM).<sup>15</sup> Each material offers different advantages. For example, PMMA can be dispersed in a medium in which it is simultaneously refractive index matched and density matched, eliminating van der Waals forces and gravity. Silica is stable and inert, has excellent thermal and chemical resistance and is mechanically strong. The colloidal particles that were synthesized for this thesis were all made of a particular type of silica: Stöber silica. Below, the synthesis procedure of Stöber silica will be described.

### 1.3.1 Stöber silica

Stöber, Fink and Bohn were the first to publish the synthesis of silica particles from an alkoxy silane catalyzed by ammonia in alcoholic solution, resulting in spherical silica particles.<sup>16</sup> Silica synthesized in this manner is now commonly referred to as ‘Stöber silica.’ This method utilizes an alkoxy silane (usually tetraethoxysilane) in ethanol and ammonia. In the Stöber process, there is an initial nucleation stage where particles are formed, followed by a phase in which the particles are grown to larger sizes.

The nucleation phase starts with the production of reactive monomers from the silica-precursors. For this, the alkoxy-arms of the silica-precursor are hydrolyzed, consuming a water molecule and yielding an alcohol (usually ethanol or methanol) and a silanol (Si-OH) group (see Figure 1.2A). Silanol groups can react with one another in a condensation reaction which produces a water molecule and a Si-O-Si bond, called a siloxane bond, as shown in Figure 1.2B. This process can be repeated multiple times, leading

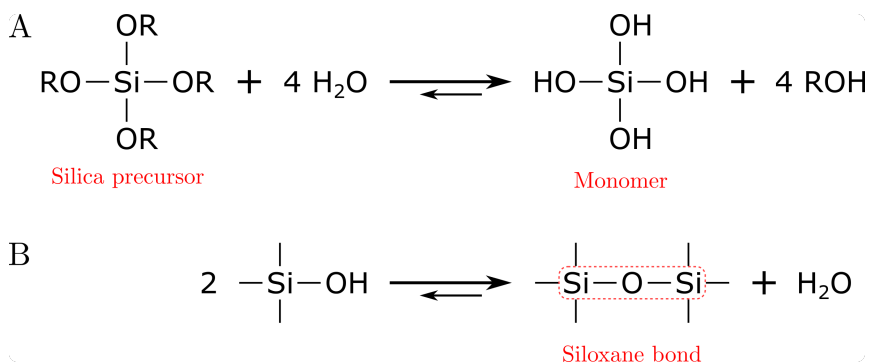


Figure 1.2: **A**: Hydrolysis of alkoxy silane precursor molecules leading to the formation of monomers, and **B**: their condensation resulting in siloxane bonds which make up the structure of silica. The three other bonds on the silicon atom are left unspecified for simplicity.

to the formation of (densely) interconnected chains of alternating silicon and oxygen atoms. Therefore, silicon atoms in solution with one or more OH groups are considered monomers in a polymerization reaction. Both reactions (hydrolysis and condensation) are catalyzed by both acid and base.<sup>17,18</sup> Additionally, the reaction rate is influenced by the size of the alkyl chain: the smaller the alkyl chain, the faster the reaction.

During Stöber synthesis, particles go through several stages, as shown in Figure 1.3. In the initial stage, monomers react with one another and form poorly connected oligomeric clusters. Above a certain size ( $r_{col}$ ), these clusters become thermodynamically unstable and collapse, expelling the solvent from their interior and forming dense, compact particles.<sup>19–21</sup> Subsequently, these collapsed particles grow in size by further addition of monomers, clusters, and other dense particles until they reach another critical size: the point at which they become electrostatically stable ( $r_{stab}$ ). At this size, the electrostatic repulsion on the growing particles is large enough that they are prevented from closely approaching and attaching to one another.<sup>22</sup> As a consequence, they grow individually by addition of monomers and (collapsed) clusters alongside the other stable particles instead of collectively aggregating. The size at which the particles become electrostatically stable is influenced by the ionic strength, the pH of the solution and the particle charge, which in turn is affected by the degree to which the particle is crosslinked and has chargeable groups available. Because of these effects, the final particle size depends on the specific experimental conditions. By changing the pH of the growth solution, the ionic strength, the dielectric constant of the solvent (type of alcohol) and/or the temperature, the final particle size can be tuned (to a degree).

In order for a new stable particle to be formed, it must grow to  $r_{stab}$  without encountering and attaching to an already stable particle during

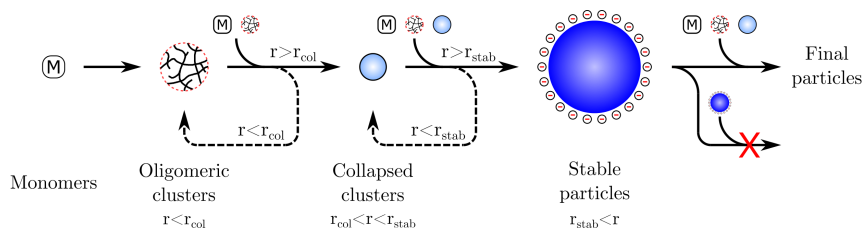


Figure 1.3: Schematic representation of the Stöber process, adapted from Ref. [19]. Precursor monomers polymerize to form clusters, which collapse to dense particles at a critical size,  $r_{col}$ . Monomers, clusters and collapsed clusters continue to aggregate and polymerize until a size is reached where they are electrostatically stable,  $r_{stab}$ , after which these particles only grow by the addition of monomers and (collapsed) clusters, but not with other stable particles.

the growth process. Therefore, the probability of forming a new stable particle is affected by the monomer concentration (which drives the growth to  $r_{stab}$ ) and the concentration of particles which are already stable (which results in loss of the growing particle due to it being incorporated). As the reaction proceeds, the concentration of stable particles rises, progressively making the formation of more new stable particles less probable. Additionally, the concentration of monomers decreases gradually because the silica-precursor is added all at once at the beginning of the reaction.<sup>23</sup> In this way, the generation of new particles is self-limiting and the nucleation stage of the reaction automatically comes to an end. During the subsequent growth stage, particles grow by the addition of monomers and clusters to their surface. Larger particles require more material in order to grow, but this is exactly balanced by the increased probability of encountering the larger surface area of larger particles. This means that particle growth is independent of particle size.<sup>24</sup> Because stable particles are only formed in a brief period of time and then continuously grow independent of particle size, the distribution of particle size can be very narrow, typically a few percent.

## 1.4 Microscopy

Colloidal particles can be directly observed using a microscope. One of the advantages of using colloids is that they are large enough to be observed through an optical microscope, where light passes through the sample and a system of lenses magnifies the image. In several chapters of this thesis, we used confocal laser scanning microscopy to image the particles and their motion. In confocal microscopy, a small pinhole in the focal plane blocks out-of-focus light. As a result, only a thin section of the sample

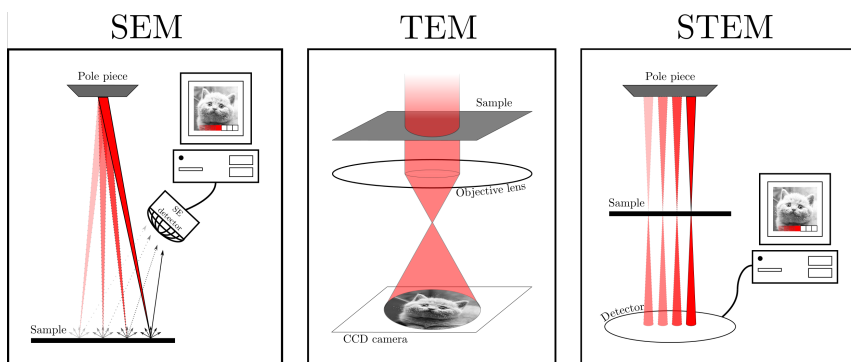


Figure 1.4: Schematic representation of the different modes in electron microscopy, scanning (SEM), transmission (TEM), and scanning transmission (STEM). The lenses of the condenser and imaging systems are not shown.

contributes to the image. By incorporating a fluorescent dye into our sample and exciting it with a laser, the background signal can be greatly reduced. The combination of these two factors (optical sectioning and fluorescent labels) allows for high signal-to-noise images to be obtained at much better resolution. Additionally, by moving the sample and acquiring sequential images at different depths, three dimensional ‘image stacks’ can be recorded.

However, instead of using light, other types of waves can be used to do microscopy. One such alternative is using high-energy electrons in electron microscopy. Several chapters in this thesis make extensive use of electron microscopy. Therefore, in the next section we will discuss this technique, how we extended it to study liquid specimens, and we also address some complications caused by the electron beam.

### 1.4.1 Electron microscopy

There are several advantages of using electrons instead of light. Most notably, the wavelength of high-energy electrons is much smaller than that of light ( $\sim 3$  pm at 200 kV), allowing for much higher resolution, and electrons can interact in different ways with matter and can therefore generate various kinds of signals different from intensity contrast and fluorescence. However, the use of electrons also comes with considerable disadvantages, primarily due to the strong interactions with matter and high absorption. One of the consequences of these strong interactions is the requirement that the microscope column must be kept at high-vacuum, as the beam would otherwise be completely absorbed before reaching the sample. Additionally, the samples must be very thin in order for electrons to pass through at all, and the samples are easily damaged by the electron beam. Despite these limitations, electron microscopy is an incredibly powerful tool for the

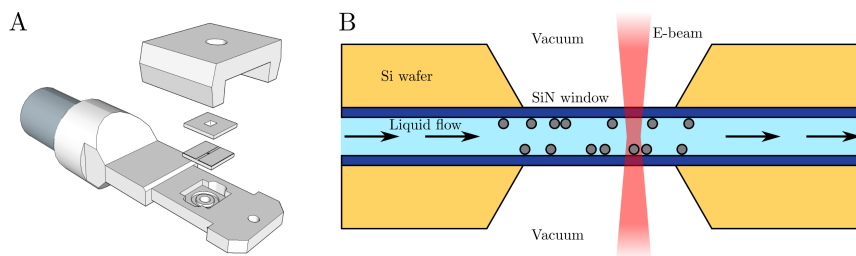


Figure 1.5: Schematic representation of the liquid cell holder for the electron microscope. **A:** The tip of the holder, showing the silicon chips. **B:** a side view of the cell once it has been closed. The SiN membranes separate the sample from the vacuum while liquid can flow through the cell and the electron beam can pass through.

characterization of nanomaterials. It combines imaging of materials with atomic resolution, determination of crystal structure by electron diffraction, probing of energy states, spectroscopy, and even elemental mapping.

There are three types of electron microscopy, schematically illustrated in Figure 1.4: scanning (SEM), transmission (TEM), and scanning transmission (STEM). In SEM, the electron beam is scanned over the sample, recording one pixel at a time and building up an image piecemeal. Due to the use of relatively low acceleration voltages (0.5-30 kV) it only collects signal from the sample surface, yielding topological information. TEM is similar to traditional film projectors; the electron beam travels through the sample and creates a shadow image, which can be captured on a screen or detector. In order for the beam to penetrate through the sample, the acceleration voltage in TEM is significantly higher (100-300 kV), which has the added benefit of increased resolution. A series of lenses are used to magnify the transmitted image (not shown in the illustration). STEM, as the name implies, combines the previous two methods. The electron beam is focused to a point - as small as possible - and is scanned across the sample. The intensity of the transmitted beam is recorded and used to build up an image. Besides the intensity of the transmitted beam there are various other ways of recording images that make use of other beam-sample interactions. However, we will not go into these techniques because they were not used in this thesis.

### 1.4.2 Liquid cell electron microscopy

For a long time, the high-vacuum required for the electron beam also implied that samples had to be subjected to (and compatible with) these conditions. However, in recent years it has become possible to image thin *liquid* samples in the TEM.<sup>25,26</sup> Thanks to advances in microfabrication technology, thin SiN membranes can be made that are strong enough to withstand the difference in pressure between ambient conditions and the

column vacuum while remaining thin enough to allow the electron beam to pass through virtually unperturbed.<sup>27</sup> In this sense, they are aptly referred to as ‘windows’ since they prevent mass from getting through, but allow radiation to pass. Typically, these membranes are 50 nm thick and offer a viewing area of 50x200  $\mu\text{m}$ . By placing two of these windows on top of one another, a thin section in between them can be created that is separated from the column vacuum on both sides while still allowing the electron beam to pass through and form an image, schematically shown in Figure 1.5. In this way, specimens in specific gaseous atmospheres<sup>28</sup> and in liquids<sup>29,30</sup> can be studied in the electron microscope. This setup also allows for liquid flow through the sample holder and in between the windows, and for the viewing area to be heated (using a platinum wire) or electrically biased.

### 1.4.3 Electron beam induced effects

In optical microscopy, a beam of light passes through the specimen and leaves it mostly unaffected, thus visualizing the sample’s native behavior without disruption. Unfortunately, the electron beam is not such an innocent bystander, particularly when liquid specimens are concerned. There are various ways in which electrons can damage the specimen, such as ionization, excitation, and breaking of chemical bonds.<sup>31</sup> Moreover, in the case of liquid cell electron microscopy, the liquid that surrounds the sample is also affected by the electron beam. Electron irradiation of water, for example, is known to generate a whole range of reactive ions, radicals and hydrated electrons which may also affect the sample.<sup>32</sup> Sometimes this can be used as an advantage, using the electron beam to locally induce certain changes or reactions, controlling where and when they occur. However, while there may be occasions where beam effects can be employed usefully, it is also important to attempt to eliminate the perturbing influence of the electron beam. To this end, the effects of the electron beam on the sample must be studied and understood so that phenomena purely intrinsic to the sample can be fully explored. Being able to study (liquid) specimens without changing their behavior will allow for their fundamental dynamics to be laid bare and deepen our understanding of the processes that govern nanoparticle behavior under ‘normal’ conditions and to compare them to *ex situ* experiments. It is therefore crucial to study the sample at various intensities of the electron beam (expressed as ‘dose rate’) in order to separate the beam-related phenomena from the intrinsic behavior of the sample.

## 1.5 Thesis outline

The topics that are covered in this thesis are somewhat broad, yet they are all related to imaging small particles and attempts at extending the observable range to include nanoparticles, in some cases with unexpected outcomes. The observation of nanoparticles is made more difficult by the fact that when particles become smaller than the point spread function of the microscope, the signals from neighboring particles overlap, thus preventing the reliable identification of individual particles. In this thesis, we study different particle systems and attempt to circumvent the aforementioned problem in several ways. We synthesize and characterize particles that strongly repel one another over a large distance, thus maintaining a distance of multiple particle diameters between them and preventing their signals from overlapping, even if scaled down to the nanoparticle range. We also synthesize and study a spherical particle inside a shell, guaranteeing a minimum distance between the particles and we investigate the effect of the shell wall on the inner particle. Finally, we employ electron microscopy, which has much higher resolution (smaller point spread function), to study oxide particles in liquid water and water vapor. However, in the presence of water, the electron beam profoundly influences the behavior of the particles. We briefly outline below how each following chapter contributes to these topics.

In **chapter 2**, we utilize colloidal particles and study their interactions using confocal (optical) microscopy, observing collections of particles that can be distinguished individually. We study the behavior of long-range repulsive spherical silica colloids in the low-polar solvent cyclohexyl chloride (CHC) in order to extend the formation of large structures to using smaller particles. Due to the much longer range of the interactions compared to the particle size, the interparticle distance is much larger than a particle's diameter. Such separations will also allow for small nanoparticles to be imaged individually. We describe a new method to transfer the particles to CHC that does not require the particle surface to be coated with apolar molecules. The particle charge is determined in several different ways, both for particles that are recently synthesized and after the particles are aged for over a year. The commonly used Stöber synthesis is modified in **chapter 3** to synthesize silica particles containing a large quantity of organic groups. Silica with a large organic content is preferentially removed by etching with hydrofluoric acid (HF) solution, leaving the purely inorganic silica mostly unaffected. By making particles with an organically doped layer in between a pure silica core and outer shell, and subsequently etching the particles with HF solution, we are able to synthesize 'yolk-shell' particles: a small sphere inside a much larger shell. Particle morphology and charge are monitored as the particles are etched with HF solution, demonstrating differences in etching behavior between single spherical particles and dumbbells related to differences in the structure of the outer silica shell. The yolk-shell particles synthesized in chapter

3 are imaged using confocal microscopy in **chapter 4**. These particles are identified and tracked in time using computer code, allowing for the analysis of particle movement. The surrounding shell affects the motion of the core particle hydrodynamically and electrostatically. We study these two effects by observing the movement of the particle at different salt concentrations. Additionally, we investigate the influence of the proximity of the core particle to the shell on the diffusivity. In **chapter 5**, yolk-shell particles are imaged using liquid cell electron microscopy. The yolk-shell particles are synthesized in a similar way to those used in chapter 3 and 4 and are completely densified by high temperature treatment. Exposure to the electron beam results in transformation and dissolution of the silica, leading to an initial swelling of the shell followed by a gradual shrinkage. Interestingly, the shell retains its shape during these transformations. The observed changes to the particles are related to the internal particle structure, the material density, the availability of water, and the strength of the electron beam. Finally, we investigate the influence of the electron beam on a different oxide, MgO, using in situ electron microscopy in **chapter 6**. We study the conversion of crystalline MgO to amorphous MgOH<sub>2</sub> by reaction with water vapor. The dependence on the electron beam is investigated and a mechanism for the conversion reaction is proposed.



# 2

---

## Synthesis of uncoated silica particles for studies of index-matched long-range repulsive systems

---

In this chapter, we study fluorescent silica spheres suspended in the low-polar ( $\epsilon = 7.6$ ) solvent cyclohexyl chloride (CHC). By deionizing the solvent, the repulsive Yukawa potential between the particles can be made long ranged, resulting in several particle diameters of separation between particles. We present a new method for transferring silica colloids from ethanol to CHC that avoids particle aggregation, keeps the ionic strength low and does not require a coating on the particles. This method utilizes a liquid monomer, trimethylolpropane ethoxylate triacrylate (ETPTA), which can be polymerized using a photo-initiator and UV light. We determine the particle charge for three volume fractions in various ways using confocal microscopy and microelectrophoresis. Additionally, we find that the particle charge is considerably reduced after the particles have been stored in ethanol for 35 months.

## 2.1 Introduction

### 2.1.1 Colloidal particles and interactions

There is great diversity in the materials in the world around us, and in their properties. An important parameter that influences the properties and behavior of (particulate) matter is its size, and the discovery of these size-dependent effects and influences has led to the development of (nano)particles with improved properties, or new combinations thereof.<sup>33,34</sup> Below  $\sim 10$  nm, quantum mechanical effects begin to dictate particle properties. Beyond the micrometer scale lies the granular regime, where thermal fluctuations no longer allow the particles to explore other configurations. In between these two regimes resides the colloidal domain; a range where particles are large enough that they can be described classically, yet small enough that thermal fluctuations allow for equilibration and the exploration of available states. Materials composed of these colloidal particles are commonplace, from consumer products such as food and cosmetics to technological applications such as paints, coatings, and oil recovery enhancers. Aside from their wide applicability, colloids are also commonly used as models for atomic systems for studying phase behavior, owing to their tunability and because they can be observed in real space and on human time scales.<sup>11,35,36</sup>

Colloidal particles interact with each other in several ways, primarily through steric, van der Waals, and electrostatic interactions. Steric forces prevent particles from overlapping and are short ranged, only coming into play when particles touch. Sometimes, polymers and short oligomers are grafted onto the particle surface, resulting in a steric interaction range from a few nanometers to tens of nanometers depending on the size of the macromolecule.<sup>37</sup> Van der Waals forces are somewhat longer ranged and are always attractive between identical particles. The magnitude depends on the difference between the particle's index of refraction and that of the surrounding solvent.<sup>38</sup> Finally, electrostatic forces arise from charge on the particles, and can be very long ranged. The range of electrostatic interactions depends predominantly on the concentration of ions in the solution. These ions 'screen' the charge, effectively hiding the electric field, and making the interaction shorter ranged. As a result of the screening, the interaction decays exponentially, characterized by the Debye screening length,  $\kappa^{-1}$ :

$$\kappa^{-1} = (8\pi\rho_{\text{ion}}\lambda_{\text{B}})^{-1/2} \quad (2.1)$$

where  $\rho_{\text{ion}}$  is the number density of ions ( $\text{m}^{-3}$ ) and  $\lambda_{\text{B}}$  is the Bjerrum length. Solutions can be prepared that contain almost no ions, resulting in a slow decay of the electrostatic repulsion.<sup>39</sup> In systems with such low ionic strength, called the 'long range repulsive' regime, particles interact with one another over long distances, even over  $10 \mu\text{m}$  (i.e. many particle diameters). One of the consequences of such a long ranged interaction is that the potential between the particles is 'soft', meaning that it varies

gradually, as opposed to sudden increases or decreases in free energy. A second implication is that particles will be kept far apart, and that shorter ranged interactions can be neglected. Electrostatic and van der Waals interactions are combined in DLVO theory, named after two pairs of researchers who described it independently of each other: Derjaguin and Landau, and Verwey, and Overbeek.<sup>7,8</sup>

### 2.1.2 Charged particles in a gravitational field

Over a century ago, Perrin and Einstein used the study of colloidal particles settling under the influence of gravity to unravel Brownian motion and the molecular nature of matter. Since then, colloidal particles in a gravitational field have been studied extensively, yielding sometimes counterintuitive results.<sup>40,41</sup> In particular, the sedimentation of charged particles that are surrounded by a cloud of counterions. The interplay between gravity (pulling the particles to the bottom), the entropy of the ions (striving for a homogeneous distribution of ions), and electrostatics (favoring counterions close to the particles to satisfy local charge neutrality) can cause an unintuitive effect called ‘entropic lift.’<sup>42,43</sup> If the salt concentration is high, then the fraction of ions required to balance the colloid charge is small and therefore the concentration is still mostly homogeneous. However, when the total ion concentration is low, the fraction of ions required to counter balance the accumulated charge of the particles in the bottom becomes significant and the partitioning of the ions then becomes entropically unfavorable. This can be resolved by either dispersing the particles more homogeneously through the medium (i.e. not all on the bottom) or by developing an electric field between the bottom and the top of the dispersion (sacrificing local charge neutrality). This effect has been observed experimentally<sup>44,45</sup> and has been explored using computer simulations.<sup>46</sup> The theory set out by van Roij<sup>43</sup> results in three distinct sedimentation regimes, using a dimensionless particle density,  $y$ :

$$y = 24\phi \frac{Q\lambda_B}{a} \frac{1}{(\kappa a)^2}, \quad (2.2)$$

where  $\phi$  is the volume fraction,  $Q$  is the number of charges on the particle, and  $a$  is the particle diameter. This dimensionless particle density combines the relevant parameters (volume fraction, particle charge and screening length) into a single parameter. Over its entire range,  $y$  can be divided into three separate regions where different behavior occurs. The first region,  $y \ll Q^{-1}$ , represents a situation of low particle density or high salt concentration, where the fraction of ions that are ‘bound’ to the charged particles is small compared to the total concentration. In this case, the familiar barometric height distribution is recovered, resulting in an ‘classic’ exponential decrease in number of particles versus height. At the other extreme,  $y \gg 1$ , there are almost no ions in the solution, and the few that are present are tightly bound to the charged particles, effectively

moving as a single unit. Also here an exponential decay is found, albeit with a different typical length. However, in between these two regimes,  $Q^{-1} < y < 1$ , the entropy of the ions and the electric field around the charged particles are in competition, and there are not enough ions to satisfy both. As a result, the concentration of particles decreases *linearly* with height, effectively being lifted up by the electric field of the ions in the solution that want to be as homogeneously distributed as possible. Although particle-particle interactions are not taken into account in this description, it has been shown that the theory still holds for particle volume fractions up to 4% with  $\kappa a = 2.0$ .<sup>45</sup>

### 2.1.3 Radial distribution function and pair potential

Dispersions of colloidal particles can be analyzed using methods from statistical mechanics. By recording many different configurations of particles, and measuring the distances between them, one can calculate the probability of finding a particle at a certain distance,  $r$ , away from another particle. This probability distribution (normalized by the average density) is called the radial distribution function (RDF),  $g(r)$ . An important feature of  $g(r)$  is that it can be ‘inverted’ to obtain the potential of mean force,  $W(r)$ :<sup>47</sup>

$$g(r) = \exp \frac{-W(r)}{k_B T}. \quad (2.3)$$

Here,  $k_B$  is the Boltzmann constant ( $1.38 \cdot 10^{-23} \text{ m}^2 \text{ kg s}^{-2} \text{ K}^{-1}$ ) and  $T$  is the absolute temperature (K). For a collection of identical particles, the potential of mean force can be written as the sum of all multiple particle interactions:

$$\begin{aligned} W(r) = & u(r) \quad (\text{pairs, } \propto \rho^2) \\ & + v(r) \quad (\text{three particles, } \propto \rho^3) \\ & + w(r) \quad (\text{four particles, } \propto \rho^4) \\ & + \dots \end{aligned} \quad (2.4)$$

If the volume fraction,  $\rho$ , is low enough, then the potential of mean force is predominantly determined by interactions between only two particles and higher order terms can be neglected. Therefore, by measuring the probability distribution at sufficiently low volume fraction,  $g(r)$  can be inverted to obtain the pair potential,  $u(r)$ :<sup>47</sup>

$$g(r) = \exp \frac{-u(r)}{k_B T}. \quad (2.5)$$

For higher volume fractions or large interaction ranges such that on average more than two particles interact, one needs to resort to liquid state theories and/or computer simulations to obtain interaction potentials.<sup>48</sup> The obtained potential can also be fitted (e.g. using DLVO theory) to

extract parameters such as particle charge and screening length. The assumption that the total interactions between the particles can be written as a sum of pair potentials is called ‘pairwise additivity.’ Moreover, as long as the system is pairwise additive,  $g(r)$  is unique for fixed temperature and density and thus the complete phase behavior can be extracted by measurements of  $g(r)$  as function of density.<sup>49,50</sup> The volume fraction at which the assumption of only two particles interacting breaks down will decrease as the interactions become longer ranged.<sup>48,51</sup> At such volume fractions, more structure appears in  $g(r)$ , familiar from liquid-state theory,<sup>52</sup> usually in the form of a peak, followed by damped oscillations.

### 2.1.4 Materials for colloidal particles

Colloidal particles can be prepared out of a wide variety of materials, from metals, oxides, organic polymers to biological molecules. However, the most common materials for colloidal particles are polymers such as polymethylmethacrylate (PMMA)<sup>10,11</sup> and polystyrene (PS),<sup>9</sup> inorganic oxides such as silica<sup>12,16</sup> and titania,<sup>13,14</sup> and hydrogels such as poly(N-isopropylacrylamide) (pNIPAM).<sup>15</sup> Aside from the compatibility of these materials with their applications, the choice of material also affects the interactions between the particles.

Steric interactions are caused by the repulsive forces generated when the molecules on the particle surface start to overlap.<sup>37</sup> Coatings (or ligands) on the particle surface may affect the interaction near contact. The material’s index of refraction is also of concern, as the difference between it and that of the medium affects the van der Waals forces.<sup>38</sup> By dispersing particles in a medium with the same refractive index, the van der Waals force vanishes. This is commonly called ‘index matching.’<sup>53</sup> Likewise, the difference in density between the particle and the medium dictates the force on the particles due to gravity. The gravitational energy,  $E_{\text{grav}}$ , is given by:

$$E_{\text{grav}} = \frac{4}{3}\pi a^3(\rho_{\text{col}} - \rho_{\text{sol}})gh, \quad (2.6)$$

where  $a$  is the particle radius, (475 nm),  $\rho_{\text{col}}$  is the colloid density (1.80 g/mL for silica),  $\rho_{\text{sol}}$  is the solvent density (1.00 g/mL for CHC),  $g$  is the acceleration due to gravity (9.81 m/s<sup>2</sup>) and where  $h$  is the particle-wall distance ( $m$ ). This equation can be used to calculate the gravitational height: the distance at which the gravitational energy is equal to one  $k_{\text{B}}T$ . For the particles used in this work, this was 1.16  $\mu\text{m}$ , or 1.22 times the particle diameter. Similar to the van der Waals force, the gravitational force can be eliminated as well by using particles and medium with the same density. The mechanism by which the particle acquires its charge is also affected by the material, affecting both the magnitude and the sign of the particle charge. In some cases, chemical modification is employed to alter a particle’s native charge, even reversing the sign. Moieties such as silanol, amine, phosphate, and carboxylic acid groups are sensitive to

pH, allowing the charge to be tuned. Specific adsorption of ions may also influence the particle charge.<sup>54</sup>

In addition to the differences between the charging mechanism, the electrostatic interactions may also become volume fraction dependent in some cases.<sup>39</sup> If the number of ions that are released or absorbed by the chargeable groups of the particle is a significant portion of the total ion concentration, then the ionic strength - and through it,  $\kappa^{-1}$  - will vary with volume fraction. At high volume fraction, charged particles may be brought together so closely that charged groups de-charge to mitigate the electrostatic repulsion with other particles. Under these conditions, the particles can usually be described as having a constant potential instead of a constant charge. Additionally, if adsorption of ions from solution is the predominant way for a particle to acquire charge, and the ionic strength is low, then there will be fewer ions available per particle as the volume fraction increases.

Particles composed of pNIPAM owe their popularity to the fact that they are thermoresponsive, allowing the particle size to change with temperature in a controlled manner.<sup>15</sup> PMMA particles can be both index and density matched by dispersing them in a mixture of cyclohexyl bromide (CHB) and cis-decalin, which is particularly advantageous for large particles. Additionally, other components can be easily incorporated due to the acrylate groups, either during the synthesis or afterwards. Silica is known for excellent thermal, chemical and mechanical stability and controllable porosity, and its chemistry is well understood.<sup>17,18,55</sup> Furthermore, the silica surface can be readily modified/coated with a wide variety of materials and, perhaps more importantly, silica can easily be coated on other materials.<sup>56</sup> When dispersed in cyclohexyl chloride (CHC) or a mixture of glycerol and water, silica can be index matched. CHC has the added advantage that it can be deionized, allowing for the formation of extremely long double layers, many particle diameters long.<sup>57,58</sup> Unfortunately, silica particles tend to aggregate in these low polar media, requiring the surface to be coated with an apolar alkyl chain, usually octadecyltrimethoxysilane (OTMOS), to prepare dispersion of single particles.<sup>57,59</sup>

In this work, we present a different method to transfer silica particles to CHC without the need for an apolar coating on the particles. Using this method, long range repulsive dispersions can be prepared. Dispersions were prepared at various volume fractions and at different times after the particles had been synthesized. The particle surface potential was estimated by analyzing the distance between the particles and the charged capillary wall and by fitting the pair potential as obtained from  $g(r)$ . Additionally, microelectrophoresis measurements were performed on some of the samples to determine the zeta potential, which we in this work equate with the surface potential.<sup>38</sup>

## 2.2 Experimental

In this section, we will describe the synthesis of silica particles with a fluorescent core. We will also describe the procedure to transfer these particles from ethanol to trimethylolpropane ethoxylate triacrylate (ETPTA), from which they can be added to CHC. Additionally, we will outline the procedure for the microelectrophoresis measurements and the experiments using the confocal microscope.

### 2.2.1 Chemicals

For the synthesis of the silica particles and the preparation of the samples, we used the following chemicals: fluorescein isothiocyanate isomer I (**FITC**),  $\geq 90\%$  (Sigma), (3-aminopropyl)triethoxysilane (**APTES**),  $\geq 98\%$  (Sigma-Aldrich), ammonium hydroxide solution (**ammonia**), puriss p.a., ca. 25% (Sigma-Aldrich), ethanol, 100% (interchem), tetraethoxy silicate (**TES**), 98% (Aldrich), chlorocyclohexane (**CHC**), 98% (Alfa Aesar), trimethylolpropane ethoxylate triacrylate (**ETPTA**), average  $M_n \sim 428$  (Sigma-Aldrich), molecular sieves, 4A, 10 to 18 mesh (Acros Organics). Deionized water was obtained from a Millipore Direct-Q3UV water purification system. All chemicals were used as received. ETPTA and CHC were deionized by mixing with molecular sieves ( $\sim 10$  wt%) and leaving them, away from sunlight, for several days.

### 2.2.2 Particle synthesis

Fluorescently dyed silica seed particles were synthesized following a modified Stöber synthesis.<sup>16,24</sup> In the first step, APTES was coupled to the dye. For this purpose, 0.0493 g of FITC was added to a new 4.0 mL vial, followed by 2.000 mL ethanol, resulting in a bright orange liquid. After magnetically stirring for 15-20 minutes, 0.300 mL APTES was added. This turned the liquid clear and dark red. The vial was wrapped in aluminum foil and stirred overnight. If the mixture did not become clear, and instead remained turbid, then the synthesis usually resulted in polydisperse or aggregated particles. We suspect that in these cases, residual water in the mixture already initiated polymerization of APTES.

For the second step, a 1000 mL single neck round bottom flask was cleaned with eight wt% HF solution for 30 minutes and then rinsed with deionized water, ethanol, and dried at 50 °C for one hour. An elliptical magnetic stirbar was placed inside the round bottom flask, followed by 330 mL ethanol and 33.86 mL ammonia. While stirring vigorously (the vortex just reaching the stirbar), 14.355 mL TES was added all at once, immediately followed by the APTES-FITC mixture. After eight minutes, the solution became turbid to the extent that one could no longer see through the middle of the flask. At this point, stirring was reduced to 250 RPM, the flask was wrapped in aluminum foil and left to finish reacting

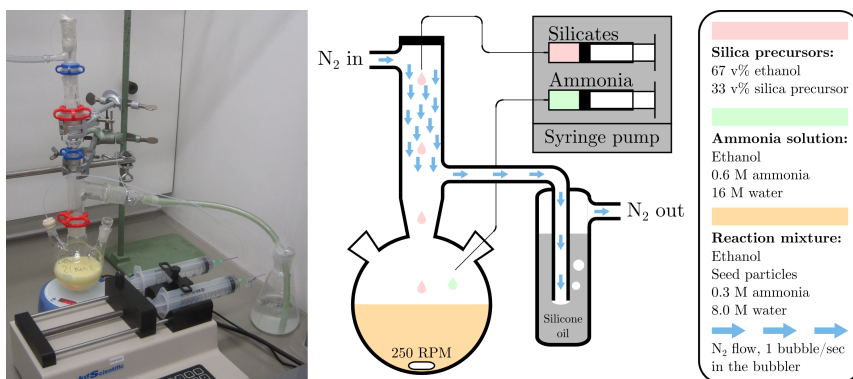


Figure 2.1: Schematic of the experimental setup used for the seeded growth of silica spheres. A photograph of the setup is shown on the left.

overnight. The seed particles were cleaned by centrifuging the particles (300-600 g, 15-35 minutes), removing the supernatant, and redispersing them in ethanol. This was done five times.

The fluorescent silica particles were used as seeds in a seeded growth synthesis where they were grown in one step to their final size, as follows.<sup>60,61</sup> A 250 mL three-neck round bottom flask was cleaned with eight wt% HF as for the seed particle synthesis. It was filled with 47.56 mL ethanol, 8.85 mL deionized water, 20.0 mL seed dispersion (0.036 g/L particles), 3.59 mL ammonia, and magnetically stirred. Two syringes were prepared, one containing an ammonia solution and the other containing a solution of silicate precursor. Syringe 1 was filled with a mixture of 41.3 ethanol, 13.28 mL deionized water, and 5.38 mL ammonia. Syringe 2 was filled with 40.0 mL ethanol and 20.0 mL TES. Higher concentrations of TES resulted in swelling of the rubber stopper, thus preventing it from moving and pushing out the liquid. The syringes were placed in a syringe pump, teflon tubing was connected to the syringes and the tubing was prefilled with liquid. Tubing from the ammonia syringe was then passed through a septum on one of the necks of the round bottom flask and placed a few centimeters above the surface. The tubing from the syringe with silicate precursor passed through a leak tight seal at the top of a glass column which was placed on the central neck of the round bottom flask. From there, droplets could fall unhindered into the reaction mixture. A mild nitrogen flow, one to two bubbles per second measured with a silicone oil bubbler, prevented ammonia fumes from reaching the silicate inlet. Additionally, the nitrogen flow only blew through a part of the glass column, not reaching down to the round bottom flask itself. The addition was started at 0.57 mL/h and gradually increased. After four hours, it was set to 0.90 mL/h, after another four hours it was set to 1.43 mL/h and 19 hours later it was set to 3.60 mL/h. The maximum addition

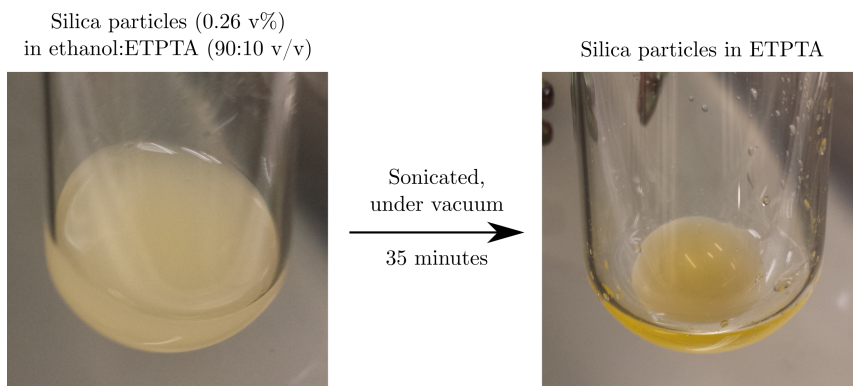


Figure 2.2: Photograph of particle dispersion before and after the solvent transfer from ethanol to ETPTA. The ethanol was removed by evaporation while sonicating the particles. The volume, color, and viscosity of the liquid changed during the procedure.

speed was determined by the particle size, particle concentration and TES concentration.<sup>61</sup> If silica precursor is added too quickly, then this may lead to particle aggregation and secondary nucleation.

After the desired amount of liquid was added, the reaction was allowed to continue for another three hours. Particles were subsequently washed by centrifugation (typically 300 g for 20 minutes) and redispersing in ethanol, similar to the seed particles. This was done at least three times. Particles were not coated with alkylsilanes, octadecanol<sup>62</sup> or longer polymer brushes. Particle dispersions were stored in ethanol in the dark.

### 2.2.3 Solvent transfer

Silica particles in ethanol were transferred to ETPTA by evaporating the ethanol under vacuum while sonicating the dispersion. ETPTA was deionized using molecular sieves before use. For this, molecular sieves were added to ETPTA ( $\sim 10$  wt%) and the container was rotated in a carousel for several days. The particles were dispersed in ethanol:ETPTA (90:10 v/v) at a volume fraction of 0.26 v%. It is important that the volume fraction is low; the same procedure with a volume fraction of 1.3 v% yielded dispersions containing a significant concentration of clusters. The dispersion was connected to a vacuum pump and placed in a sonication bath (Branson 2510, 100 W). After one minute of sonication, the pressure was reduced to approximately 0.2 bar. The liquid was gently swirled to prevent superheating and sudden, rapid boiling. During the procedure, the volume decreased steadily. This was accompanied by a gradual change in color, from pale yellow to a brighter yellow, like that of egg-yolk, as can be seen in Figure 2.2. Additionally, near the end when the amount of remaining liquid was close to the amount of ETPTA, a rise in the viscosity

could be observed. Once no more bubbles formed and no further reduction in volume was apparent, the dispersion was sonicated under vacuum for an extra 15 minutes to ensure the complete removal of ethanol from the mixture. Once dispersed in ETPTA, particles could be added to deionized CHC under magnetic stirring (720 RPM) without particle aggregation.

### 2.2.4 Confocal microscopy and particle tracking

Samples for confocal microscopy (Leica SP8) were prepared immediately prior to use. Dispersions of three different volume fractions were prepared. In order to vary the volume fraction, the amount of added particle dispersion was changed and for samples A1-A3, ETPTA from the same stock (without particles) was added to keep the total ETPTA concentration constant. For samples B1-B3, the dispersion was centrifuged and clear ETPTA from the top was added instead of adding ETPTA from the same stock. This resulted in a more constant conductivity among samples B1-B3 (see Table 2.1). Samples A1-A3 were prepared eight months after the particles were synthesized. Samples B1-B3 were prepared using the same particles, 35 months after synthesis. The particles were stored in ethanol and transferred to ETPTA shortly before the samples were prepared. The exact volume fractions were determined from the confocal data by simply counting particles in a known volume. Sample conductivity was measured using a Scientifica model 627 conductometer. Details of the sample composition and their properties are summarized in Table 2.1.

For each sample, a capillary (borosilicate, 0.10x2.00 mm, Vitrotubes), was filled with the dispersion and sealed with UV glue (Norland optical adhesive #68). Particles were allowed to sediment for several minutes. A sequence of 200 confocal  $z$ -stacks was recorded from which we determined the height distribution of particles. The recorded images were 512x512 pixels, 92x92  $\mu\text{m}$ , using a 0.34  $\mu\text{m}$   $z$ -step, over a period of 995 seconds. At the height where the concentration of particles was highest, we recorded images from which we calculated the 2D  $g(r)$ . Using the Tiledscan function of the microscope, a set of five images in a line was recorded 500 times, resulting in a total of 2500 images. Images were 512x512 pixels, 200x200  $\mu\text{m}$ , and the acquisition took 58 minutes and 20 seconds. A certain amount of time must pass for images recorded at the same location to become uncorrelated in time and statistically independent.<sup>47</sup> By recording multiple images in a row, we increased the time between images recorded in the same location without idling the microscope.

Images were processed using computer code in IDL.<sup>63</sup> A detailed tutorial of the code can be found on the author's website, such as for selecting the appropriate 'masscut' and preventing pixel bias.<sup>64</sup> In general, we used a particle radius of 13 pixels. Particles located slightly out of focus appear with lower intensity, and we generally used an intensity limit of 25% of the maximum intensity (exactly in focus) to determine which particles to take into account. Only particles with more than 25% of the intensity of

Table 2.1: Details of sample compositions and measurements. Samples A1-A3 were prepared eight months after the particles were synthesized. For samples B1-B3, this was 35 months.

Sample	CHC ( $\mu\text{L}$ )	Particles in ETPTA ( $\mu\text{L}$ )	ETPTA stock ( $\mu\text{L}$ )	ETPTA from dispersion ( $\mu\text{L}$ )	Conductivity ( $\text{pS cm}^{-1}$ )	Calculated $\kappa^{-1}$ ( $\mu\text{m}$ )	Experimental volume fraction
A1	4990	2.00	8.00	-	41.2	3.59	$6.19 \cdot 10^{-6}$
A2	4990	4.00	6.00	-	27.7	4.38	$9.68 \cdot 10^{-6}$
A3	4990	10.0	0.00	-	17.5	5.50	$3.31 \cdot 10^{-5}$
B1	4990	2.00	-	8.00	34.2	3.94	$6.39 \cdot 10^{-6}$
B2	4990	4.00	-	6.00	43.7	3.48	$3.02 \cdot 10^{-5}$
B3	4990	10.0	-	0.00	32.7	4.03	$6.67 \cdot 10^{-5}$

the highest intensity were counted. Based on the size of the point spread function (FWHM in  $z = 440$  nm), the size of the fluorescent core (diameter = 420 nm), and the intensity cut-off used in the particle identification software (25% of the maximum intensity), we estimate that the thickness of the optical slice was 430-550 nm. This deviation in the  $z$ -position of the particles was small compared to the average interparticle distance ( $\sim 7$   $\mu\text{m}$ ). Using this code, the 2D or 3D particle positions were extracted from the images and were used to calculate the  $z$ -profiles and  $g(r)$ s.

### 2.2.5 Microelectrophoresis

We performed microelectrophoresis measurements on samples B1-B3. The freely diffusing particles in the middle of the capillary were used to extract the exact viscosity of the medium. Prior to the measurements, the samples were homogenized overnight in a rotating stage to negate the sedimentation due to gravity.<sup>65</sup> The samples were mounted on a tilted confocal microscope, such that gravity was pointing along the long axis of the capillary. Electrodes on each end of the capillary were used to generate an electric field along the long axis of the capillary. By applying an electric field in both directions - in the direction of gravity, and opposite to it - the particle velocity due to gravity could be subtracted, leaving only the electrophoretic mobility.<sup>54</sup> 30 seconds after switching on the electric field, a movie was recorded of the particles moving through the liquid. The particle velocity was measured with the use of particle tracking code.<sup>54, 66</sup> This was repeated every 10  $\mu\text{m}$  from the bottom to the top, resulting in a mobility profile across the capillary. When an electric field was applied, the liquid close to the walls flows one way, driven by the double layer adjacent to the charged walls - a process called electro osmosis,<sup>38</sup> while it flows in the reverse direction in the middle. As a result, there are two planes where the flow reverses direction. In these planes, known as the Poiseuille flow stationary planes, there is no net flow of liquid.<sup>67</sup> For the capillaries used in this work, the stationary planes were located at 15% and 85% of the total height from top to bottom. By reading off the mobility at these stationary planes, we obtained the true particle mobility.

## 2.3 Results and discussion

In this section, we will describe and discuss the results of the particle synthesis and solvent transfer procedures followed by the measurements of the interparticle potentials using confocal microscopy, microelectrophoresis and conductivity. Once dispersed in CHC, the particles were allowed to sediment in a capillary and we recorded the distribution of particles above the repulsive wall. The repulsion with the wall was compared to the gravitational energy to estimate the particle surface potential. Additionally,

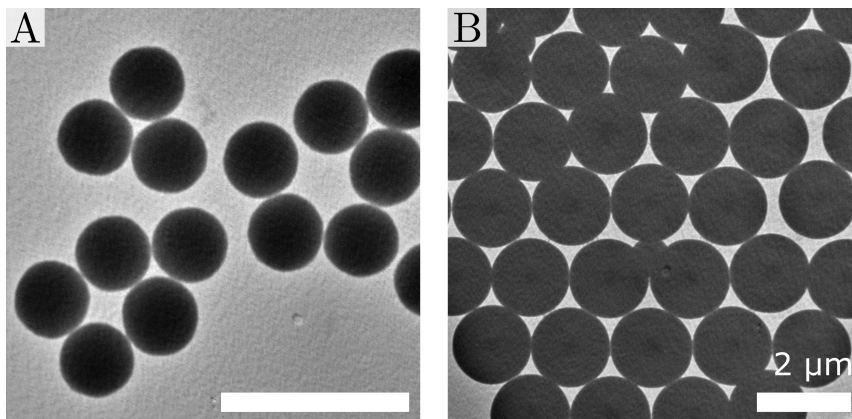


Figure 2.3: TEM images of fluorescently labeled particles (**A**, average radius = 210 nm, PD = 4%) and the particles after further (undyed) seeded growth (**B**, average radius = 425 nm, PD = 2%). Scalebars are 2  $\mu\text{m}$ .

we imaged the particles in the plane parallel to the wall where the volume fraction was highest, with an estimated optical thickness of 430-550 nm. These images were used to calculate the radial distribution function,  $g(r)$ , in the low concentration limit. Fitting these measurements with a DLVO potential provided a second way to calculate the surface potential of the particles. For samples B1-B3, we also obtained an experimental value for the zeta potential through microelectrophoresis combined with measurements of the conductivity. The conductivity of each dispersion was measured in order to obtain a value for the Debye screening length for each sample individually following methods described previously.<sup>57</sup>

### 2.3.1 Particle synthesis

The seed particle synthesis yielded fluorescent uniform spherical particles. A thin layer (10-20 nm) of undyed silica is commonly grown around the particles to improve their electrostatic stability. We did not do this, because the particles were immediately used in a seeded growth synthesis after the excess dye and unreacted material was washed away. Particle size and polydispersity were determined from TEM images using an automated procedure in iTEM software based on particle contrast, counting at least 100 particles. The fluorescent seed particles were 420 nm in diameter, with a polydispersity of 4%. After the seeded growth, the final particle size was 950 nm, with a polydispersity of 2%.

During the seeded growth synthesis, the silica precursor was added dropwise using a syringe pump. Alongside the addition of the silica precursor, a solution of water and ammonia was added to keep their con-

centrations in the reaction mixture constant throughout the growth. The seeded growth faced two main challenges: particle aggregation/clustering, and secondary nucleation. Aggregation of particles can occur when the ionic strength becomes too high, leading to the formation of undesired dumbbells and other small aggregates. In an extreme case, it may even result in en masse particle aggregation. Aggregation may be caused by too rapid addition of TES, because when TES is added to the reaction mixture, the ionic strength increases sharply momentarily.<sup>23</sup>

The other problem that may arise is secondary nucleation; the formation of new particles. As TES is added to the growth solution, it is hydrolyzed to yield precursor monomers. These monomers may encounter - and react with - existing particles, or they can react with other monomers, producing small clusters. Below a critical size, these clusters will also react with existing particles. However, once these clusters reach a critical size, the electrostatic repulsion will become strong enough to prevent them from coming into contact with other particles. At this point, the cluster is stable and will grow on its own, as a new particle. Secondary nucleation is likely to occur if the ionic strength is low, because the critical cluster size is small; if the particle concentration is low, because the probability of clusters encountering (and reacting with) existing particles is low; and if the addition of TES is too fast, because the clusters will grow and reach the critical size more quickly and the larger amount of silanol groups also leads of a larger increase in the ionic strength. Secondary particles were removed after completion of the synthesis during the cleaning steps, together with unreacted monomers and ammonia.

We chose the seed particle volume fraction such that the desired final particle size could be reached with a single growth step of 20 mL TES. Due to the slow addition of TES (27 hours), a mild nitrogen flow was needed to prevent ammonia fumes from reaching the TES inlet above the reaction mixture. Without the nitrogen flow, white solid material formed at the inlet after several hours, sometimes even completely blocking the tubing. However, if the nitrogen flow is too strong, or if it passes through the reaction vessel itself, it may remove so much ammonia that the reaction is perturbed. It is therefore important to flow nitrogen only around the inlet and not through the whole setup.

The rate at which silica precursor may be added to the reaction mixture depended on the particle volume fraction and diameter. The maximum speed of addition was calculated using the method of Giesche.<sup>61</sup> As the quantity of added TES increases, so does the maximum addition speed. We used 50% of the maximum addition speed for the seeded growth syntheses.

### 2.3.2 Solvent transfer

Dispersing silica particles in CHC faced two challenges. Firstly, the low-polar environment of CHC destabilized the particles, causing aggregation if the repulsive potential becomes so small that the particles can come into

physical contact. Secondly, dispersions of silica particles contained too many ions, which put the extremely low ionic strengths needed for long range repulsive systems out of reach. These problems were compounded by the fact that deionized CHC may not be sonicated (a procedure commonly used to break up aggregates) because this causes dissociation of the molecules which increases the ionic strength as was found for the solvent cyclohexyl bromide (CHB).<sup>68</sup> Adding silica particles in a dry state can circumvent the addition of ions to the dispersion. Unfortunately, redispersing dried silica particles tends to result in aggregates, especially when sonication is not an option. Therefore, instead of transferring the particles to CHC directly, we first transferred them to another liquid that can be deionized, can be sonicated without generating ions, and from which silica particles can be added to CHC without destabilization. We found that ETPTA is such a liquid. If necessary, the ETPTA could be replaced with new ETPTA without causing particle aggregation by sedimenting the particles and replacing the supernatant. Silica particles (normally stored in ethanol) remained stable for several months after being dispersed in ETPTA. However, once particles were dispersed in CHC, they were only stable for several days. After two days, small clusters of two or three particles were common. These clusters gradually grew in size, while maintaining stable relative to other clusters. After one week, only large (10+ particles) clusters remained. We suspect that this was caused by slow decomposition of CHC, resulting in the generation of  $H^+$  and  $Cl^-$  ions. The adsorption of the positive ions ( $H^+$ ) would counteract the negative particle charge, leading to instability and clustering. This process is known to occur in the similar solvent CHB.<sup>69,70</sup> Particles containing a silane coupling agent with amine groups, with a net positive charge in water (See chapter 3), remained stable in CHC for a week.

An additional advantage of ETPTA is that it can be used in small concentrations ( $\sim 10\%$ ) to arrest colloidal dispersions almost instantaneously by also adding a photoinitiator and illuminating the sample with UV-light, causing the ETPTA to polymerize.<sup>71</sup> Because ETPTA is capable of forming three covalent bonds it is an effective crosslinker which does not increase the ionic strength in the process. This method can thereby create a 3D physical ‘snapshot’ of the system that can be analyzed over a much longer time.

### 2.3.3 Confocal microscopy and particle tracking

Sedimented dispersion of particles, at three different volume fractions, were imaged in a confocal microscope. Particles from the same synthesis were transferred to ETPTA and then to CHC eight months (samples A1-A3) and 35 months (samples B1-B3) after they were synthesized. We analyzed the dispersions by the height distribution of the particles above the capillary wall after equilibration of the sedimentation profile and by the 2D radial distribution function in a plane parallel to the wall. We estimate

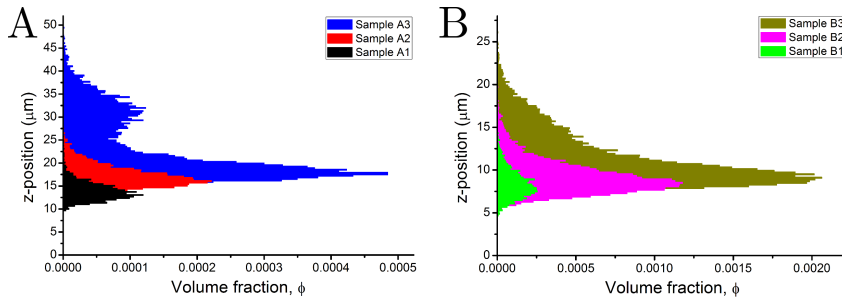


Figure 2.4: Histograms of the  $z$ -position of particles dispersed in CHC at various volume fractions. Samples A1, A2, and A3 are shown together in **A**, Samples B1, B2, and B3 are shown in **B**. In each sample, the wall was at  $z = 0$ . Note the different scale on the y-axis. Based on the number of particle identification, the number of particles per area was: A1: 1.57, A2: 7.41, A3: 16.5, B1: 1.53, B2: 2.39, B3:  $8.18 \cdot 10^{10} \text{ m}^{-2}$ .

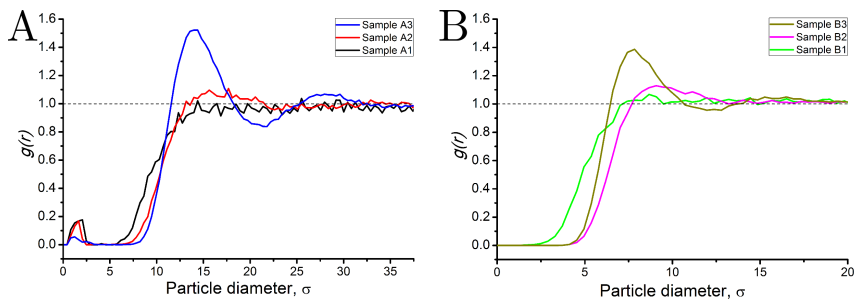


Figure 2.5: Radial distribution functions of all samples, taken at a  $z$ -position where the volume fraction was highest. The optical thickness was estimated to be 430-550 nm. Samples A1, A2, and A3 are shown together in **A**, Samples B1, B2, and B3 are shown in **B**. Note the different scale on the x-axis. Particle diameter was 950 nm.

that the thickness of the segment from which particles were detected for the 2D measurements was 430-550 nm. First, we will describe the height profiles.

We used the reflection signal to determine the position of the wall in each sample and shifted all positions such that the walls were placed at  $z = 0$ . After obtaining all particle locations through particle tracking code in IDL,<sup>35, 48, 64, 72</sup> we made a histogram of the  $z$ -coordinates of all particles in the  $z$ -stacks, shown in Figure 2.4. The histograms show several layers of particles floating at a significant distance above the capillary wall. For sample A3, a second layer was present on top of the first, although it was less well defined. The distance between the layer of particles and the wall was much larger for samples A1-A3 than for B1-B3. In order to obtain an estimate of the particle surface potential, we equated the force due to gravity to that of the DLVO repulsion, where we assumed that the particles and the wall had the same surface potential and assumed in this calculation that effects of the other particles can be neglected. However, we expect that this will lead to an overestimation of the surface potential, as the particles in our experiments were in the intermediate regime ( $Q^{-1} < y < 1$ , using Eq. 2.2), indicating that the entropy induced electric field resulted in a linear rather than an exponential decay. The formula for the gravitational energy, Eq. 2.6, is shown page 17, and for the particles used in this work, the gravitational height was 1.16  $\mu\text{m}$ , or 1.22 times the particle diameter. The DLVO interaction free energy for a sphere and a plate is given by (Eq. 12.48 in Ref. [73] using  $F = 2\pi RW$  from below Eq. 10.18):

$$\frac{W}{k_{\text{B}}T} = \frac{128\pi a \rho_{\infty} \tanh^2 \frac{ze\psi_0}{4k_{\text{B}}T}}{\kappa^2} e^{-\kappa r}. \quad (2.7)$$

Using  $\tanh(x) \approx x$ , for small  $x$ , we obtain:

$$W = 4\pi\epsilon_m\epsilon_0 a \psi_0^2 e^{-\kappa r} \quad (2.8)$$

where we used the dielectric constant of the medium,  $\epsilon_m$ , of 7.6,  $\epsilon_0$  is the permittivity of vacuum,  $\psi_0$  is the potential on the wall and on the particles (assumed to be the same), and  $r$  is the particle-wall separation. Using the experimental values for  $\kappa^{-1}$  (see Table 2.1), we calculated the surface potential necessary for the electrostatic repulsion to balance the gravitational force at the position of the highest particle volume fraction, i.e.  $h = r$ . These potentials are summarized in Table 2.2. Among samples A1-A3, and B1-B3, the values are very similar (15 to 18 mV), indicating that the particles carried close to the same charge at these different volume fractions. However, the potential on the older particles was less than half that of the ones measured earlier, suggesting that the particles became less charged over time. The particle zeta potentials will be treated further down in the text, after the other measurements have been discussed.

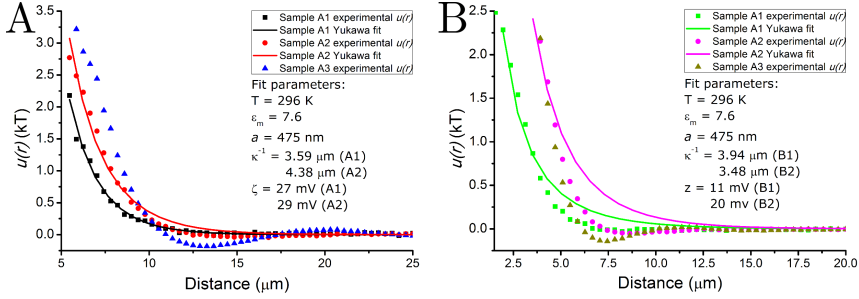


Figure 2.6: Potential of mean force,  $u(r)$ , obtained by inversion of  $g(r)$  from experiments for samples A1-A3 (A) and B1-B3 (B) along with fitted Yukawa potentials for A1, A2, B1, and B2 using Eq. 2.9.

Images were recorded in the layer of particles parallel to the wall, from which the 2D particle positions were extracted using the same IDL particle tracking code as above. It is important that the images from which  $g(r)$  was calculated were uncorrelated.<sup>47</sup> If they are not, a certain state of the system may be oversampled and  $g(r)$  will not fully and equally reflect the states available to the system. Images can be uncorrelated in place and in time. We allowed enough time between images taken at the same place for a particle to diffuse over its own diameter, which for our particles was seven seconds. During this time, we recorded five images next to one another using the TileScan function of the microscope. Using these statistically independent images, we calculated  $g(r)$ . The  $g(r)$ 's are shown in Figure 2.5. For samples A1-A3, a small peak at one particle diameter was present due to a few small clusters of particles. For the low volume fraction samples,  $g(r)$ 's showed an excluded zone at short distance, followed by a gradual rise but contained no further structure, indicative of only two particle interactions being present. However, at higher volume fraction,  $g(r)$ 's exhibited significant structure, revealing multiple peaks. The range of the repulsion was much larger in samples A1-A3 than for B1-B3, similar to the  $z$ -profile measurements discussed above.

For each sample, we inverted  $g(r)$  to obtain the potential of mean force,  $u(r)$ ,<sup>47</sup> which is plotted in Figure 2.6. This only yielded reasonable two particle interaction curves for the low and middle volume fractions, because the high volume fraction  $g(r)$ 's contained too much structure. We fitted these  $u(r)$ s with a Yukawa potential for two spheres ( $i$  and  $j$ ):<sup>5</sup>

$$\frac{V_{ij}}{k_B T} = Q_i Q_j \lambda_B \frac{e^{\kappa(a_i + a_j)}}{(1 + \kappa a_i)(1 + \kappa a_j)} \frac{e^{-\kappa r}}{r}. \quad (2.9)$$

The number of charges on the particle,  $Q$ , can be converted to a zeta potential,  $\zeta$ , using: (from Ref. [38] Eq. 8.2.24)

$$Q = 4\pi\epsilon_0\epsilon_m a \frac{\zeta}{e} (1 + \kappa a), \quad (2.10)$$

where  $e$  is the elementary charge ( $1.60 \cdot 10^{-19}$  C). With these equations and the experimental values for  $\kappa^{-1}$ , we fitted the pair potential  $u(r)$  using a least-squares fit to obtain the surface potential. The quality of the fit could be improved by allowing different values of  $\kappa^{-1}$ , which in all cases resulted in shorter Debye lengths and larger potentials. However, we opted to use the experimental values for  $\kappa^{-1}$  in order to better compare them to the values obtained from the other measurements. The potentials are summarized in Table 2.2. Almost the same values were obtained for samples A1 and A2. The difference between the surface potential obtained from the  $u(r)$  fitting and the  $z$ -profile could be because the assumption of equal charge on the walls and the particles was incorrect; a higher potential on the wall would have resulted in a lower potential on the particle. The surface potentials for the older particles, B1 and B2, were lower than for A1 and A2, as was also found above. For the older particles, there is only partial agreement with the surface potentials obtained from the  $z$ -profiles. However, they were close to those obtained by microelectrophoresis (see below).

The distribution of particles relative to the bottom capillary wall and each other was well described by DLVO theory using experimental values for  $\kappa^{-1}$ , yielding surface potentials that explain the wall distances and  $g(r)$ s properly. However, due to the entropic lift, the particle surface potentials calculated from the sphere-wall DLVO repulsion are likely overestimated. Also, effects caused by (repulsion from) neighboring particles were neglected, which may have influenced the results in particular for sample A3, as this sample showed the formation of a distinct second layer on top of the first. Among samples A1-A3, the obtained surface potentials were consistent, both from the  $z$ -profiles and from fitted  $u(r)$ s. We expect that the discrepancy between the values obtained using the different methods was due to assumptions made in the calculation that the particles and the wall had the same potential and that there were no other particles around (or above), and that fitted  $u(r)$ s were more accurate.

For samples B1-B3, similar surface potentials were obtained from the  $z$ -profiles for each sample. Additionally, the values obtained from fitting  $u(r)$  and from microelectrophoresis were in good agreement with one another. Although they deviated somewhat from the  $z$ -profile values, all methods showed that the particle charge of the older particles was substantially lower (almost half). This decrease in particle charge over time may be attributed to a decrease in silanol groups. Neighboring silanol groups can react with each other to a siloxane bond, thereby lowering the number of groups that can generate negative charge. Another explanation could be related to residual water inside the micropores of the silica particle.<sup>74-76</sup> The water inside the silica matrix may act as an ion sink, offering refuge for ions in the low polar medium. Bulk water in contact with CHC is known to act as such an ion sink.<sup>77,78</sup> After being stored in ethanol for an extended period of time, the water molecules inside the particle may have

Table 2.2: Particle surface/zeta potentials determined by confocal microscopy and microelectrophoresis of samples A1-A3 (eight months old) and B1-B3 (35 months old).

Sample	Calculated $\kappa^{-1}$ ( $\mu\text{m}$ )	Particle potential		
		$z$ -profile (mV)	$g(r)$ inversion (mV)	Microelec. (mV)
A1	3.59	34	27	-
A2	4.38	38	29	-
A3	5.50	36	-	-
B1	3.94	15	11	13
B2	3.48	18	20	30
B3	4.03	18	-	18

escaped into the solution, leaving a particle that can adsorb fewer ions. Nonetheless, stable long-range repulsive dispersions were prepared in both cases.

### 2.3.4 Microelectrophoresis

The particle zeta potential was measured for samples B1-B3. Particle velocity was determined by particle tracking code in IDL every 10  $\mu\text{m}$ .<sup>54,66</sup> The resulting mobility profiles are plotted in Figure 2.7, where the stationary planes are indicated by dashed lines. The mobility,  $\mu$ , was converted to zeta potential using the Hückel equation:<sup>38</sup>

$$\zeta = \frac{3\mu\eta}{2\epsilon_m\epsilon_0}, \quad (2.11)$$

using a viscosity,  $\eta$ , of 1.57 mPa s. This relation holds for particles with a low zeta potential ( $<25$  mV) and which have a large double layer ( $\kappa\alpha \ll 1$ ). The particles used in this study satisfied both conditions. The zeta potentials, listed in Table 2.2, match those obtained from  $u(r)$  fitting reasonably well and are in the same range as those from obtained from the  $z$ -profile. Unfortunately, due to the extremely low volume fractions, only very few particles ( $<20$ ) were visible in the movies. This resulted in a significant error in the values in the mobility data.

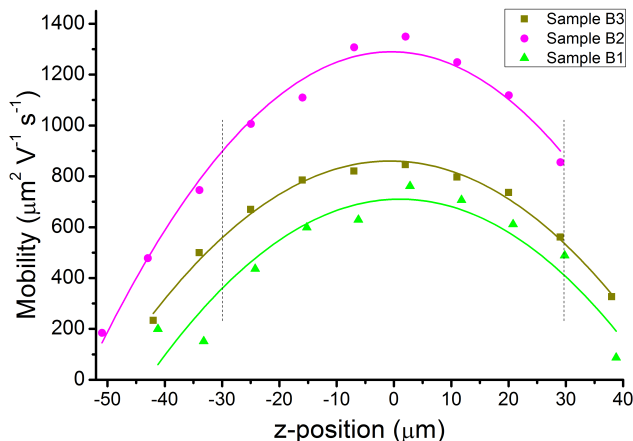


Figure 2.7: Electrophoretic mobility profiles and parabolic fits for samples B1, B2, and B3. The stationary planes in the Poiseuille flow are indicated with dashed lines.

## 2.4 Conclusions and outlook

We have demonstrated a new method of transferring silica particles from ethanol to CHC without the need for an apolar sterically stabilizing surface coating on the particles by first transferring them to the monomer ETPTA, acting as a solvent. Ethanol was removed by evaporation while sonicating the dispersion. Once in ETPTA, particle dispersions were stable for months and could be added to CHC by regular magnetic stirring, resulting in dispersions of single particles with large double layers of several times the particle size. The surface potential of the particles was calculated from the equilibrium distance between the sedimented particle layer and the capillary wall, from inversion of  $g(r)$ , and by measuring the electrophoretic mobility. Dispersions with different volume fractions were prepared and we observed no dependence of the particle charge on the volume fraction. However, old particles (35 months after synthesis) appeared significantly less charged compared to newer particles (eight months after synthesis). This may be attributed to slow and gradual removal of water from the micropores inside the silica matrix. Comparison of the experimental data with computer simulations and theory could be used to check the results more quantitatively and to also take into account many parameters that were now neglected.<sup>43</sup>

ETPTA can be added to particle dispersion in low concentrations and rapidly polymerized using a photoinitiator and UV light. In doing so, dispersions can be arrested nearly instantaneous while preserving particle positions and thus the structure of the suspension for extended analysis. Therefore, ETPTA is a convenient medium for the silica particles, as it as-

tures that these final particle dispersion will contain no additional liquids or traces. The convenient transfer of particle to CHC, combined with the tunability of the potential through the salt concentration and the ability to make 3D ‘snapshots’ of the particle distributions allows for direct measurement of the interparticle potential. We expect that these techniques can also be applied to particles smaller than 100 nm, allowing for the direct measurement of the potential between nanoparticles for the first time. The slow charge reversal of the particles dispersed in CHC also allows for the study of the formation of oppositely charged crystals,<sup>5</sup> in particular with the possibility of arresting their structure by rapid polymerization of ETPTA at various stages of formation.

## 2.5 Acknowledgments

The authors wish to thank Peter Helfferich for the microelectrophoresis measurements and Ernest van der Wee for assistance with the tracking code. We also want to acknowledge Johan Stiefelhagen for careful reading of the chapter.

# 3

---

## Synthesis of oppositely charged colloidal silica and yolk-shell particles

---

In this chapter, we study the morphology and charge of colloidal silica particles containing a layer of organically modified silica ('ormosil'). The ormosil is synthesized by incorporating a silane coupling agent (SCA), N-[3-(trimethoxysilyl)propyl]ethylenediamine (EDAPTMS), during the growth reaction. We are able to incorporate a large amount of SCA into the ormosil: up to 25 mol%. This ormosil differs from regular 'pure' Stöber silica in several ways: it is positively charged at neutral pH, and it is highly susceptible to etching with HF solution. By synthesizing particles containing an ormosil layer in between a pure silica core and outer shell and subsequently etching with HF solution, the ormosil layer can be removed leaving fluorescently labeled pure silica 'yolk-shell' particles: a small particle inside a shell. The removal of the ormosil layer by HF etching occurs through two etching pathways: it is either removed homogeneously from all sides through the shell, or from a single point/line. Dumbbell particles etch more quickly than single spherical particles. We attribute this to a thinner/weaker outer silica shell in the neck region in the middle of the dumbbell. Additionally, the particle zeta potential can be reversed from -80 to +58 mV by coating it with only a few nanometers of ormosil. Moreover, the zeta potential of particles containing an ormosil layer and an outer silica shell can be tuned by mild HF etching. This reversal of the particle charge completes before morphological changes occur.

### 3.1 Introduction

Nowadays, a wide variety of colloidal particle shapes is accessible through different synthesis strategies, for instance: spheres, rods,<sup>79</sup> platelets,<sup>80,81</sup> cubes,<sup>82-84</sup> triangles,<sup>85</sup> and octapods.<sup>86,87</sup> Besides the variety in shape, particles can be synthesized out of various materials, contain fluorescent moieties,<sup>24</sup> and biologically relevant labels and coatings.<sup>88,89</sup> In addition to solid particles, it is possible to synthesize particles consisting of physically unconnected parts. The simplest example is a sphere inside of another hollow sphere (shell), referred to as ‘yolk-shell’ or ‘rattle/rattler’ particles.<sup>90</sup> The smaller core particles are often metal or metal oxide nanoparticles with specific optical,<sup>91</sup> magnetic<sup>34</sup> or catalytic properties.<sup>92</sup> The outer shell is commonly composed of silica because it is strong, chemically inert, easy to synthesize and compatible with medical applications.<sup>93</sup> The function of the shell that surrounds the nanoparticles is usually strictly as a barrier; it can prevent the nanoparticles from aggregating,<sup>94</sup> contain cargo for drug delivery,<sup>95,96</sup> be used as a nanoreactor,<sup>97</sup> or for sensing.<sup>98,99</sup> The removal of material to create internal void space can be achieved in many ways: a polymer layer can be grown that is burned away after the formation of a shell,<sup>100</sup> organic functionalities can be incorporated in the silica matrix that can be removed by etching<sup>101,102</sup> or thermal treatment<sup>103</sup> and the interior of regular silica particles can be removed by heating in acidic aqueous solution,<sup>104</sup> a solution containing  $\text{NaBH}_4$ ,<sup>105</sup> and even in pure water.<sup>106</sup> We call the particles that have been synthesized with a removable section ‘Core-Layer-Shell’ particles when the layer is still present. After the layer has been removed, we refer to them as ‘yolk-shell’ particles. Many variations of the yolk-shell design have been synthesized, such as those with multiple cores,<sup>107</sup> and multiple shells.<sup>108</sup> The latter are sometimes referred to as ‘Matryoshka particles’, named after the Russian dolls that fit inside each other in a core-shell fashion.

For use in optical microscopy, in particular confocal microscopy, it is often advantageous to use fluorescent particles.<sup>35</sup> This is usually achieved by incorporation of an organic fluorescent dye into the structure. If such dyes are used, then the void space can not be created using calcination, because these dyes are unable to withstand high temperatures. An alternative removal method was demonstrated by Chen et al.<sup>101</sup> which uses silica doped with a silane coupling agent: N-[3-(trimethoxysilyl)propyl]-ethylenediamine (EDAPTMS). They showed that EDAPTMS-doped silica (EDAPTMS is called TSD in their article) is rapidly etched by hydrofluoric acid (HF), while leaving the undoped silica intact, and that this can be used to make yolk-shell particles.

Aside from the influence on the structure and etching properties, the incorporation of EDAPTMS into the silica structure also affects the particle charge. The amine groups in the EDAPTMS side chain (see Figure 3.1 below) can acquire a positive charge by absorption of a proton, provided they are accessible for protonation from the outside. In this way, these

groups counteract the inherent negative charge from the silica silanol groups. Moreover, spatially inhomogeneous charge distributions within a particle are of interest, because they may allow for tuning of the particle charge through the salt concentration. The electrostatic potential of charged colloidal particles is screened by ions in the solution. This screening causes the potential to decay exponentially, characterized by the Debye screening length, which sets the range of the potential. By changing the Debye screening length, it is possible to alter the combination of groups contributing to the particle potential. In other words, by increasing the Debye screening length, contributions from charges deeper in the particle are ‘mixed in’ with the potential. If the charge of these internal groups is opposite to that of the groups closer to the surface, then the salt concentration would allow for smooth tuning of the particle potential, which would be advantageous for the study of crystals of oppositely charged particles.<sup>5,109</sup>

In this chapter we present the synthesis of Core-Layer-Shell particles with a fluorescent core by HF etching of heavily doped silica (also called ‘ormosil’ for ‘organically modified silica’). We determined the EDAPTMS content in the ormosil layer and investigated the effects of HF etching on the charge and the morphology of the particles. Additionally, we studied the difference in etching behavior between ormosil silica and ‘pure’ Stöber silica in NaOH solution. Below, we will present a brief overview of the structure and etching of Stöber silica.

### 3.1.1 Stöber silica structure

In the Stöber process, silica precursors are hydrolyzed in an ethanol solution containing ammonia.<sup>16</sup> The hydrolyzed monomers then react with one another to form small clusters that eventually form small particles. Above a critical size, the charge on these particles prevents them from fusing with other particles.<sup>19</sup> From this point on, they grow independently by the addition of monomers and small clusters that are not yet charged strongly enough.<sup>20,23</sup> The aggregative growth process in Stöber synthesis results in silica particles that are not completely condensed, i.e. a fraction of the silicon atoms has fewer than four (the maximum) number of bonds to neighboring silicon atoms, called ‘siloxane’ bonds. NMR studies have found that about 30% of the silicon atoms have only three siloxane bonds.<sup>24,110</sup> Additionally, the density of Stöber particles is usually found to be approximately 1.8 g/mL, whereas completely condensed silica has a density of 2.2 g/mL<sup>24,60,62</sup> and silica synthesized by the Stöber process is ultramicroporous, meaning that small species such as  $H^+$ ,  $OH^-$  and  $H_2O$  can penetrate the structure.<sup>74</sup> Particle porosity can be greatly affected by the specific conditions during the washing steps after particle synthesis.<sup>76</sup> As a result, a large variety of particle surface areas and porosities are reported in literature. Bazula et al. found that particles went from 2% porosity to 18% simply by washing them in water, ethanol, and then

again in water. However, the porosity had fallen to 3% after four days. Moreover, they were able to increase the porosity even to 31% by adding a surfactant (Lutensol AO5) to the second water washing step, and the increase in porosity was permanent.

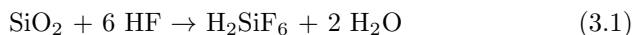
Aging of the particle results in slow densification and increased cross-linking of the structure, particularly near the particles outer surface. This can be accelerated by heating the particles in water to 60 °C<sup>111</sup> and a high temperature treatment at 900 °C can be employed to completely densify the particles.<sup>112, 113</sup>

### 3.1.2 Etching of Stöber silica

Silica can be chemically removed in several ways. The etching of silica involves breaking the siloxane bonds and removing the silicates as a gas or dissolved species. If the silica network is only poorly interconnected, such as shortly after the synthesis of Stöber silica, hot water (90-95 °C) is enough to redissolve it<sup>106, 111</sup> because the solubility of silicates in water increases greatly with temperature.<sup>17</sup> However, the etching capability of hot water was reduced after the particles were aged at room temperature, allowing the outer surface to withstand the dissolution, or at 60 C, which prevented hollowing out entirely.<sup>111</sup>

As in hot water, the solubility of silicates increases sharply above pH 9. Additionally, the hydrolysis and condensation reaction of siloxane bonds are catalyzed by base, accelerating the dissolution process. Therefore, alkaline solutions, such as NaOH, are commonly used to etch/dissolve silica. In these solutions, the hydroxide ion (OH<sup>-</sup>) attacks the silicon atom, replacing one of the siloxane bonds through a fivefold coordinated transition state on the silicon.<sup>18</sup>

Another well known method to etch silica is to use HF. This is extensively used in the semiconductor industry at high concentration (40-49 wt%).<sup>114, 115</sup> Like OH<sup>-</sup>, F<sup>-</sup> is a small nucleophile that can attack the silicon atom, cleave siloxane bonds, and dissolve silica. However, the fluoride ion etches more aggressively and the Si-F compounds are gaseous, resulting in a terminating reaction. The mechanism is complicated, especially for high HF concentrations, but the net reaction is reported as:



with a Si:F stoichiometry of 1:6.<sup>116, 117</sup> Although it is sometimes also presented with a stoichiometry of 1:4.<sup>102</sup>



The Si:F ratio can be used as an indicator of the degree of etching; more fluoride per silicon meant a higher the rate of etching. However, it is worth emphasizing that the HF concentrations used in this work are all orders of magnitude lower than those commonly used for industrial etching of

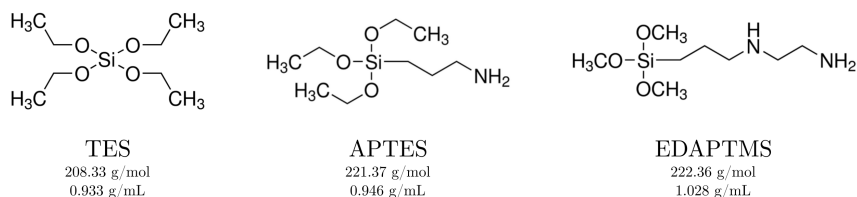


Figure 3.1: Structure formulas of the silane coupling agents used in this chapter. Note the amine groups in APTES and EDAPTMS.

silica. Even the highest fluoride concentration we used in our experiments is lower than that of regular toothpaste (1450 ppm)!

Incorporation of other elements into the silica matrix, usually achieved by co-condensation of silane coupling agents (SCA), can affect the etching behavior of the material. The chemical reactions shown above change slightly when considering etching silica containing SCAs, because the Si-C bond is not cleaved by HF. The incorporation of organic functionality leads to a decrease in the crosslinking density of the silica matrix, making it more susceptible to etching and dissolution. Silica shells containing APTES (a silane coupling agent, see section 3.2.1) were found to etch in ammonia, whereas pure silica shells were not.<sup>94</sup> Also, Chen et al. found that HF etched EDAPTMS-doped silica preferentially, while leaving the pure silica mostly intact.<sup>101</sup> They also reported that several other SCAs - including a shorter but similar SCA APTES - did not result in preferential etching. It may be possible that specific interactions with chemical moieties (such as the amine groups in APTES and EDAPTMS) also influence the etching process.

## 3.2 Experimental Section

### 3.2.1 Chemicals

The following chemicals were used without further purification: absolute ethanol (J.T. Baker), ethanol 100% (Interchemia), ammonia (26.6 wt% NH<sub>3</sub> in H<sub>2</sub>O, Sigma-Aldrich), fluorescein isothiocyanate isomer I (**FITC**, Sigma), rhodamine B isothiocyanate (**RITC**, Sigma-Aldrich), tetraethoxy silicate (**TES**, Aldrich), (3-aminopropyl)triethoxysilane, 98% (**APTES**, Sigma-Aldrich), N-[3-(trimethoxysilyl)propyl]ethylenediamine, 97% (**EDAPTMS**, Sigma-Aldrich), hydrofluoric acid, 40-45%, technical grade (**HF**, Riedel-de Haën), sodium hydroxide, 98% (Fischer Scientific), and sodium chloride, p.a. (Acros Organics). Deionized (DI) water was obtained from a Millipore Direct-Q3 UV water purification system. The structure formulas of the silica precursors are shown in Figure 3.1.

### 3.2.2 Particle synthesis

Fluorescently labeled organo-silica core-shell particles were synthesized using a modified Stöber method,<sup>16</sup> utilizing seeded growth<sup>12,23,61</sup> and the incorporation of silane coupling agents (SCAs)<sup>24,118</sup> leading to organo-silica particles. These procedures are commonly used and well described in literature.<sup>19,22,23,60,61,119,120</sup> These initial particles were subsequently coating with a hybrid organo-silica layer (also called ‘ormosil’ for ‘organically modified silica’) with a significantly larger SCA loading, following a modified version of the procedure described by Chen et al.<sup>101</sup> Finally, again a ‘pure’ Stöber silica outer shell was grown around the Core-Layer particles using another seeded growth step. A typical synthesis is summarized in Table 3.1, which yielded particles CLS1 (see Table 3.6). Aside from minor changes, such as the use of a different fluorescent dye or growth of a shell with a different thickness, all particles were synthesized following the same procedure. The seeded growth setup was similar to the one used in chapter 2, shown in Figure 2.1 on page 20.

**Fluorescent core particles** FITC-labeled particles were prepared by coupling a dye to APTES.<sup>24,118</sup> We used molar ratios of APTES:FITC of 10:1, and TES:APTES of 50:1. The reaction medium contained 0.60 M ammonia and 3.68 M water, see Table 3.1 for details. For the first step, 2.00 mL of absolute ethanol was added to 0.050 g of FITC and stirred for 15 minutes, resulting in a bright orange solution. Then, 0.300 mL of APTES was added, causing the liquid to become clear and the color to change from orange to deep red. The mixture was stirred overnight, in the dark and at room temperature. In the second step, ammonia was added to ethanol and under vigorous stirring TES was added all at once, immediately followed by the APTES-FITC mixture. After eight minutes, the reaction mixture became turbid to the degree that one could no longer see through the flask. Subsequently, the stirring speed was reduced and the reaction mixture was allowed to react for at least five hours. In the third step, a thin layer of ‘pure’ Stöber silica (~10 nm) was added to improve particle stability and guarantee a greater negative surface charge. For this, 150 mL of reaction mixture and particles was transferred to a clean round bottom flask. Under gentle stirring, TES solution (Solution A) and ammonia solution (Solution B) were simultaneously added to the reaction flask using a syringe pump. Finally, the FITC-labeled particles were cleaned by centrifugation and redispersion in ethanol three times.

Synthesis of RITC-labeled particles followed the same general procedure, but differed on several points. The amount of APTES was reduced, to a molar RITC:APTES ratio of 1:2.3. Also, the APTES-RITC mixture was added first, followed by TES. After the growth of the thin silica layer, particles were centrifuged and redispersed in a fresh mixture of ethanol and ammonia (1.20 M) and a second thin silica layer was grown by dropwise addition of a mixture of 3.00 mL TES in 6.25 mL ethanol.

Table 3.1: Synthesis details for particles CLS1, comprised of FITC-labeled silica core particles and an ormosil layer synthesized with a molar ratio TES:EDAPTMS 3:1. Syntheses were performed at room temperature, while stirring magnetically. During the seeded growth, a slight N<sub>2</sub> flow prevented ammonia fumes from reaching the TES/EDAPTMS inlet (~1 bubble per second). Ratios between seed particles and added TES/EDAPTMS can be changed to tune the size ratios. The synthesis can be modified for synthesizing FITC labeled particles (see text).

Particle	Flask (mL)	Solution A (mL)	Solution B (mL)	Addition
Core 	EtOH	328		Abs. EtOH 2.00
	Ammonia	33.86	TES 14.335	FITC 0.05 g
				APTES 0.30
Thin shell 	Reaction mixture	150	TES 1.00 EtOH 6.86	EtOH 5.34 Ammonia 0.712 DI water 1.81
				Syringe pump, 0.25 mL/h
Layer 	EtOH	619	EtOH 31.27	EtOH 32.29
	DI water	85	TES 11.82	DI water 10.06
	Ammonia	33.62	EDAPTMS 3.816	Ammonia 4.107
	Particles ( $\phi = 0.04$ )	12.5		Syringe pump, 2.0 mL/h
Shell 	EtOH	914		
	DI water	122		
	Ammonia	47.9	TES 8.98	
	Particles ( $\phi = 0.0164$ )	140		Syringe pump, 0.898 mL/min

RITC-labeled particles were washed by centrifugation and redispersion in ethanol ammonia mixture (1.20 M ammonia) four times, and then washed by centrifugation and redispersed in ethanol three times.

**Ormosil layer growth** Seed particles (in ethanol) were dispersed in a mixture of ethanol, ammonia (0.30 M) and water (8.00 M) and gently stirred. A solution was prepared of silica-precursors in ethanol, 1:2 volume ratio, containing TES and EDAPTMS in a molar ratio 3:1. This was added to the dispersion of seed particles by slow dropwise addition using a syringe pump. At the same time, an equal volume of ethanol, ammonia (0.60 M) and water (16.0 M) was added to keep the ammonia and water concentration constant. A mild nitrogen flow (approximately one bubble per second, measured in an externally connected bubbler) prevented ammonia fumes from reaching the TES inlet, (see Figure 2.1 on page 20). After addition was completed, particles were allowed to react for an additional three hours and were then washed by centrifugation and redispersing in ethanol three times.

**Outer shell growth** Core-Layer particles (in ethanol) were dispersed in a mixture of ethanol, ammonia (0.30 M) and water (8.00 M). TES was then added to the reaction mixture under gentle stirring using a syringe pump. Because the added volume of TES was much smaller than the reaction volume, no additional ammonia/water mixture was added. After TES addition, the reaction was left overnight. After synthesis, particles were washed by centrifugation and redispersing in ethanol three times.

### 3.2.3 HF etching

For HF etching experiments, particles were dried by evaporation of the ethanol and redispersed in 10 mL deionized water to obtain a particle concentration of 2.0 mg/mL in Corning centrifuge tubes (15 mL, blue caps). Then, the required amount of 10 wt% HF solution was added with a pipette and the particles were left to react, typically for 20 hours. For example, addition of 70  $\mu$ L of 10 wt% HF solution to the 10 mL particle dispersion yielded a 0.070 wt% HF etching solution. At this concentration, the molar ratio (stoichiometry) between Si and F was 1:1.44. Finally, particles were washed by centrifugation and redispersing in ethanol three times. The etching experiments are summarized in Table 3.7. There was about 10% uncertainty in the HF concentration from the supplier (40-45%). For our calculations, we used the value of 40 wt%.

### 3.2.4 NaOH etching

NaOH etchings were performed in 20 mL scintillation vials at a particle concentration of 0.6 mg/mL. Concentrated NaOH solution was added to the particle dispersion to achieve the desired pH, and the vial was placed

on the rollerbank for 24 hours. Finally, particles were washed by centrifugation and redispersing in ethanol three times.

### 3.2.5 Particle characterization

Particles were characterized using a FEI Tecnai 12 (acceleration voltage 120 kV) Transmission Electron Microscope (TEM) and using a Malvern *Nano ZS* Zetasizer. Measurements in the Zetasizer were performed in dilute suspension in water with 1.00 mM NaCl. Inductively coupled plasma (ICP) measurements were carried out by Mikroanalytisches Laboratorium KOLBE (Germany) using an Elementar ‘Vario EL’ for the carbon and nitrogen content, and a AnalytikJena ‘Specord 50Plus’ UV-Vis detector for silicon. Thermogravimetric analysis (TGA) was performed on a Perkin Elmer Pyris 1. Particles were stored in the dark in pure ethanol. With the exception of the section on aged particles (see paragraph 3.3.2), particles were used within 10 weeks of synthesis.

## 3.3 Results and Discussion

In this section, we will describe and discuss the results of the synthesis and etching experiments with various etchants. We will first discuss the synthesis of Core-Layer-Shell particles, including the optimization of the EDAPTMS content of the ormosil layer. Subsequently, we will present HF etching of such particles, both with and without an outer silica shell. Finally, we discuss other types of etching: NaOH etching, combined NaOH/HF etching, and prolonged dispersion in pure water (three to five days). TEM images were used to assess particle morphology and structure, i.e. particle size, roughness, presence of dumbbells and the way in which the EDAPTMS-doped layer was (partially) removed. Measurements of the zeta potential were used to monitor the particle charge.

### 3.3.1 Synthesis

To increase the contrast in HF etching sensitivity between pure silica and EDAPTMS-doped ormosil, the maximum achievable EDAPTMS content was investigated. Based on the particle charge and radius after the seeded growth, we determined the optimal TES:EDAPTMS molar ratio. The TES:EDAPTMS content in the particles was determined using inductively coupled plasma (ICP) and thermogravimetric analysis (TGA). Several batches of Core-Layer-Shell particles were synthesized using this optimal EDAPTMS content. Particle results will be presented at the end of this section.

Table 3.2: Properties of particles synthesized with ormosil layers containing an EDAPTMS molar content 0.10 to 0.75 in the precursor solution during seeded growth. Particle radius and polydispersity (PD) were determined by TEM. Zeta potentials were determined in water with 1.00 mM NaCl after washing.

Particle	EDAPTMS (mole fraction)	Diameter (nm)	PD (%)	Zeta pot. (mV)
Core-FITC	-	367	2.6	-80 ( $\pm 5$ )
CL_10	0.10	450	2.8	-4 ( $\pm 5$ )
CL_25	0.25	433	3.4	+36 ( $\pm 7$ )
CL_50	0.50	416	3.7	+30 ( $\pm 5$ )
CL_75	0.75	375	2.8	+58 ( $\pm 6$ )

### EDAPTMS-loading

We synthesized Core-Layer particles with a range of TES:EDAPTMS molar ratios in order to create layers containing the maximum amount of EDAPTMS. Mole fractions from 0.10 to 0.75 EDAPTMS were tried by mixing both precursors in ethanol before (dropwise) addition to the reaction medium. However, we note that the silica precursors are not necessarily incorporated with the same efficiency, and that therefore the ratio in the particle may deviate from the one of the reactants. The resultant particle size and charge are summarized in Table 3.2. A layer with an EDAPTMS mole fraction of 0.10 resulted in weakly charged particles, likely caused by an almost equal amount of negatively charged silanol groups and positively charged amine groups. Syntheses with an EDAPTMS mole fraction of 0.25 resulted in stable, positively charged particles. Ormosil layers grown with an EDAPTMS mole fraction in excess of 0.25 also yielded positively charged particles, demonstrating that EDAPTMS was incorporated into/onto the particle, but higher EDAPTMS-loading led to reduced layer thickness. It is known from literature that for several other silane coupling agents, such as APTES and 3-(trimethoxysilyl)propyl methacrylate (usually abbreviated as TPM), particle growth in Stöber conditions stops after several nanometers if no additional TES is added to the growth mixture.<sup>121</sup> This is in line with our findings that at TES:EDAPTMS molar ratios above 3:1, only particle charge was affected while particles size remained nearly constant. From this we concluded that the reactant TES:EDAPTMS molar ratio of 3:1 offered the optimal compromise between particle charge and growth. We did not see complete particle aggregation at these high EDAPTMS-loadings as was reported by Chen et al.<sup>101</sup>

Table 3.3: ICP results (wt%) of Core-FITC2 and CL1. Atom ratios were obtained by dividing the weight percentages by the atomic mass.

Particle	wt%	Atom ratio		
		per C	per N	per Si
Core-FITC2	C 3.26	1	12.3	0.19
	N 0.31	0.08	1	0.02
	Si 40.48	5.33	65.3	1
CL1	C 14.69	1	2.62	1.09
	N 6.53	0.38	1	0.42
	Si 31.35	0.91	2.40	1

Table 3.4: Atomic components of silica precursors after incorporation into the silica structure, i.e. after removal of alkoxy groups.

Atom	TES	APTES	APTES-FITC	EDAPTMS
Si	1	1	1	1
O	2	1.5	6.5	1.5
C	0	3	24	5
N	0	1	2	2
H	0	8	19	13
S	0	0	1	0

### Thermogravimetric analysis and elemental analysis of ormosil layers

To determine the amount of EDAPTMS that was incorporated into the ormosil layer, we performed element analysis by ICP and TGA. ICP measurements were carried out by Mikroanalytisches Laboratorium KOLBE (Germany). Samples for ICP were dried under vacuum at 120 °C for three hours to remove traces of ethanol. Below, we will first discuss the ICP analysis, followed by the TGA analysis.

**ICP** An ormosil layer, with a TES:EDAPTMS molar ratio of 3:1, was grown around FITC-labeled core particles (Core-FITC2 and CL1 particles, see Table 3.6) and ICP was used to measure their atomic composition. For

Table 3.5: Relative silica precursor quantities (mol) for particles Core-FITC2, CL1, and CL1 taking into account the different core particle inside (CL1.corr). Relative quantities based on ICP atom ratios Si:C and Si:N are shown separately.

Particle	Precursor	Relative quantity (mol)		
		Si:C	Si:N	Average
Core-FITC2	TES	96.4	98.6	97.5
	APTES	3.24	1.25	2.25
	APTES-FITC	0.38	0.14	0.26
CL1	TES	78.1	79.2	78.65
	EDAPTMS	21.9	20.8	21.35
CL1.corr	TES	75.5	76.3	75.9
	EDAPTMS	24.5	23.7	24.1

each particle, we obtained weight percentages of carbon, nitrogen and silicon, summarized in Table 3.3. These were converted to atom ratios by dividing them their respective atom masses. The particles were synthesized from four possible precursors: TES, APTES, APTES which was coupled to the fluorophore FITC, and EDAPTMS. The atomic composition of each of these precursors, once incorporated into the silica structure (without the alkoxy groups on silicon), is stated in Table 3.4. The relative quantity of each precursor were adjusted such that the combined atom ratios matched those measured by ICP. For the core particles (Core-FITC2), we optimized the compositions of TES, APTES and APTES-FITC. Relative precursor quantities are summarized in Table 3.5 that best reproduced the experimental Si:C and Si:N atom ratios. These values are in excellent agreement with the synthesis conditions (APTES:FITC molar ratio of 10:1, TES:APTES molar ratio of 50:1). The same analysis was performed for the ICP results for the Core-Layer particles (CL1), only considering precursors TES and EDAPTMS. Although CL1 particles predominantly consisted of the ormosil layer, the core still made up 12.6% of its volume. By subtracting the volume weighted ICP values of Core-FITC2 from those of CL1, we obtained values for the ormosil layer only, labeled CL1.corr. The molar ratio calculated from the ICP results is in excellent agreement with the ratio of the reactants used in the seeded growth experiments (TES:EDAPTMS 3:1 mol:mol) and that therefore nearly all the silane coupling agent was incorporated into the silica particle.

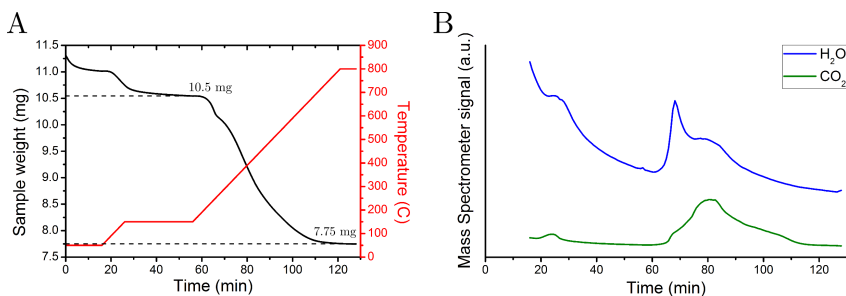


Figure 3.2: TGA measurement of particles CL1. **A**: Sample weight and temperature, **B**: MS signal for water and CO<sub>2</sub>.

**TGA** TGA analysis was performed using an oxygen flow of 20 mL/min and heating the sample in two stages: a drying step, and the combustion. For this, the sample was first heated from 50 to 150 °C (10 °C/min) and then kept at 150 °C for 30 minutes to remove physisorbed water from the particles surface and pores. In the second stage, the particle was heated to 800 °C (10 °C/min). The gas flow was analyzed using a mass spectrometer (MS).

The sample mass and temperature are plotted in Figure 3.2A, and the MS signal for water and CO<sub>2</sub> are shown in Figure 3.2B. From the sample mass and the CO<sub>2</sub> signal we determined that the combustion of the EDAPTMS alkyl-chain occurred only during the second heating stage (150-800 °C). During this time, the sample mass decreased from 10.5 to 7.75 mg, a decrease of 2.79 mg, which we attributed to the removal of EDAPTMS alkyl-chain. The removal of the side chain and replacing it with a bridging oxygen atom carries with it a change in mass of -93 g/mol. We assumed that all the remaining mass was SiO<sub>2</sub>, with a molar weight of 60 g/mol. Using these values, we obtained an TES:EDAPTMS molar ratio of 81:19 for the whole particle. Correction for the mostly undoped core yields a molar ratio in the ormosil layer of 78:22. This EDAPTMS content is in good agreement with those obtained from ICP, and demonstrates that nearly all of the silane coupling agent that was used during the seeded growth synthesis became part of the particle.

### Core-Layer-Shell particles

Fluorescently labeled silica Core-Layer-Shell particles were successfully prepared using the modified seeded Stöber method. Both FITC and RITC labeled particles were synthesized. An overview of all synthesized particles is shown in Table 3.6. All ormosil layers were synthesized with a TES:EDAPTMS molar ratio of 3:1. For particles CLS1, Figure 3.3 shows a TEM image of each stage of the synthesis. The relative size of each section of the particle (core/layer/shell) can be easily controlled by altering the amount of added silica precursor or the seed:precursor ratio.<sup>61</sup>

Table 3.6: Overview of synthesized particles. Layers were grown with a TES:EDAPTMS molar ratio of 3:1. Particle radius,  $r$  and polydispersity (PD) were determined by TEM. Zeta potential,  $\zeta$ , was determined in water with 1.00 mM NaCl after washing.

Sample name	Type	$r$ (nm)	PD (%)	$\zeta$ (mV)	
Core-FITC	Core	197	2.6	-80	
CL1	Core-Layer	393	2.5	+31	
	CLS1	Core-Layer-Shell	445	3.0	-90
CL2	Core-Layer	387	2.0	+64	
	CLS2	Core-Layer-Shell	422	2.6	-82
	CLS3	Core-Layer-Shell	440	3.0	-80
Core-FITC2	Core	205	4.7		
Core-RITC	Core	157	6.0	-80	
CL-RITC	Core-Layer	379	3.0	+65	
	CLS-RITC	Core-Layer-Shell	457	3.0	-78

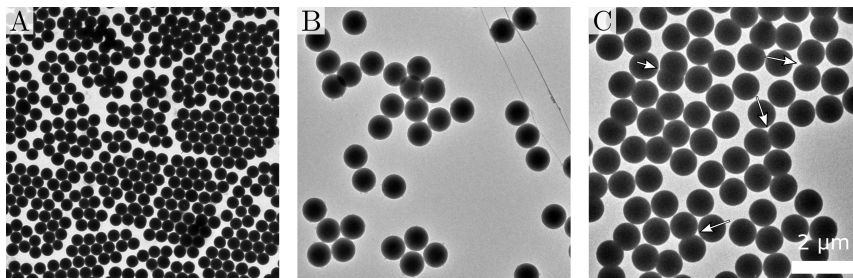


Figure 3.3: TEM images of particles CLS1: **A**, Core, **B**, Core-Layer, and **C**, Core-Layer-Shell particles. Additionally, several short (more overgrown) and long (less overgrown with silica) dumbbells are indicated with arrows in **C**. Scalebar is 2  $\mu\text{m}$ .

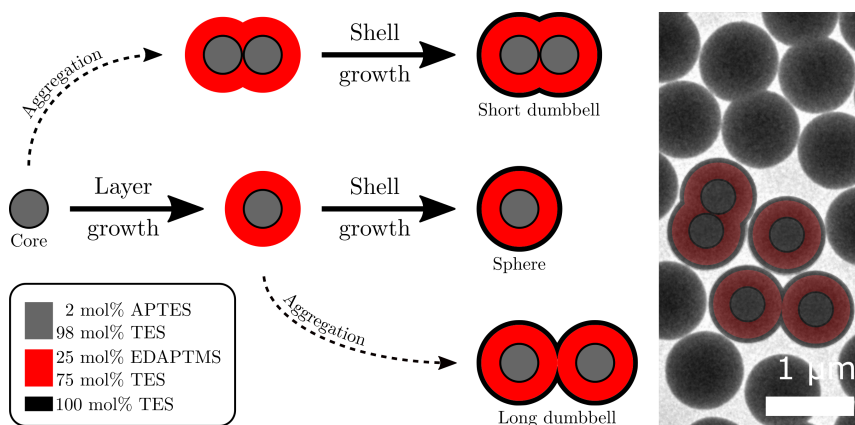


Figure 3.4: Schematic representation of the formation of short and long dumbbells during layer growth. Diagrams are overlaid on a TEM image, showing excellent agreement. Scalebar is 1  $\mu\text{m}$ .

During the growth of the layer and of the shell, some particles aggregated to form dumbbells, also indicated with arrows in Figure 3.3C. Particles that aggregated during the growth of the ormosil layer resulted in very overgrown dumbbells, which we will refer to as ‘short’ dumbbells to distinguish them from dumbbells that formed during the shell growth, which led to the formation of ‘long’ and less overgrown dumbbells. From the aspect ratio of these dumbbells, we determined that aggregation occurred at the earliest stage of the growth step, likely caused by the increase in conductivity in the initial stage of the synthesis.<sup>23</sup> The formation is schematically shown in Figure 3.4. The fraction of dumbbells varied between different batches; the highest fraction was found in CLS1 with 23% of the particles being long dumbbells. We suspect that dumbbells were formed during the cleaning steps in between ormosil layer growth and shell growth, where particles are taken from the Stöber mixture - containing ammonia - and redispersed in ethanol. It is known from literature that for the synthesis of RITC-labeled particles, the initial washing steps must be carried out with ammonia, and not pure ethanol.<sup>118</sup> Additionally, another method for making dumbbells also involves the destabilization of silica particles with ammonia and is combined with shearing the suspension.<sup>122</sup> Indeed, Core-Layer particles that were cleaned by centrifugation and redispersing in ethanol containing 30 mM ammonia had almost no dumbbells after the shell growth. It is likely that by using a specific pH during the washing steps, controlled aggregation and dumbbell formation can be achieved with these particles., although this may lead to the formation of larger aggregates as well.

In another experiment, the particle charge was monitored during the growth process. For this, a standard seeded growth Stöber mixture (30

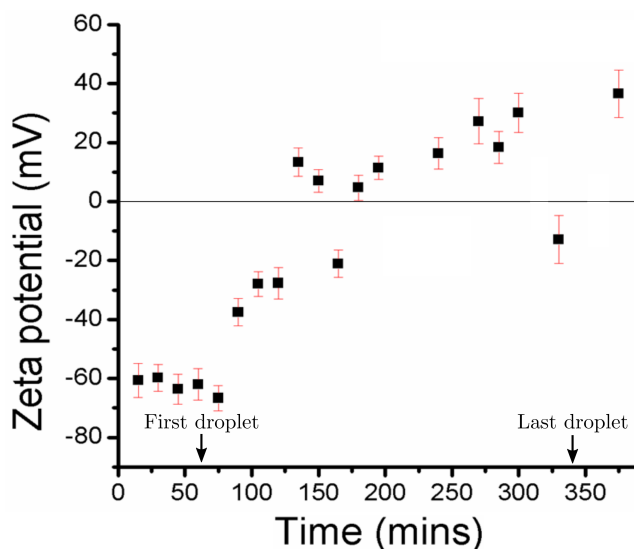


Figure 3.5: Particle (Core-FITC) charge during EDAPTMS growth. Between taking the sample from the reaction mixture and the measurement, the particles were washed and dispersed in water with 1.00 mM NaCl. Only points that were deemed reliable by the Zetasizer software were included.

mL) was prepared containing 0.067 v% seed particles (Core-FITC, radius 197 nm). A mixture of EDAPTMS in ethanol (1.8  $\mu\text{L}$  in 0.6 mL) was added over 270 minutes. Periodically, a small sample was taken from the reaction mixture, washed by centrifugation and redispersing twice in water with 1.00 mM NaCl, and its zeta potential measured using the Zetasizer. The zeta potential during the growth process is plotted in Figure 3.5. Data points that the Zetasizer software concluded were unreliable were excluded from the plot. Particle charge changed within 25 minutes after the addition of EDAPTMS, becoming at first less negative and eventually switching sign. The coating of EDAPTMS on the particles could not have been more than a few nanometers, because no TES was added along with EDAPTMS.<sup>121</sup> This demonstrates that even a thin (surface) coating of EDAPTMS is enough overcome the native negative charge on silica and even reverse the particle charge to positive.

### 3.3.2 HF etching experiments

The primary focus of our investigation was the difference in etching behavior between EDAPTMS-doped silica and pure Stöber silica. Chen et al. showed that silica doped with 0.4-4.3 mole % EDAPTMS (called TSD in their article) etched faster than pure silica in mild HF solution (0.10 wt% HF).<sup>101</sup> They used particles with a diameter of 460 and 645 nm and

Table 3.7: Overview of etching experiments. Unless otherwise stated, experiments were performed within 10 weeks of synthesis and using a particle concentration of 2.0 mg/mL.

No.	Particles	Etchant	Concentration	Time	Figure
1	CL1	HF	0.020 wt%	20 h	3.6
2	CLS1	HF	0.0025-0.070 wt%	20-48 h	3.7
	CLS1	HF	0.100 wt%	20 min	
3	CLS1	HF	0.100 wt%	20 min	3.8
	CLS2	HF	0.100 wt%	6-10 min	
	CLS3	HF	0.100 wt%	10 min	
4	CLS1	HF	0.018, 0.030 wt%	20 h	3.11
	CLS1	HF	0.100 wt%	3 min	
5	CLS1_aged*	HF	0.070 wt%	20 h	3.12
		HF	+0.020 wt%	95 h	
		HF	+0.050 wt%	66 h	
6	CLS1	HF	0.020 wt%	20 h	3.13
	CLS-RITC	HF	0.020 wt%	20 h	
7	CLS1	NaOH	0.025-4.0 mM	24 h	3.14
8	CLS1	NaOH	4.0 mM	24 h	3.15
		HF	0.020 wt%	5 min	
9	CLS1	Water**	-	96 h	3.16

\* = 13 months old

\*\* = 1.00 mM NaCl, 0.1 mg/mL particles

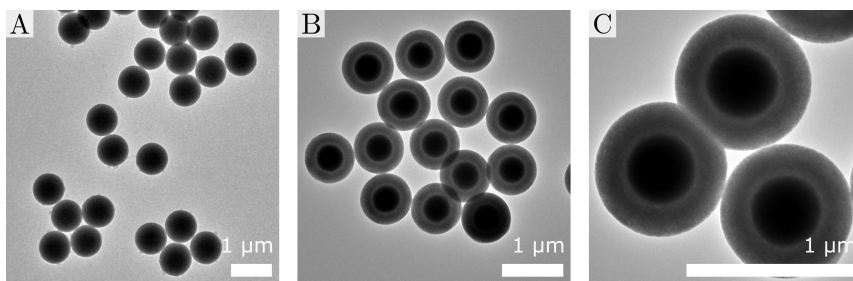


Figure 3.6: Etching no. 1: etching of particles (CL1) without an outer silica shell. **A**: before, and **B,C**: after etching with 0.020 wt% HF for 20 hours. Scalebars are 1  $\mu\text{m}$ .

etched in HF solution for 10 minutes (2.0 mg/mL particle concentration). We increased the EDAPTMS content of the ormosil layer in an attempt to increase the HF etching sensitivity even further. We will first present the effect of HF etching on unprotected ormosil layers, i.e. without an outer silica shell. Next, we studied the changes in particle morphology and charge as a result of HF etching between 0.0025 wt% and 0.100 wt%. We noticed different behavior between single spheres and dumbbells (both long and short), and between fresh (10 weeks after synthesis) and aged particles (13 months). An overview of all etching experiments is shown in Table 3.7. Etching experiments were conducted in plastic Corning centrifuge tubes using a particle volume fraction of 2.0 mg/mL and typical etching time of 20 hours.

### HF etching of Core-Layer particles

Core-Layer particles (CL1) were etched in 0.020 wt% HF for 20 hours. TEM images of the particles before and after etching are shown in Figure 3.6. From the reduced contrast of the ormosil layers (compared to the core) it is clear that the only ormosil layers had been etched. Additionally, the ormosil layer etched homogeneously from all sides and there appeared to be no difference between etching of dumbbell particles and single spherical particles (see Figure 3.6C). Particle diameter remained unchanged within experimental error. Therefore, like Chen et al.,<sup>101</sup> we also found that the EDAPTMS-doped layer etched faster than pure Stöber silica.

### HF etching of Core-Layer-Shell particles

Particles with an outer silica shell of 52 nm (CLS1) were etched in the range of 0.0025-0.100 wt% HF, demonstrating preferential etching of the ormosil layer, see Figure 3.7. The particle diameter remained unchanged during etching. The etching process appeared to have come to completion

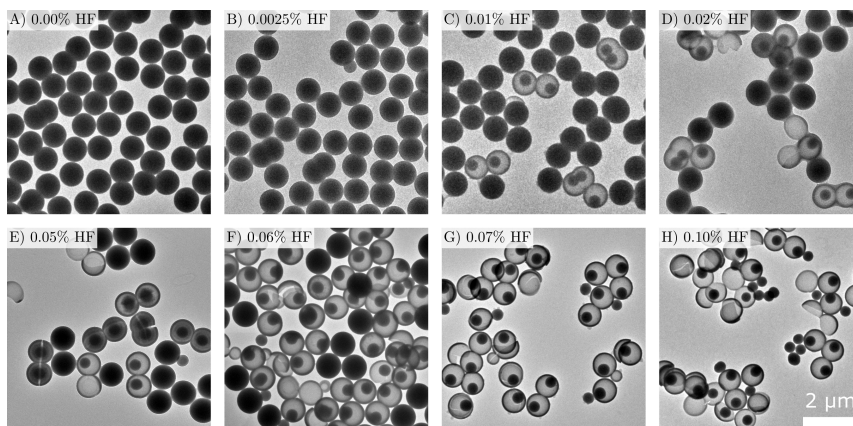


Figure 3.7: Etching no. 2: etching of Core-Layer-Shell particles (CLS1) at various HF concentrations. **A**: before etching, **B**: 0.0025 wt% for 48h, **C**: 0.010 wt% for 48h, **D**: 0.020 wt% for 48h, **E**: 0.050 wt% for 48h, **F**: 0.060 wt% for 48h, **G**: 0.070 wt% for 20h, **H**: 0.100 wt% for 10 mins. Scalebar is 2  $\mu\text{m}$ .

within minutes based on TEM images taken at different times of the same sample and changes in turbidity after HF addition. Chen et al. had used an etching time of 10 minutes for their experiments.<sup>101</sup> The optimal HF concentration appeared to be 0.07 wt%, which resulted in complete removal of the ormosil layer from all of the particles while leaving the pure silica core and outer shell intact and apparently unaffected, i.e. no obvious removal of material. This is surprising, because under these conditions the Si:F ratio is 1:1.44, which is much lower than the complete etching reaction stoichiometry of 1:6 (Si:F).<sup>116,117</sup> If we only consider etching the ormosil layer, then the Si:F ratio becomes 1:2.77. We speculate that at this ratio, enough siloxane bonds can be broken to detach silicate oligomers from the rest of the silica matrix, removing it from the particle. These oligomers can still be etched further in solution of enough HF is present (see paragraph 3.3.2 below) or may be washed away. Moreover, we conclude from these calculations that HF is completely consumed, automatically terminating the reaction.

Etching particles using 0.100 wt% HF resulted almost exclusively in broken shells, see Figure 3.8A-C. Additionally, we observed partially etched core particles, depicted Figure 3.8D-F. As mentioned, the core particles were synthesized with 2.0 mole % of the silane coupling agent APTES (for covalently binding the fluorescent dye) and were coated with a thin ‘pure’ silica layer afterwards, giving it a similar core-shell structure. Moreover, the outer surface of silica particles is known to harden over time.<sup>111</sup> The etched core particles were found most frequently inside short dumbbells, because these were the first to become etched, allowing HF to reach the

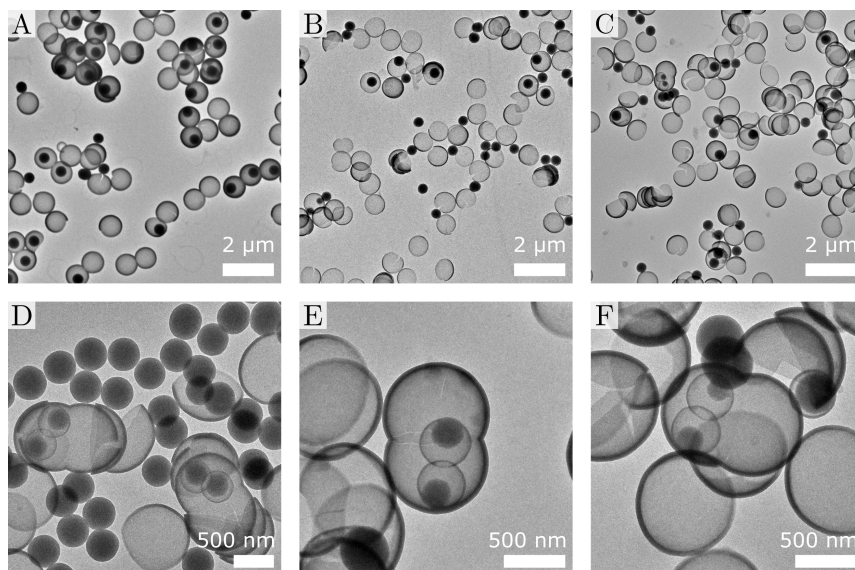


Figure 3.8: Etching no. 3: excessive etching of particles (CLS1). General overview images are shown in the top (**A**: CLS1, 0.100 wt% HF, 20 min. **B**: CLS2, 0.100 wt% HF, 10 min. **C**: CLS3, 0.100 wt% HF, 10 min. Scalebars are 2  $\mu\text{m}$ ). At these HF concentrations, etching of the core particles was also observed, shown in the bottom images (**D**: CLS2, 0.100 wt% HF, six min. **E**: CLS3, 0.100 wt% HF, 10 min. **F**: CLS3, 0.100 wt% HF, 10 min. Scalebars are 500 nm). Etched core particles were found most frequently inside short dumbbells.

cores (see below).

Furthermore, the structure of the silica shell appeared to be critical in determining the etching behavior of the particles. Below, we will discuss observations relating to the outer silica shell in more detail. First, there appeared to be two different pathways for the etching to occur: homogeneously through the shell, or from a single point. Second, etching behavior of dumbbell particles was different from that of single spherical particles. Third, particles that were aged for 13 months required more HF remove the ormosil layers.

**Homogeneous and defect etching pathways** After etching, some ormosil layers showed reduced contrast in the TEM images, while for other particles the layer was partially removed with the remaining layer showing no reduction in contrast. Additionally, we noticed that etching experiments in the range of 0.020-0.050 wt% HF resulted in a mixture of etched and unetched particles. In other words, there was a spread among the particles in how well the outer shell shielded the ormosil layer from the HF, and once breached, whether the inner ormosil layer became accessi-

Table 3.8: Percentages of particles CLS1 etching homogeneously or through a defect in HF concentrations from 0.005 to 0.070 wt% for 20 hours. Not enough spherical particles were observed in a partially etched state to determine etching pathway percentages.

HF (wt%)	Short dumbb. (%) 	Long dumbb. (%) 	Spheres (%) 
0.005-0.010	20	77	0
0.020-0.050	0	3	1
0.060	0	0	24
0.070	0	0	75

ble from a single point through the shell, or from all directions equally. An overview of the various stages of spheres, short dumbbells and long dumbbells etching through a defect in the shell is shown in Figure 3.9, and for homogeneous etching in Figure 3.10. In the case where short and long dumbbells etched through a defect in the shell, the position of this defect was almost always located in the neck region, where the two spherical lobes come together. Apparently, the neck concave region was secluded enough that less silica was deposited compared to the other parts of the shell. This is remarkable, because it has been found that for convex particles particle growth occurs in proportion to the surface area, resulting in the same rate of growth independent of particle size.<sup>24</sup> The locally thinner shells apparently had a higher probability of defects and a higher etching rate. The larger fraction of defective long (less overgrown) dumbbells compared to short dumbbells is consistent with this formation mechanism. Spherical particles do not have such a neck region and were found to etch only almost exclusively at higher HF concentrations (above 0.060 wt%).

Table 3.8 summarizes the percentage of particles (CLS1) that showed signs of etching (clear removal of material or reduction in contrast) for different HF concentrations. Additionally, the particles are split up by etching pathway, defect or homogeneous. We found too few spherical particles that were in the process of etching to determine a distribution of etching pathways, which indicates that there was likely no large difference. At low HF concentration, only dumbbells (short and long) became etched and at higher HF concentration the fraction of etched particles increased. In the range of 0.020-0.050 wt% HF, this sometimes resulted in the peculiar situation that by using a high concentration of HF, actually fewer ormosil layers were completely removed, due to the increase in the number of particles consuming HF. In these cases, the layers were only partially removed. Figure 3.11 shows etching experiments performed on

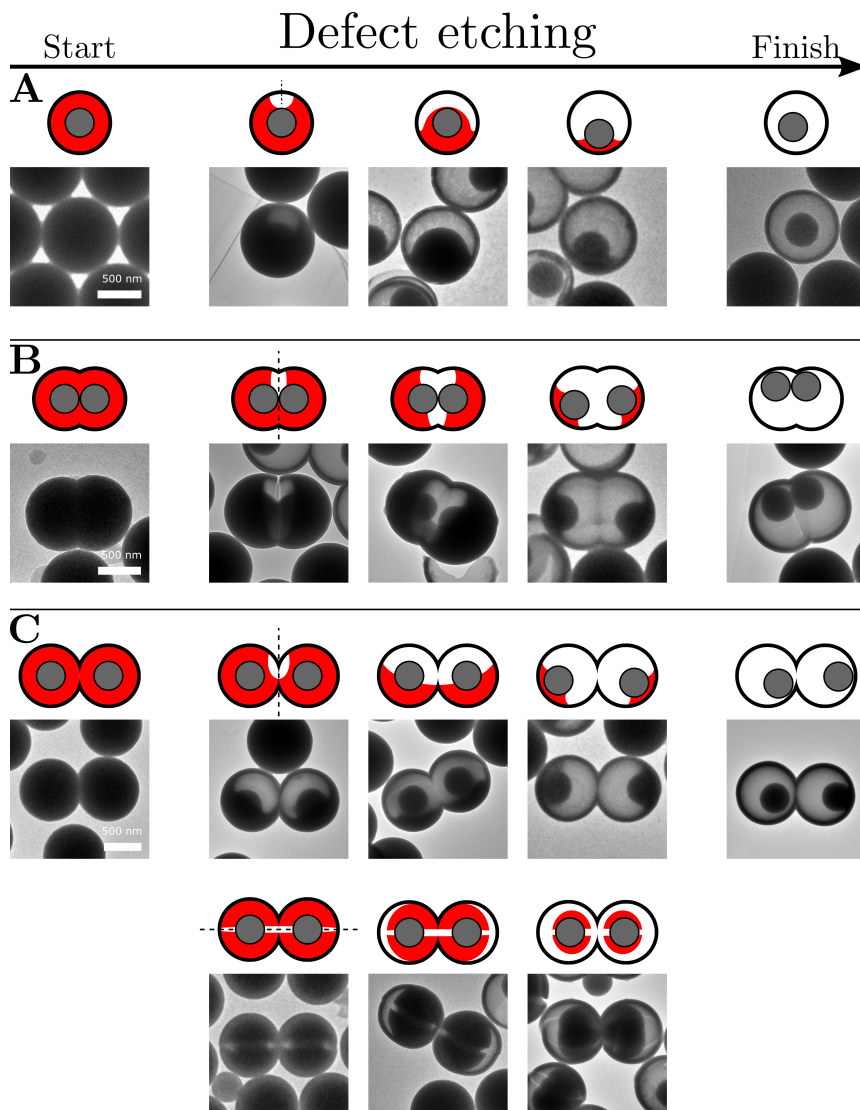


Figure 3.9: Schematic representation of spheres (A), short dumbbells (B) and long dumbbells (C) etching through a defect in the shell. Accompanying TEM observations from various experiments are shown below the diagrams. Long dumbbells showed two different defect etchings, either originating from the neck region between the spherical lobes (top) or through a crack in the shell along the long particle axis (bottom). Scalebars are 500 nm.

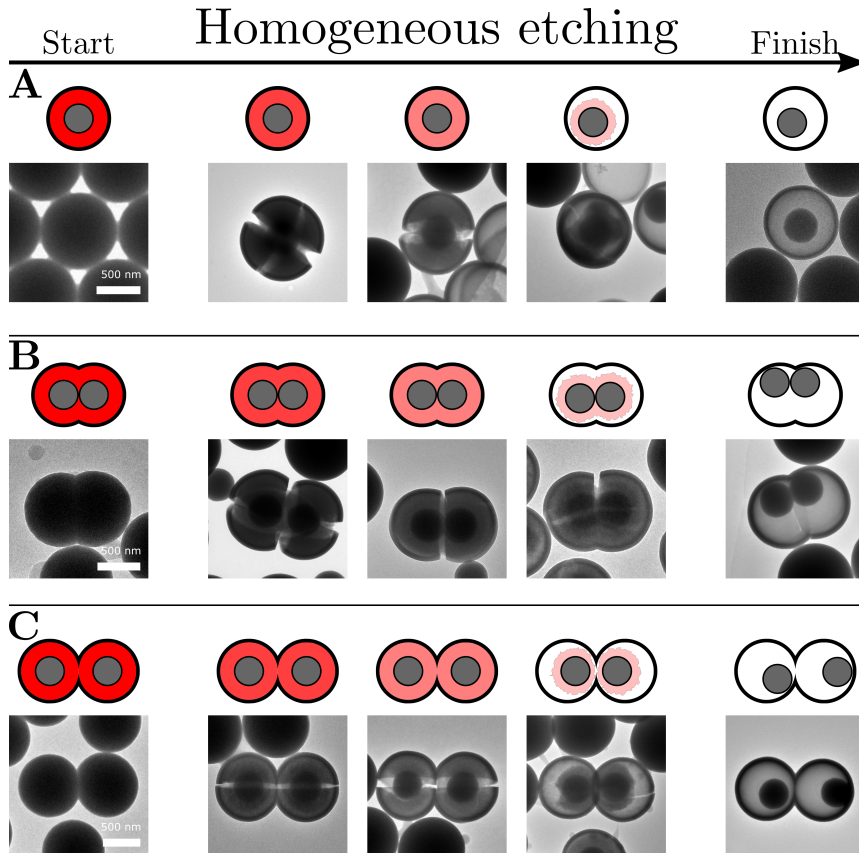


Figure 3.10: Schematic representation of spheres (**A**), short dumbbells (**B**) and long dumbbells (**C**) etching homogeneously from all directions. Accompanying TEM observations from various experiments are shown below the diagrams. Partially etched particles were often fractured during drying on the TEM grids. We hypothesize that these cracks formed upon drying; had they been present in the solution, the particles would not have etched homogeneously. Scalebars are 500 nm.

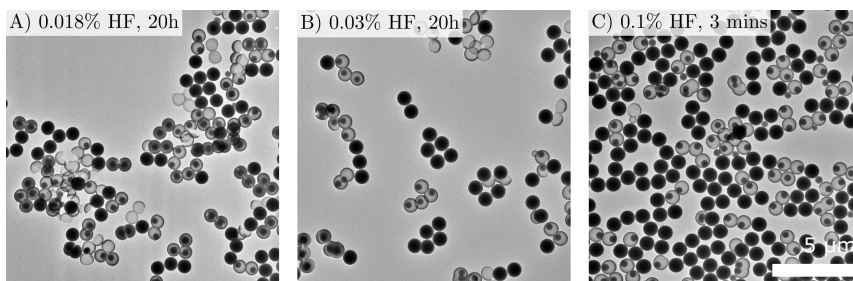


Figure 3.11: Etching no. 4: dumbbell particles (CLS1) etched at an earlier stage. Particles in a solution of HF of 0.018 wt% for 20h (A), 0.030 wt% for 20h (B) and 0.100 wt% for 3 mins (C). Scalebar is 5  $\mu\text{m}$ .

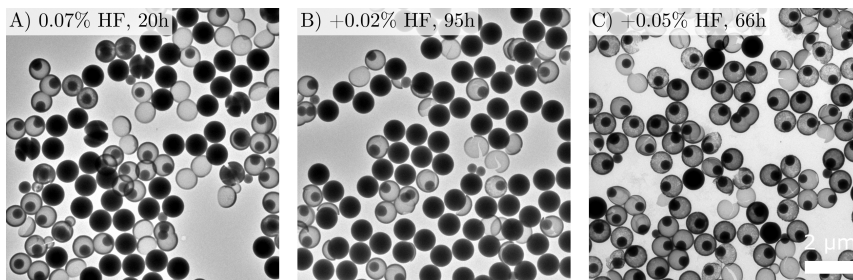


Figure 3.12: Etching no. 5: particles (CLS1<sub>aged</sub>) etched 13 months after synthesis (stored in ethanol) in sequential steps without washing. A, first etching with 0.070 wt% HF for 20h, B, second etching with 0.020 wt% HF for 95h, C, third etching with 0.050 wt% HF for 66h. Scalebar is 2  $\mu\text{m}$ .

CLS1 particles at 0.018, 0.030 and 0.100 wt% HF. At 0.100 wt% HF, all particles - including all spherical particles - became etched after 10 minutes. However, as can be seen from Figure 3.11C, after three minutes the spherical particles were not yet etched, whereas the dumbbells were, demonstrating that the dumbbells became etched both earlier and at lower HF concentration than spherical particles.

**HF etching of aged particles** Experiments shown in previous sections were all performed within 10 weeks of particle synthesis. However, 13 months after synthesis, the same particles (CLS1) showed different etching behavior. Aging effects on yolk-shell particles (containing a gold core particle) have been observed before.<sup>123</sup> These aged particles had been stored in ethanol in the dark during this period and the particle diameter had not changed. Figure 3.12A shows a TEM image of these aged particles (CLS1<sub>aged</sub>) etched using 0.070 wt% HF. Whereas for CLS1 (within 10 weeks of synthesis) these conditions resulted in complete removal of all ormosil layers (see Figure 3.7G), in the case of CLS1<sub>aged</sub>, a mixture

of completely etched, partially etched and unetched particles was found. Additional etchings were performed - without washing the particles in between successive etchings - to convert the majority of the aged particles into yolk-shell particles, shown in Figure 3.12B and C. We explain these results by a further condensation of the outer silica shell during this time, which is known to occur under thermal treatment,<sup>124</sup> electron irradiation,<sup>125</sup> and simply over time.<sup>111</sup>

### Particle zeta potential after HF etching

Two batches of Core-Layer-Shell particle, CLS1 and CLS-RITC, were etched with HF in the range of 0.001-0.050 wt% HF for 20 hours. After etching, the particles were washed, redispersed in water containing 1.00 mM NaCl, and the zeta potential of the particles was measured using the Zetasizer. The particle zeta potentials are plotted in Figure 3.13. Initially, both batches of particles had a surface potential of -80/-90 mV, typical of Stöber silica. As the particles were etched with higher concentrations of HF, the charge became more positive. We attribute the shift in the data between the two different batches of particles to the different shell thickness (52 and 78 nm, see Table 3.6. Already after mild HF etching (0.008-0.010 wt%), the zeta potential had changed to +60/+80 mV in both experiments. We found a linear trend between the HF concentration and the surface potential over a large range (0.001-0.006 wt% for CLS1, and 0.003-0.008 wt% for CLS-RITC). Interestingly, no structural changes were observed in the majority of the particles in this HF concentration range (see Section 3.3.2, Figure 3.7), indicating that removal of material from the particle did not play a role in this change. Above 0.012 wt% HF, when structural changes started to occur in CLS1, the charge remained strongly positive and eventually decreased slightly to +40 mV.

Additionally, a photograph of CLS-RITC after 20 hours of HF etching is shown in Figure 3.13B. It clearly shows a range of HF concentration (0.006-0.009 wt%) where destabilization was observed macroscopically, highlighted blue in the graph and photo. This concentration range corresponded to the region of low positive particle charge. We hypothesize that the faster sedimentation in the blue region was due to heteroaggregation, caused by some of the particles changing sign while others still remained negatively charged. These oppositely charged particles would then attract one another, cluster and sink. We expect that at higher HF concentration, all of the particles changed sign simultaneously, keeping all the particles electrostatically repulsive.

From this, we conclude that for the vast majority of the particles, the shell was initially closed and protected the ormosil layer (thicker shells providing longer protection). When exposed to HF, the shells were slightly etched and became permeable for ions and larger soluble species.<sup>74</sup> Subsequently, the amine groups in the ormosil layer became accessible, resulting in a reversal of the particle charge to +60/+80 mV. The decrease in

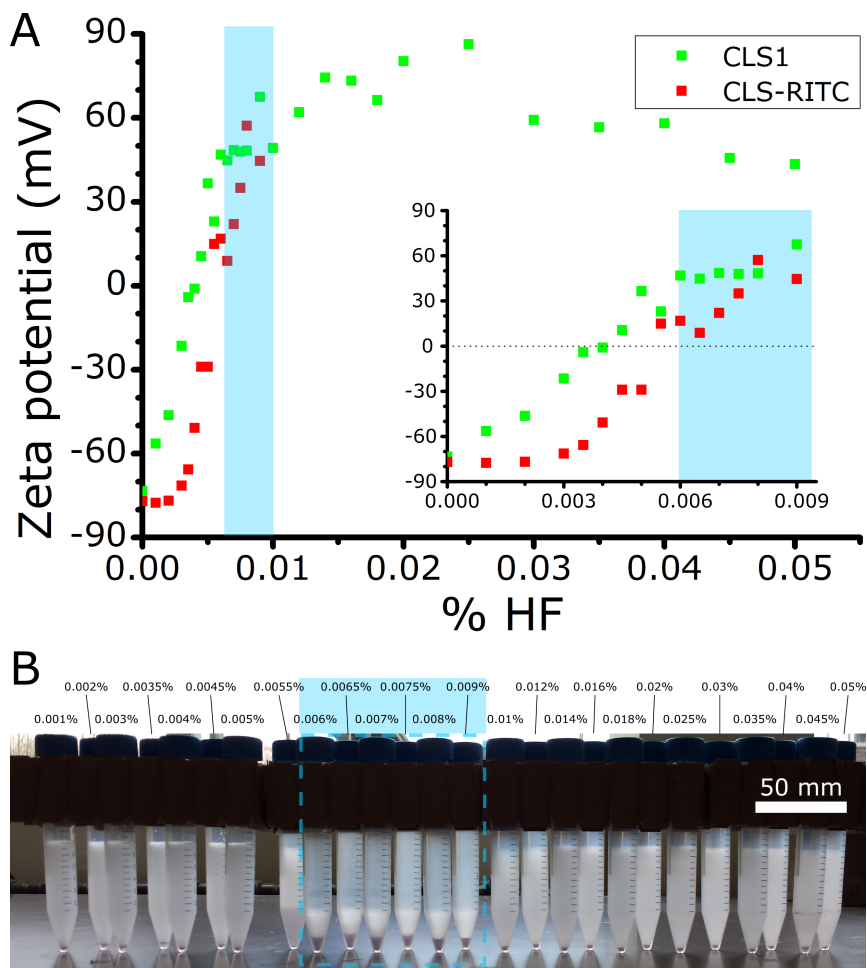


Figure 3.13: Etching no. 6: particle charge after etching. **A**: Zeta potential of particles CLS1 and CLS-RITC etched with HF concentrations from 0.001-0.050 wt% for 20 hours. **B**: Photograph of CLS-RITC after etching (scalebar is 50 mm). In the range from 0.006-0.009 wt% HF (highlighted blue) the particles aggregated and sedimented faster than in other concentrations.

particle charge at the highest HF concentrations was likely caused by a reduction in the number of amine groups due to physical removal of the ormosil layer from the particle (see Section 3.3.2). Even after etching at high HF concentration (0.070 wt% and higher), particles CLS1 remained positively charged, indicating that some of the EDAPTMS must have remained connected to the pure Stöber core and/or shell, giving it a net positive charge. Additionally, it is possible that some of the EDAPTMS redeposited on the pure Stöber silica shells and/or core particles. Figure 3.5 demonstrates that even a thin (surface) coating was enough to reverse the particle charge.

The particle design of layers with alternating charge allowed for careful tuning of the net particle charge by controlled HF etching, evidenced by the smooth and linear increase through zero shown in Figure 3.13A. Particle size can be carefully controlled through the synthesis, allowing for the preparation of different batches of particles with precise size ratios. HF etching only affected particle charge, not the size. The ability to independently adjust particle charge and size will allow for greater control when preparing crystals of oppositely charged particles, where both size and charge ratios affect the crystal structure.<sup>5</sup> Additionally, due to the spatial distribution of the different charging groups (negative silanol groups in the shell, positive amine groups in the ormosil layer), the potential outside the particle can also be influenced through the ionic strength. For example, if the Debye screening length is short, then the inner groups will no longer contribute to the potential outside the particle.

### 3.3.3 Base etching

In addition to etching with HF, particles (CLS1) were also etched using base (NaOH). Under these conditions, the etching behavior of the pure Stöber silica and the ormosil layer was very similar; both materials etched at roughly the same rate. Figure 3.14 shows TEM images of particles etched in NaOH solution between 0.025 and 4.0 mM. The particles etched from the outside inwards, leaving a rough surface, with no apparent difference in etching rate between ormosil and pure Stöber silica. In contrast to HF etching, under these conditions the neck area of the long dumbbells etched more slowly, maintaining a bridge between the two shrinking lobes while the rest of the particle continued to etch. This is reminiscent of another study on monolayers of close-packed silica particles that were etched with mild buffered HF solutions.<sup>126</sup> The authors also observed that the points where the particles touched remained intact. The layer slightly undercut the shell in the neck area, showing that it etched marginally faster than the pure Stöber silica shell. Only the outer surface showed etching (no hollowing out), even after the shell had been completely removed. From this, we concluded that in base, both types of silica etched at (almost) the same rate and thus quite differently from HF etching.

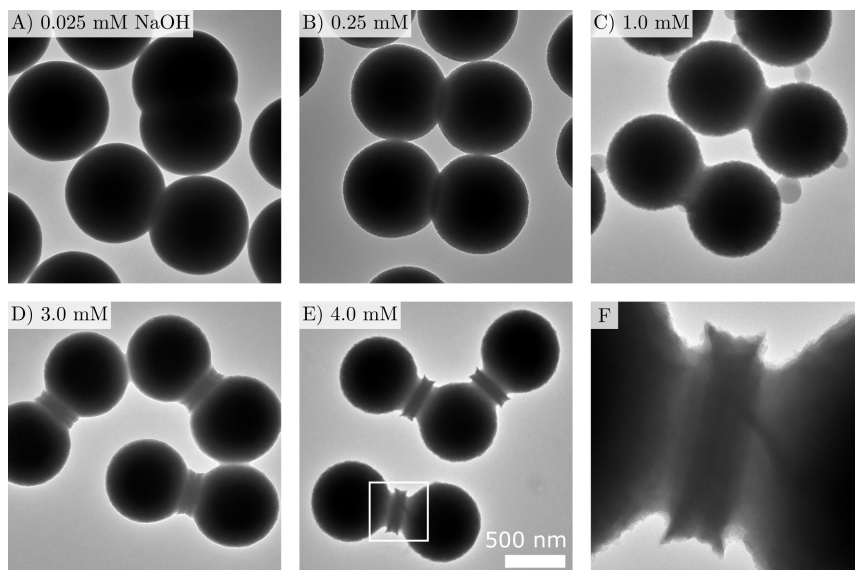


Figure 3.14: Etching no. 7: etching of particles (CLS1) with NaOH for 24 hours at various concentrations. **A**, 0.025 mM, **B**, 0.25 mM, **C**, 1.0 mM, **D**, 3.0 mM, **E**, 4.0 mM. A close-up of the neck region indicated in **E** is shown in **F**. Scalebar is 500 nm.

### 3.3.4 Combined etching

By combining different etching agents/conditions and utilizing the relative etching rates of EDAPTMS-doped and pure silica in these solutions, we were able to selectively remove specific parts of the particle and thereby synthesize shapes not dictated by the Stöber silica growth mechanism. CLS1 particles were etched in two steps. First, they were etched in 4.0 mM NaOH (shown in Figure 3.14E and F), which completely removed the outer silica shell except for the small section in the neck region of the long dumbbells. After three washing steps (centrifugation and redispersion in water) the particles were etched in 0.020 wt% HF for five minutes and subsequently washed and stored in ethanol. The resulting particles are shown in Figure 3.15. The HF etching completely removed the ormosil layer, leaving the pure silica unaffected. This left the cores of the CLS1 particles alongside the pure silica part of the neck regions of the long dumbbells. This demonstrates that new shapes (such as the rings from the necks) can be realized by combining EDAPTMS-doped silica with pure Stöber silica and subsequently etching in different media.

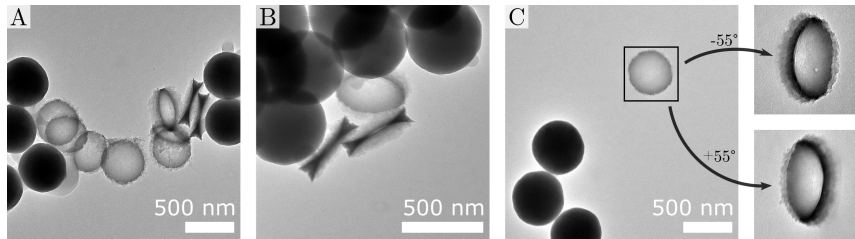


Figure 3.15: Etching no. 8: combined etching of particles (CLS1). Particles were first etched with 4.0 mM NaOH for 24 h, washed and then etched with 0.020 wt% HF for five minutes. Images under positive and negative tilt angle clearly show the shape of these ring-like objects. Scalebars are 500 nm.

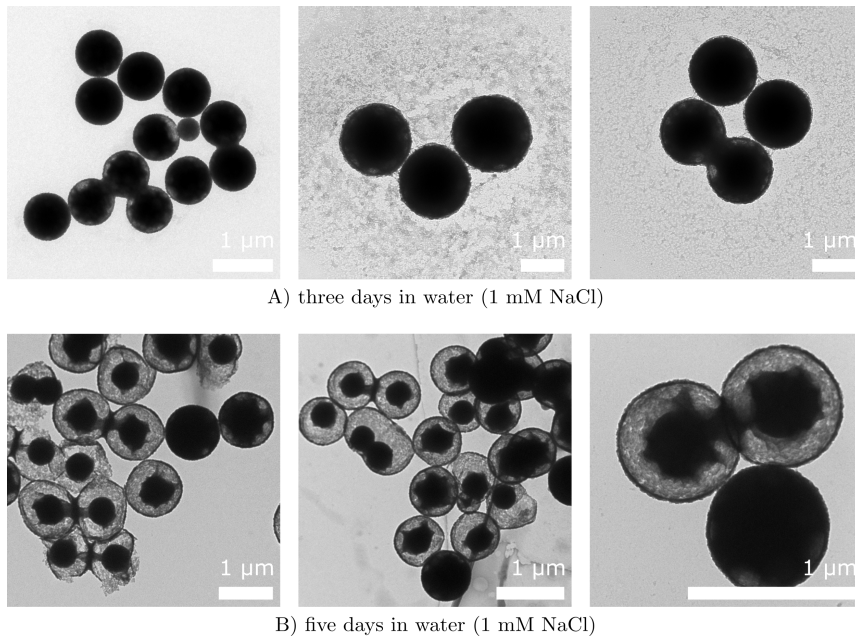


Figure 3.16: Etching no. 9: particles (CLS1) stored in water with 1.00 mM NaCl. **A**: three days, **B**: five days. Scalebars are 1  $\mu\text{m}$ .

### 3.3.5 Water etching

Surprisingly, deionized water at room temperature proved to be enough to etch particles containing an EDAPTMS-doped layer after several days. Cleaned particles (CLS1) were transferred from ethanol to water containing 1.00 mM NaCl by centrifugation. After three days, the particles had clearly become etched, as shown in Figure 3.16, even in the absence of any etching agent. Both the EDAPTMS-doped silica and the pure Stöber silica were affected; shells appeared rough and porous, and the ormosil layer partially remained in an irregular distribution inside the particle. The coarse structure of the shells is reminiscent of particles etched with base. We hypothesize that this was caused by the high concentration of EDAPTMS amine groups in the ormosil layer which locally increased the pH. The  $pK_a$  of these groups, when protonated, is around 10.6, meaning they will be protonated in water and thereby make the environment more alkaline. The locally elevated pH would then have resulted in a slow etching process resembling that of etching in NaOH solution.

## 3.4 Conclusions

We have demonstrated that HF etching of silica particles containing an ormosil layer allowed for the particle charge to be gradually changed from negative to positive and that further HF etching resulted in preferential removal of the ormosil layer producing yolk-shell particles. We increased the mole fraction of EDAPTMS in the ormosil layer to 0.22-0.25, as measured by ICP and TGA. The higher SCA content in the ormosil layer offered greater contrast in etching sensitivity than was found previously for up to a mole fraction of 0.04.<sup>101</sup> Beyond a mole fraction of 0.25, particle growth was found to be impaired. The outer silica shell was found to be primarily responsible for way in which the particles became etched. Etching occurred through two possible pathways: either homogeneously though all sides of the shell, or through a single point (defect). Dumbbell particles were more susceptible to HF etching and were found to etch both faster and from lower HF concentrations compared to single spherical particles. Additionally, the shell in the concave neck region of the dumbbells, where the two spherical lobes come together, was often weaker/thinner which resulted in defect-type etching. Apparently the normal homogeneous layer thickness for Stöber seeded growth was not achieved in these concave regions between two touching spheres. The amount of HF required to completely dissolve all of the ormosil layers equated to a Si:F ratio of 1:2.78 (assuming the pure silica remained unaffected). We hypothesize that (organo-)silicate species were incompletely etched to oligomers that detached from the matrix and went into solution as larger soluble ions. Particles aged in ethanol for 13 months required more HF to etch to completion. The differences between the permeability of the outer shells of different particles also be-

came larger after aging. We attribute this to the slow densification that is known to occur in Stöber silica, in particular near the particle surface, a process that is known to occur over time.<sup>94, 111</sup> Ideally, for future studies, better control over the structure of the Stöber silica shell would allow for even more uniform etching. This may allow for stronger/thinner shells to be made while keeping the underlying ormosil layers accessible for rapid etching.

EDAPTMS-doped silica was found to etch at approximately the same rate as pure silica when etched in NaOH solution. By sequentially etching dumbbells with NaOH and HF solution, we were able to form silica nano-rings, demonstrating that the combination of different types of silica and different etching media offer a way to possibly synthesize particle with new shapes. Neutral water was enough to cause slow etching of the particles, similar to etching in base over the course of several days. We hypothesize that this was due to the basic amine groups of EDAPTMS, thereby locally increasing the pH.

Aside from the effect on the etching properties, EDAPTMS also affected the particle charge. The amine groups can counteract the negative charge of the silanol groups, and a thin (surface) coating was enough to reverse the particle charge from negative to positive. Additionally, the charge of Core-Layer-Shell particles containing an ormosil layer could be controllably changed from negative to positive by mild HF etching. We expect that this mild HF etching made the shell progressively more porous, allowing more of the amine groups to become protonated, thus changing the net particle charge. This reversal of particle charge occurred in the range of HF concentrations where no changes to particle morphology were observed. The separate control over particle size and charge offers new ways to form crystals of oppositely charged particles of specific size and charge ratios.

### 3.5 Acknowledgments

We wish to thank Chiara Raffaelli for performing many of the measurements and experiments. We also acknowledge Jessi van der Hoeven for the TGA measurements and Relinde Moes-van Dijk for help with the ICP measurements and Nina Elbers for careful reading of the chapter.

### 3.6 Appendix: HF concentration

Table 3.9: The resulting HF concentration in various commonly used units following the addition of 10 wt% HF solution to 10 mL of particle dispersion.

HF added ( $\mu\text{L}$ )	HF			
	(v%)	(mg)	(mM)	(ppm)
0	0	0	0	0
10	0.01	1.030	5.146	92.80
20	0.02	2.060	10.28	185.4
30	0.03	3.090	15.41	277.8
40	0.04	4.120	20.53	370.1
50	0.05	5.150	25.63	462.1
60	0.06	6.180	30.73	554.0
70	0.07	7.211	35.82	645.6
80	0.079	8.241	40.90	737.1
90	0.089	9.271	45.97	828.4
100	0.099	10.30	51.03	919.5

# 4

---

## Diffusion of colloidal particles in spherical shells

---

The yolk-shell particles synthesized in chapter 3 are used in this chapter to study the motion of a particle in confinement. The fluorescent core particles are imaged using confocal laser scanning microscopy and the images are analyzed using particle tracking computer code. Particle diffusivity is predicted to decrease as the cavity size decreases and as particle-wall separation decreases, although there is conflicting experimental evidence. We find that the motion of the core particle is slowed down more strongly than expected purely based on hydrodynamic coupling with the shell. We expect this is related to the electrostatic repulsion between the similarly charged core and shell which further confines the particle to the center of the shell. By varying the ionic strength we can tune the range of the repulsion and we find that at high salt concentration a repulsion-free region develops in the center of the cavity, characterized by a constant particle probability. However, the range of the electrostatic repulsion is found to be stronger than expected for all salt concentrations. We do not observe the predicted lower particle diffusivity close to the shell.

## 4.1 Introduction

One of the most universal phenomena of our finite-temperature world is diffusion. From atomic motion in condensed matter physics, the distribution of biologically active compounds within living cells, to the weather,<sup>127</sup> diffusion is - quite literally - everywhere. In the field of soft matter and the study of colloidal particles, diffusion occurs over convenient time and length scales and can be observed in real space, while maintaining many of the general features that also hold for atomic systems, such as temperature dependence and phase behavior. Therefore, colloidal particles are often used as model systems. The thermal fluctuations that give rise to Brownian motion have been understood and described well over a century ago. Since then, diffusion in more complicated geometries and surroundings has been studied, such as particles moving close to boundaries,<sup>128</sup> subdiffusive motion due to crowding,<sup>129</sup> and superdiffusive behavior in active particles.<sup>130</sup>

Diffusion close to other objects is relevant in many branches of nanoscience. For example, transport of reactants through the pores of catalyst carrier materials, droplets flowing through microfluidic channels, and colloidal particles sedimenting over an inclined wall are all affected by the presence of flow-restricting boundaries. The hydrodynamic coupling between the diffusing object and the boundary depends on the separation and the confinement geometry.<sup>131,132</sup> For simple and symmetric geometries, such as single or parallel walls, the coupling has been calculated.<sup>133</sup> Unfortunately, this has not been extended to complex or even arbitrary confinements. Aside from the hydrodynamic coupling, other interactions may be present, such as electrostatics, which also depend on the particle-wall separation. Therefore, the diffusion of colloidal particles enclosed on all sides by charged flow-restricting walls is fundamentally interesting and relevant to many fields of study. Moreover, this geometry can also be interpreted as particle diffusion in a (harmonic) potential well or an external field, which is applicable to many other situations.<sup>134,135</sup> Once these effects are characterized, the diffusive behavior of such particles can be used as sensors to determine local conditions such as temperature, viscosity, and ionic strength. Moreover, by manipulating confined particles with an external electric field, devices with switchable optics can be realized.<sup>136</sup>

A small particle enclosed inside a spherical shell, called a 'yolk-shell' particle, is an excellent system to study confined diffusion. Such particles can be prepared in large quantities, with good control over the size of both core particle and shell, and can be prepared out of many different materials.<sup>90</sup> A common material for the production of yolk-shell particles is silica, known for its excellent chemical, mechanical and thermal stability and biocompatibility.<sup>93</sup> In neutral conditions, silica is negatively charged.<sup>17</sup> However, by incorporating silane coupling agents during the synthesis, the charge can be adjusted and even reversed (see chapter 3). Silica yolk-shell particles are therefore excellent for studying the hydrody-

dynamic and electrostatic effects on confined translational diffusion. In the sections below, we will discuss hydrodynamic interactions in more detail, going from free diffusion to increasingly more confined diffusion, followed by electrostatic interactions.

#### 4.1.1 Diffusion, hydrodynamic drag and confinement

Colloidal particles that are dispersed in a liquid medium exhibit diffusion; a process that causes the particle to travel through the medium. Diffusion is caused by the molecules of the medium that collide with the particle. On average, the force on the particle will be constant from all directions. However, this force will not be exactly balanced at any specific point in time due to thermal fluctuations. Therefore, the particle experiences a fluctuating force in a random direction, causing it to move in that direction. The motion of the particle causes liquid to be displaced, which in turn results in hydrodynamic drag on the particle. The simplest case is that for a single, isolated, spherical particle. The equation relating (in three dimensions) the drag force,  $\vec{F}$ , to the particle velocity,  $\vec{v}$ , is known as the Stokes formula:<sup>137</sup>

$$\vec{F} = -(6\pi\eta a)\vec{v} \quad (4.1)$$

where  $\eta$  is the viscosity of the liquid and  $a$  is the particle radius. Relating the drag to the thermal fluctuations yields the famous Stokes-Einstein equation:

$$D = \frac{k_{\text{B}}T}{6\pi\eta a} \quad (4.2)$$

where  $D$  is the diffusion constant,  $k_{\text{B}}$  is the Boltzmann constant, and  $T$  is the absolute temperature. This equation describes the diffusion of a particle in a large reservoir of liquid; free diffusion. If the particle is charged, the cloud of counterions surrounding it could hinder its diffusion. In the event that the electrical double layer is large compared to the particle radius and the particle is highly charged, the ions in the double layer will not be able to respond fast enough to the Brownian motion of the particle.<sup>138</sup> In that case, particle diffusion is slowed down by the ion cloud, akin to the retardation force in electrophoresis.<sup>139</sup> However, the screening lengths in this work were small compared to the particle size and therefore this effect was negligible. The picture of unhindered diffusion changes when the particle is not moving in a reservoir, but close to another object. One of the simplest cases is that of a flat planar wall, which has been explored experimentally,<sup>131, 140</sup> theoretically,<sup>128, 141</sup> and by computer simulations.<sup>133</sup> The effect of the wall is twofold. Firstly, its presence restricts the flow of the liquid and thus alters the hydrodynamic drag on the particle. Secondly, it breaks the symmetry around the particle and as a result, the diffusion constant can now be decomposed in a component parallel and perpendicular to the wall. These diffusion constants are affected by the separation between the particle and the wall; the closer the particle

comes to the wall, the higher the hydrodynamic drag and the slower the particle will move. This is the case both parallel and perpendicular to the wall, although the effect is stronger in the perpendicular direction. The increased drag is quite long ranged. At a distance of three particle diameters from the wall, the diffusion constant perpendicular to the wall is 80% of that in the bulk.<sup>131,142</sup>

More restrictive geometries than a single wall have also been studied, such as placing the particle between two parallel planar walls or in a circular channel. These geometries are relevant for the field of micro-/nanofluidics. Similar to the single wall scenario, the diffusion constant is split up in two components, and diffusion is generally found to be slower closer to the wall, both in the parallel<sup>143</sup> and the perpendicular direction.<sup>132,144</sup> However, one study<sup>145</sup> reported a constant diffusivity along the axis of a narrow channel (twice the particle diameter) regardless of the proximity to the wall, while diffusivity perpendicular to the channel axis was found to decrease with off axis displacement. Besides the dependence on particle-wall separation, the diffusivity of particles confined in multiple directions is also affected by the ratio between the particle size and the width of the channel/wall separation. The diffusion constants decrease as the channel width/wall separation becomes smaller.<sup>132,146</sup>

Finally, a particle may be enclosed on all sides, such as a cylindrical or spherical cavity. Diffusion inside a spherical cavity has been investigated experimentally<sup>147</sup> and by numerical calculation.<sup>148</sup> An excellent overview of the different calculation techniques and their limitations can be found in Ref. [149]. In this geometry, the diffusion constant can be decomposed in a radial (towards or away from the center) and a perpendicular component (parallel to the curved surface). Also, the particle-wall separation and particle-cavity size ratio affect the diffusivity. Cervantes-Martínez et al. performed experiments on single polystyrene spheres diffusing in 3D inside water droplets. They compared the bulk diffusivity with those inside droplets for various droplet sizes and found that diffusion was slower (up to an order of magnitude) in smaller droplets. Moreover, they found that radial diffusion slowed down close to the wall, but that perpendicular diffusion (along the wall) was unaffected by the particle-wall distance. Simulations of a particle inside a cylindrical cavity showed slower diffusion in all directions,<sup>150</sup> although diffusive motion directly towards the wall (similar to the radial diffusion in the spherical cavity) was affected more strongly, matching well with experimental data.<sup>151</sup> Moreover, this was the case when approaching both the flat and the curved wall of the cylinder.

Overall, diffusion is well understood. The Stokes-Einstein relation is an excellent description for free diffusion, far from walls. In the presence of flow-restricting objects, diffusion becomes position and direction dependent. Diffusion slows down with decreasing separation, more strongly so for motion directly towards the wall. These effects are found for many geometries, such as single and parallel planar walls, cylindrical tubes and cavities, and in spherical confinement. When a particle is restricted from

both/all sides, the ratio of the particle size to the gap/cavity width affects the diffusivity at somewhat larger separations where the wall effects are not as steep. However, there is conflicting evidence regarding the diffusivity along the wall. While many theoretical and simulation studies have reported that the diffusion should decrease parallel to the wall as the separation becomes smaller, there are several experimental studies that report constant diffusivity in the direction along the wall, regardless of particle-wall separation.<sup>145, 147</sup>

There are several important differences between the systems used in these studies and the yolk-shell particles we used. First, in the studies mentioned above there were no electrostatic interactions, whereas in the present work the yolk-shell particles had similar charges on the core and shell which were screened by ions in the solution (details below). The second consideration is the nature of the confining wall. The shells of the yolk-shell particles were porous which allowed solvent molecules and ions to pass through, as opposed to the other reports where the impermeable PDMS walls and liquid-liquid interfaces that completely restricted solvent flow. Additionally, our silica shells were rigid while the liquid-liquid interface used in one of the studies was deformable, allowing frequent excursions beyond the theoretical interface position. Finally, our experimental setup projected 3D data onto a 2D plane. Therefore, we did not have access to the exact particle coordinates as they did in the 2D channels or in the spherical droplets.

#### 4.1.2 Electrostatic interactions

If the sphere and shell are both charged, they will also have (direct) electrostatic interactions besides the (indirect) hydrodynamic interactions described above. For charged particles in a medium containing ions, this electrostatic repulsion can be described using DLVO theory.<sup>7, 8</sup> For two charged spheres ( $i$  and  $j$ ), this takes the form of a Yukawa (screened Coulomb) potential that decreases with interparticle distance:

$$\frac{V_{ij}}{k_B T} = Q_i Q_j \lambda_B \frac{e^{\kappa(a_i + a_j)}}{(1 + \kappa a_i)(1 + \kappa a_j)} \frac{e^{-\kappa r}}{r} \quad (4.3)$$

with the Bjerrum length,  $\lambda_B$ , as:

$$\lambda_B = \frac{e^2}{4\pi\epsilon_0\epsilon_m k_B T} \quad (4.4)$$

Here,  $k_B$  is the Boltzmann constant ( $1.38 \cdot 10^{-23} \text{ m}^2 \text{ kg s}^{-2} \text{ K}^{-1}$ ),  $T$  is the absolute temperature (K),  $Q$  is the number of charges,  $\kappa$  is the inverse Debye screening length ( $\text{m}^{-1}$ ),  $a$  is the particle radius (m),  $r$  is the center-to-center distance between the particles (m),  $e$  is the elementary charge ( $1.60 \cdot 10^{-19} \text{ C}$ ),  $\epsilon_0$  is the permittivity of vacuum ( $8.85 \cdot 10^{-12} \text{ m}^{-3} \text{ kg}^{-1} \text{ s}^4 \text{ A}^2$ ),  $\epsilon_m$  is the dielectric constant of the medium.

By performing electrophoresis, the particle's electrophoretic mobility can be measured which yields the particle's zeta potential,  $\zeta$ . The zeta potential can be used to calculate the number of charges on the particle,  $Q$ , using the following equation (from Ref. [38], page 381, Eq. 8.2.24):

$$Q = 4\pi\epsilon_0\epsilon_m a \frac{\zeta}{e} (1 + \kappa a). \quad (4.5)$$

An important parameter in the DLVO potential is the Debye screening length,  $\kappa^{-1}$ , which largely sets the range of the repulsion and is determined by the concentration of ions (ionic strength):

$$\kappa = \sqrt{\frac{2N_A c e^2}{\epsilon_m \epsilon_0 k_B T}} = \sqrt{\frac{2\rho_{\text{ion}} e^2}{\epsilon_0 \epsilon_m k_B T}} = \sqrt{(8\pi\rho_{\text{ion}}\lambda_B)} \quad (4.6)$$

with  $N_A$  as Avogadro's number ( $6.02 \cdot 10^{23} \text{ mol}^{-1}$ ),  $c$  is the ion concentration in the bulk ( $\text{mol m}^{-3}$ ), and  $\rho_{\text{ion}}$  is the number density of ions ( $\text{m}^{-3}$ ). The ions surrounding the charged object 'screen' its charge, thus reducing the electrostatic potential and making the repulsion shorter ranged. This region is called the 'electrical double layer.' In the above treatment, we have assumed that the electrolyte valency is one.

When two charged objects approach one another and their double layers begin to overlap, the potential energy rises, and they will be forced apart. In the case of the electrostatic interactions inside of a yolk-shell particle, there are several charged surfaces in relatively close proximity. If the Debye screening length is small compared to the cavity size, then electrostatic forces will only be significant close to the wall and there will be a relatively force-free region in the center of the shell. As the Debye screening length becomes larger, the particle will be increasingly repelled by the shell and confined to its center. At the point where the double layer becomes so large that there is no more force-free zone, the concentration of ions inside the shell will become non-trivial and may start to deviate from that in the bulk. If that is the case, the Poisson-Boltzmann equation needs to be solved to obtain the distribution of ions and the potential as a function of distance. Additionally, by reinserting this potential back into the grand potential, the force on the particle at each position can be obtained. If the Debye screening length becomes much larger than the shell, the electric field inside the shell should be effectively constant as the repulsion from opposing sides cancels out, allowing the particle to completely explore the volume inside the shell.

In our yolk-shell particles, there was 700 nm of free space between the core particle and the shell, and the largest Debye screening length in our study was less than 30 nm. Therefore, we believe that we were in the regime where the electrostatic interactions only mattered close to the inner shell wall, that there was a force-free region in the center, and that the concentration of ions inside the shell was equal to that in the bulk.

## 4.2 Methods

In this section, we describe the measurements for determining the particle charge by microelectrophoresis, followed by the determination of solvent properties related to the Debye screening length. Finally, confocal imaging and the particle tracking routine are addressed. The synthesis procedure of the yolk-shell particles can be found in chapter 3.

### 4.2.1 Microelectrophoresis

Microelectrophoresis measurements were conducted by applying a DC electric field across a dispersion and measuring the particle velocity as a function of height with the confocal microscope.<sup>67</sup> We used a Leica SP8 confocal microscope with a 100x objective (NA = 1.4), equipped with a white light laser set to 495 nm. A glass capillary (borosilicate, 0.10x2.00 mm, Vitrotubes) with nickel electrodes approximately 20 mm apart placed inside (0.05 mm diameter wire, Goodfellow) was filled with particle dispersion and sealed with UV glue (Norland optical adhesive #68). The glue was polymerized under a UV lamp for approximately 10 minutes. The distance between the electrodes was measured on the motorized stage of the confocal microscope and free diffusion was recorded in the middle of the capillary to calculate the viscosity of the medium. Afterwards, the sample was allowed to equilibrate on a rotating stage to counteract sedimentation due to gravity. Once homogeneous, the capillary was placed back on the confocal microscope and a DC voltage was applied using a Krohn-Hite model 7602M wideband amplifier. After 30 seconds, an image stack was recorded from bottom to the top of the capillary ( $z$ -stack). This was repeated for several voltages. If necessary, the capillary was placed back in the rotating stage to homogenize the particle distribution. Using cross-correlation, the displacement (and therefore velocity) between frames was calculated. By doing so for the entire  $z$ -stack, we obtained a velocity profile across the whole capillary, which we could fit using a parabolic function.

The electric field induces a Poiseuille flow, where liquid close to the walls is flowing one way, and the liquid in the middle of the capillary is flowing in the opposite direction. Therefore, there are two positions where there is no net liquid flow, called the stationary planes, the positions of which are known. At the stationary planes, the particle mobility is purely the result of the particle charge and not of the flow of the surrounding liquid. By reading off the particle velocity from the parabolic profile at the stationary planes, we obtained the particle mobility and from that, the particle charge.

## 4.2.2 Solvent conductivity, salt concentration and Debye screening length

We measured the conductivity of the solvent using a Scientifica model 627 conductometer. 3.750 mL was added to the probe and we used the value of the conductivity 60 seconds after addition. Typically, three measurements were performed to determine the conductivity. After each measurement, the probe was rinsed with acetone (three times) and hexane (three times) to reach a base conductivity of 0.1-0.2 pS cm<sup>-1</sup>.

The conductivity can be used to calculate the concentration of ions in a dispersion. The conductivity is related to the ion concentration as follows:

$$\sigma = c\Lambda_0, \quad (4.7)$$

where  $\sigma$  is the measured conductivity (S m<sup>-1</sup>),  $c$  the concentration of dissociated salt (mol m<sup>-3</sup>), and  $\Lambda_0$  is the limiting molar conductance of the salt at infinite dilution (S m<sup>2</sup> mol<sup>-1</sup>). The total concentration of all ions in the solution is  $2c$ .

The limiting molar conductance can be estimated using an empirical formula known as Walden's rule.<sup>152,153</sup> This rule states that the product of the limiting molar conductance and the viscosity is (approximately) constant for the same species in different solvents:

$$\Lambda_0^A \eta^A = \Lambda_0^B \eta^B. \quad (4.8)$$

Here,  $\eta$  is the viscosity (Pa s). The superscript denotes the different solvents. In order to obtain  $\Lambda_0$  for our medium (glycerol water, 90:10 v/v), we used pure glycerol as a reference:  $\Lambda_0^{glycerol} = 2.71 \cdot 10^{-2}$  S cm<sup>2</sup> mol<sup>-1</sup>,<sup>154</sup>  $\eta^{glycerol} = 0.910$  Pa s (25 °C).<sup>155,156</sup> The viscosity of the sample medium was determined by measuring the free diffusion of core particles (radius 228 nm) in the middle of the capillary, which came to  $\eta = 0.2875$  Pa s. Using these values, we calculated the concentration of ions,  $c$ , and by using Eq. 4.6 we calculated the Debye screening length,  $\kappa^{-1}$ .

## 4.2.3 Particle tracking

Particles were identified by identifying bright spots in the microscopy image and fitting it with a Gaussian profile.<sup>63,64,157</sup> First, a Gaussian blur was applied over the image to reduce noise. Next, a Gaussian profile is fitted around the brightest pixel. The profile is shifted based on the intensities of the surrounding pixels. In this way, the center of this profile is taken as the exact particle position, with sub-pixel resolution due to the influence of the neighboring pixels. Once all particles in all frames are identified, they can be tracked in time by looking for particles in the next image within a certain maximum displacement (cut-off) of their previous location. Four checks were performed to prevent artifacts due to tracking or from the synthesis, such as incomplete removal of the interior inside the

shell. First, we looked for pixel bias. If there is not enough signal (pixels or brightness) per particle, the fitted Gaussian will preferably be placed on the edge between two pixels, thereby losing the sub-pixel resolution. To check for this pixel bias, a histogram was made of all the particle locations (in  $x$  and  $y$  separately) using the values *after* their decimal point. If the distribution is peaked around zero, then the code preferably finds particles on whole pixels. The histograms for our measurements were flat, showing that the code detects particles irrespective of the centers of the pixels.

Second, we checked whether the particle displacements in  $x$  and  $y$  were distributed properly and were not too large. This distribution should be Gaussian, symmetric and decay to zero.

Third, the core should explore the whole space inside the shell over the course of the measurement and should be evenly distributed throughout, provided that all interior material was removed correctly. We occasionally observed particles from which some internal material had not been removed completely, resulting in inaccessibility of certain regions for the core particle. The scatter plot should be circular and within the shell inner diameter, and the histograms should be symmetric. We used the average of all these locations as the center of the shell.

Finally, we use the particle displacements to plot the mean squared displacement (MSD), from which we calculate the short-time diffusion coefficient,  $D_s$ . Additionally, the slope of the MSD is used as an indicator of free or restricted diffusion.

### 4.3 Results and discussion

We used confocal microscopy and particle identification/tracking code to study the particle-wall interactions at various ionic strengths, and investigate whether the particle diffused more slowly close to the shell inner wall. We compared the diffusion in the bulk (far from walls) to that inside the shell, which is known to be slower. As described above, electrostatic repulsion between the particle and the wall (screened by ions in the solution) directly influence the forces on the particle and its diffusivity. Additionally, the diffusion constant is indirectly affected by hydrodynamic interactions, which are sensitive to the cavity geometry. These effects give rise to position-dependent diffusivity. For this study, we synthesized yolk-shell particles and imaged their motion. Below, the synthesis of yolk-shell particles will be presented, followed by measurements of the particle zeta potential. Subsequently, the particles were imaged using a confocal microscope and the images were analyzed using computer code in order to extract the particle location and motion. The tracking data were carefully checked to ensure that there were no artifacts due an inhomogeneous interior of the shell or due to the tracking procedure.

Table 4.1: Particle results for the yolk-shell particles at each stage of reaction. The diameter of the cores includes the non-fluorescent 20 nm layer.

Particle	Diameter (nm)	PD (%)	Remarks
Core	456	11	2% APTES-FITC
Core-Layer	1150	3.5	25% EDAPTMS
Core-Layer-Shell	1380	2.9	3% dumbbells

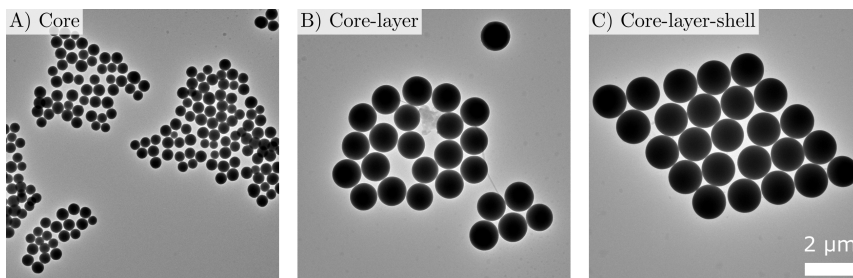


Figure 4.1: TEM images of Core-Layer-Shell particles at all stages. **A**: Core particles, **B**: Core-Layer, and **C**: Core-Layer-Shell. Scalebar is 2  $\mu\text{m}$ .

### 4.3.1 Particle synthesis and etching

Fluorescently labeled yolk-shell particles were prepared using a modified Stöber method.<sup>16,24,101</sup> The particle synthesis is described in more detail in chapter 3. Table 4.1 summarizes the particle dimensions at each stage of the synthesis, and TEM images are shown in Figure 4.1. The amine groups of the silane coupling agents can reduce the particle charge of silica and in some cases even invert it from negative to positive. Therefore, after the fluorescent cores were synthesized, an additional non-fluorescent silica layer of 20 nm was grown around the cores to improve their stability. The core-to-shell size ratio was 2.5. While the exact particle sizes (and ratios) can be easily tuned during synthesis, there are some restrictions. On the one hand, there is an upper limit to the shell size, related to the gravitational height of the core particle. If the shell is too large, the top of it will not be explored equally, especially for large core particles ( $\sim \mu\text{m}$ ). The gravitational height of the core particles used in this study was 10  $\mu\text{m}$ . Additionally, if the shell is larger than the point spread function of the confocal microscope (in the  $z$ -direction), then the core particle can diffuse out of view. This means

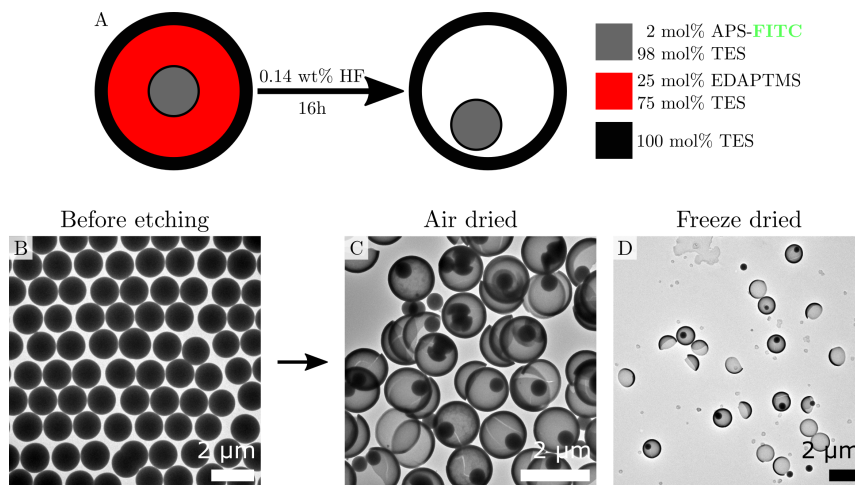


Figure 4.2: HF etching of Core-Layer-Shell particles using 0.14 wt% HF for 16 hours. **A**: Schematic representation, **B**: particles before etching, **C**: etched and air dried, **D**: etched and freeze dried. Scalebar is 2  $\mu\text{m}$ .

that recording data only in 2D is no longer sufficient and 3D data stacks have to be recorded, which deteriorates temporal resolution. However, our detector is sensitive enough that it can reliably detect particles that are several hundreds of nanometers above or below the focal plane. With regards to temporal resolution, the acquisition rate needs to be sufficient to ensure that small changes in particle position (especially close to the wall) can be recorded. For our experiments, the displacement expected based on free diffusion, which is certainly an overestimation, was 23 nm between frames (0.5 sec/frame). Our confocal microscope (Leica SP8) is equipped with a resonant scanner, allowing for frame rates up to 64-84 frames/sec for images of 256x256 pixels. Other microscopes, such as the VT-Infinity3, are even capable of reaching 1000 frames/sec. At these high frame rates, bleaching of the dye may become the limiting factor. The second consideration is the minimum size of the core particle. If the core is too small, it will move too fast to be tracked reliably, especially when it is close to the wall. Moreover, smaller core particles emit less light, making it more difficult to have enough signal to locate them with high precision, particularly for long tracks as they will also bleach more quickly. The combination of a minimum core size and a maximum shell size limits the core-shell ratios that are experimentally accessible. With the above in mind, a core-to-shell ratio up to 10 is achievable.

Once the particles were synthesized, the organo-silica layer had to be removed to obtain a freely moving core. We achieved this by etching with HF (Figure 4.2). During the etching process, the sacrificial layer was selectively removed through the (microporous) shell, keeping the pure Stöber

silica core and shell mostly unaffected. Additionally, the core retained its fluorescent dye after etching. Figure 4.2 shows TEM images of the particles before and after etching with 0.14 wt% HF for 16 hours (see chapter 3 for details). The majority of the particles were converted to yolk-shell particles by complete removal of their organo-silica layers. Alongside these particles were shell fragments and unconfined cores, indicating that a portion of the particles was destroyed during the etching procedure. Shell fragments and unconfined cores were also found after freeze drying (see Figure 4.2D), indicating that broken particles were already present in solution and were not caused by drying. These etching conditions appeared to be optimal; more HF led to more broken particles, and less HF left more particles not completely etched and with partially filled interiors. Because the surrounding solvent, and the ions dissolved in it, are of a similar size as the etching products, it is likely that the silica shell is permeable to both solvent and ions. This would allow the interior of the shell to freely equilibrate with the bulk phase. The high viscosity inside the shell, indicating that glycerol passed through the shell, supports this.

### 4.3.2 Zeta potential measurements

The core particle and the shell both carry a charge, resulting in an electrostatic interaction. As the core and shell are made of the same material (silica), they both carry the same charge which causes an electrostatic repulsion. This repulsion is screened by ions present in the solution, which can be varied experimentally, thereby varying the range of the interaction. However, the particle charge must also be determined in order to calculate the interaction strength. This is achieved by measuring the particle zeta potential, which is the particle charge together with the charge of the ions bound to it.

The zeta potential of the yolk-shell particles was measured in three different media: in pure water with 1.0 mM NaCl, as a reference, in a 5.5 mM ammonia solution, which is at elevated pH similar to Stöber growth conditions, and in glycerol/water (90:10 v/v) with 5.5 mM LiCl, which was the dispersing medium in our confocal studies. The two aqueous dispersions were measured using a Malvern Zetasizer. Figure 4.3 shows the curves obtained for neutral and elevated pH dispersions. At neutral pH, the particle zeta potential was positive, and at elevated pH (pH  $\approx$  10.5) it was negative. The charge of these particles is treated in more detail in chapter 3. In brief, we attribute this charge reversal to the deprotonation of the silane coupling agent amine groups at high pH. Primary and secondary amine groups, such as those in N-[3-(trimethoxysilyl)propyl]ethylenediamine (EDAPTMS), have a  $pK_b$  around 10.6, and will therefore be protonated (positively charged) at neutral conditions and about half deprotonated (less charged) at pH 10.5.<sup>158</sup> The net particle zeta potential is determined by the combination of the charge of the amine groups of the EDAPTMS silane coupling agent and the silanol groups of

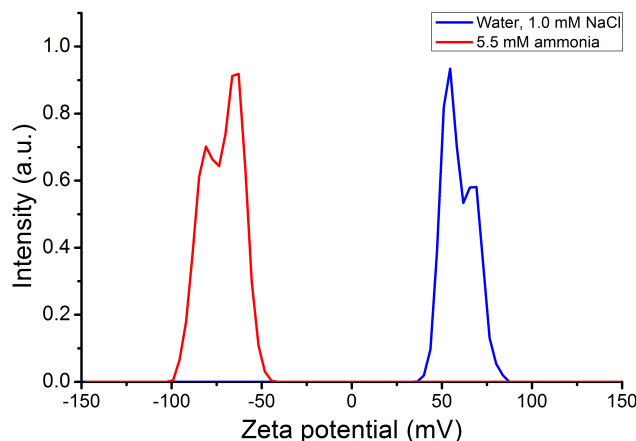


Figure 4.3: Zeta potential of etched yolk-shell particles obtained using the Malvern Zetasizer. In water with 1.0 mM NaCl at neutral pH, the particles were positively charged. In alkaline ammonia, the zeta potential was negative.

the silica. It is well established that the isoelectric point of Stöber silica is around pH 2.<sup>159</sup> Therefore, in the pH range considered here (7-11), these silanol groups will always be deprotonated and thus negatively charged.<sup>17</sup>

Both at neutral and elevated pH, the zeta potential measurement resulted two peaks with roughly the same intensity ratio. These may correspond to intact yolk-shell particles for one peak, and unconfined cores and shell fragments on the other. The cause of the formation of two peaks was not determined.

Complementary to the Zetasizer measurements, we also performed microelectrophoresis<sup>54,66</sup> on yolk-shell particles dispersed in glycerol:water (90:10 v/v). A capillary was filled with the particle dispersion and an electric field of 40.0, 60.0 and 80.0 V was applied, with an electrode separation of 19.3 mm. Subsequently, the movement of the particles was imaged using confocal microscopy by recording a  $z$ -stack from the bottom to the top of the capillary. Using image cross-correlation, the particle velocity was obtained at each  $z$ -position. The resulting mobility profiles are plotted in Figure 4.4 along with the fitted parabolic flow profiles. The dashed lines indicate the stationary planes of the Poiseuille flow, where the movement of the medium does not contribute to the particle mobility. The viscosity was determined by measuring the diffusion of the fluorescent cores prior to the electrophoresis measurement. Finally, the mobility was converted to a zeta potential using the following relation (for  $\kappa a \gg 1$ ):<sup>38</sup>

$$\mu = \frac{\epsilon_0 \epsilon_m \zeta}{\eta}, \quad (4.9)$$

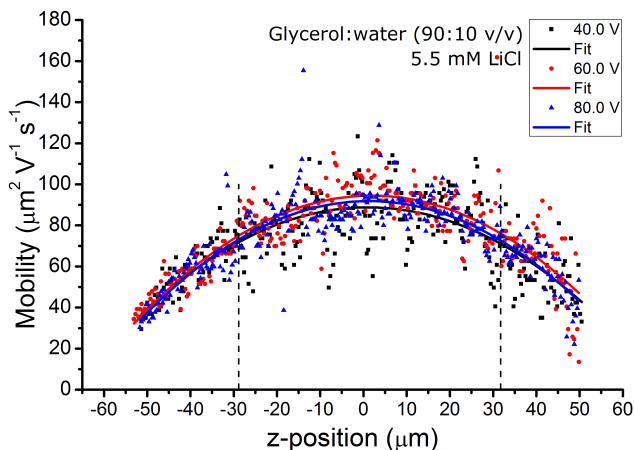


Figure 4.4: Mobility profiles of etched yolk-shell particles at various electric field strength, along with parabolic fits. The dashed lines indicate the stationary planes in the capillary flow. Distance between the electrodes was 19.3 mm.

where  $\mu$  is the mobility ( $\text{m}^2 \text{V}^{-1} \text{s}^{-1}$ ),  $\epsilon_0$  is the permittivity of vacuum,  $\epsilon_m$  is the dielectric constant of the medium, and  $\eta$  is the viscosity of the medium (0.285 Pa s). The dielectric constant of the medium was calculated using the Maxwell Garnett approximation. This yielded a value of 54 mV, which is in good agreement with the zeta potential measurements obtained in water in the Zetasizer. The data for all three electric field strengths show good agreement, as can be seen in Figure 4.4. We attribute the spread of the data points to the error caused by the low volume fraction in the particle tracking.

### 4.3.3 Confocal measurements and particle tracking

In order to study the diffusion behavior of the mobile cores, their locations and trajectories were studied at three different bulk salt concentrations by using a confocal microscope. We assume that ions can pass through the shell, so that the ionic strength inside and outside the shell can equalize. We captured the fluorescence signal of the core particles in one detection channel while simultaneously recording the reflection signal in a second channel. The fluorescence images were used to obtain the core's location with sub-pixel accuracy using particle identification and tracking routine in IDL.<sup>63</sup> Slight and gradual sample drift during the measurement (typically 250 nm over the course of 40 minutes) was corrected using the reflection signal of the particle on the bottom of the capillary. The reflection signal did not significantly depend on the position of the core particle.

Due to the net positive particle charge and the negatively charged capillary wall, the shells stuck to the bottom of the capillary. This caused

Table 4.2: Sample details for confocal studies of yolk-shell particles. Particles were dispersed in glycerol:water (90:10 v/v).

Sample	LiCl (mM)	Conductivity ( $\mu\text{S cm}^{-1}$ )	Debye length $\kappa^{-1}$ (nm)
A	0	0.055	28.4
B	0.55	0.087	22.6
C	5.5	0.468	9.74

the shell to remain immobile while the core was able to move freely inside it. We assumed that the charge on the capillary wall did not influence the electric field inside the shell because the screening length was much shorter than the shell thickness. Over the course of the measurement, the particles bleached significantly. Near the end of the measurement, after 5000 frames, particle intensity had dropped to as low as 28% of the starting intensity. For measurements in the confocal microscope, the particles were dispersed in glycerol:water (90:10 v/v) at three different salt concentrations. Table 4.2 summarizes the sample details. Data from particles that did not meet all of these criteria were discarded. Of the 20 particles that were measured, six passed all the data checks (pixel bias, displacements, and location distribution). In almost all cases where data were discarded, the particle displacements in  $x$  and  $y$  were asymmetric and/or oddly distributed. This was almost certainly in most cases caused by irregularities in the silica shell/confinement. For example, the shell could have been broken or have missing parts, the region doped with silane coupling agent may not have been removed completely, or the core particle may have been trapped in a collection of shell fragments and was thus not in a spherical confinement. The pixel bias, particle displacements, and particle position distribution are shown in Figure 4.5 for one of the six particles that met all the criteria. For the other five particles, the results were qualitatively similar. The histogram of the particle location after the decimal point is not peaked. The histogram of the particle displacements between frames decayed to zero before our cut-off of five pixels. The scatter plot of the particle locations was circular and within the shell inner diameter. Histograms of the  $x$  and  $y$  coordinates separately (shown above and to the right of the scatter plot, respectively) were symmetric.

2D histograms of the particle position are shown in Figure 4.6 for the three different salt concentrations. Without added salt, the particle was confined mostly to the middle of the shell due to the electrostatic repulsion from all sides which only left a small repulsion-free region in the center. As the ionic strength increased, the electrostatic repulsion from the shell wall decreased which allowed the core particle to explore more of the space

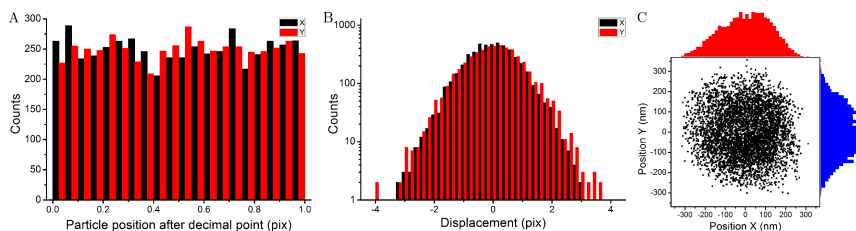


Figure 4.5: **A**: histogram of the pixel values after the decimal point of the particle location, **B**: histogram of particle displacements (60.5 nm/pix), **C**: scatter plot of particle locations. Above and to the right of the scatter plot are histograms of the  $x$  and  $y$  coordinate, respectively.

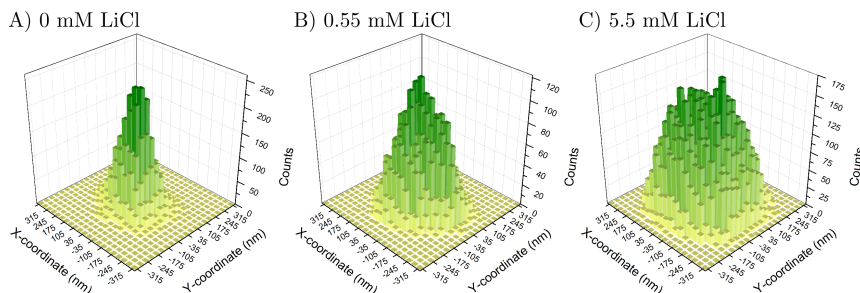


Figure 4.6: 3D representation of the particle position inside the shell for three different bulk salt concentrations. **A**: 0 mM LiCl ( $\kappa^{-1} = 28.4$  nm), **B**: 0.55 mM LiCl ( $\kappa^{-1} = 22.6$  nm), **C**: 5.5 mM LiCl ( $\kappa^{-1} = 9.74$  nm).

inside the shell. The change in the range of the repulsion is surprising, because the difference in Debye screening length is small in comparison. In each of the samples the Debye screening length is short compared to the size of the shell interior. As a result, the core particle will only interact with one side of the shell at a time, getting repelled towards the center.

The mean squared displacement (MSD) of the core particles is plotted in Figure 4.7 along with the MSD of a freely diffusing particle in the middle of the capillary. The MSD of the unconfined particle had a slope very close to one, indicating free diffusion. The diffusion coefficient is in excellent agreement with the value we obtained from the Stokes-Einstein relation. Because the solvent viscosity is very sensitive to slight changes to composition and temperature, the experimental diffusion coefficient is well within experimental error, requiring only a 1% change to either composition or temperature of the medium. Inside the shell, particles moved slower. Short-time diffusion coefficients and the slope of the MSD (evaluated between three and 10 seconds) are summarized in Table 4.3. Short-time self diffusion is the diffusion of a particle on a time scale such that its surroundings barely change. In other words, it is the diffusion of a

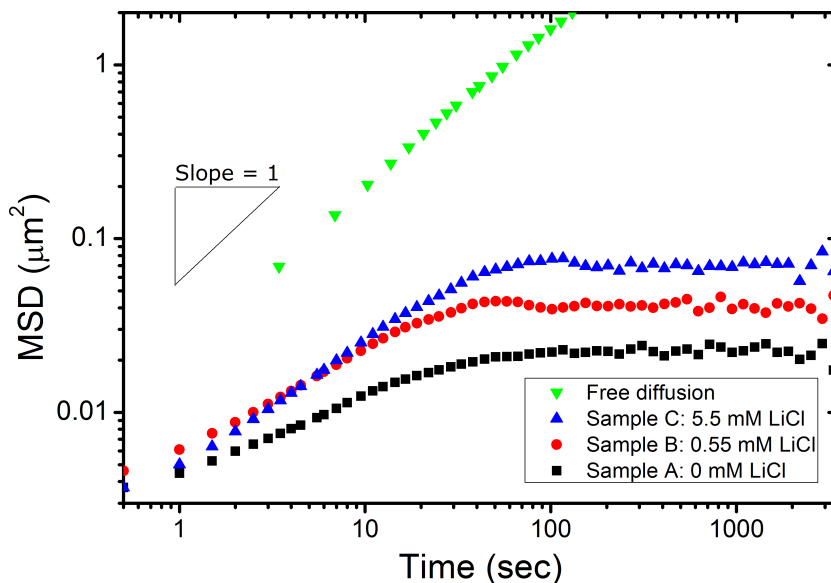


Figure 4.7: Mean squared displacement (MSD) of particles diffusing in the middle of the capillary (at 5.5 mM LiCl,  $\kappa^{-1} = 9.74$  nm) and of confined core particles at three bulk salt concentrations.

Table 4.3: Short-time diffusion coefficient,  $D_s$ , and slope of the MSD (Figure 4.7) for a particle diffusing freely far from walls and for core particles inside shells at various salt concentrations. The time interval for the evaluation of  $D_s$  and the slope of the MSD was between three and 10 seconds.

Sample	Short-time diffusion coefficient, $D_s$ ( $\mu\text{m}^2 \text{s}^{-1}$ )	MSD slope
Unconfined	$3.44 - 3.47 \cdot 10^{-3}$	0.98
Sample A	$0.36 - 0.22 \cdot 10^{-3}$	0.50
Sample B	$0.58 - 0.40 \cdot 10^{-3}$	0.62
Sample C	$0.56 - 0.44 \cdot 10^{-3}$	0.77

particle inside a static cage of other objects with which the particle has hydrodynamic interactions. The short-time self diffusion is dependent on how crowded the surrounding area is, usually by other particles. Therefore, it is often expressed versus volume fraction. We used the method of Mazur et al.<sup>160</sup> to calculate the short-time self diffusion of a particle inside the shell by using the ratio of the core:shell volumes as a volume fraction. This yielded a short-time self diffusion of 85% of the free diffusion. For all confined particles, the MSD slope in the log:log representation was smaller than 1, indicating that the diffusion was not completely free.

We measured the slowest particle diffusion for the dispersion without added salt. As the ionic strength increased, the range of the electrostatic screening decreased which left the core more free space inside the shell. This is reflected by the change in the diffusion coefficients and the MSD slopes. At long times, the MSD of all confined particles leveled off and reached a constant value due to the confinement by the shell. This value increased with ionic strength, as the reduced repulsion from the wall allowed the particle to explore a larger space. In a previous study of a polystyrene particle diffusing in a water droplet,<sup>147</sup> it was found that the droplet-particle size ratio influenced the short-time diffusion coefficient. In their experiments using a size ratio corresponding to that of our yolk-shell particles (2.5),  $D_s$  was reduced to 32% of that in the bulk. Computer simulations also found a reduction to 25-35% for a particle confined between two parallel walls.<sup>132</sup> We found an even greater reduction, which is likely due to the electrostatic repulsion from the shell, especially considering that the shell is porous, which should mitigate some of the hydrodynamic drag.

### Core-wall repulsion

We investigated the interaction between the core particle and the silica shell as a function of ionic strength. Due to their similar charge, there is an electrostatic repulsion between the core and the shell. This repulsion is screened by the ions in the solution; the higher the ionic strength, the shorter the range of the repulsion. Due to this repulsion, the particle potential increases as the distance between the core and the shell becomes smaller. As the potential increases, the probability of finding the particle exponentially decreases.

In order to obtain the probability distribution of the particle position inside the shell, the data needed to be scaled correctly with respect to the volume available to the moving core. The confocal data contained two dimensional information, from which the  $x$  and  $y$  coordinate of the center of the core could be extracted. However, the shell was three dimensional and had a spherical shape. Therefore, the  $x$ - $y$  data were connected to different  $z$ -heights based on their radial position, thus representing different volumes. The height of these sections corresponded to the height of the spherical shell, decreasing as the radius got larger. This yielded a volume for each section of the space inside the shell. The error caused by the pro-

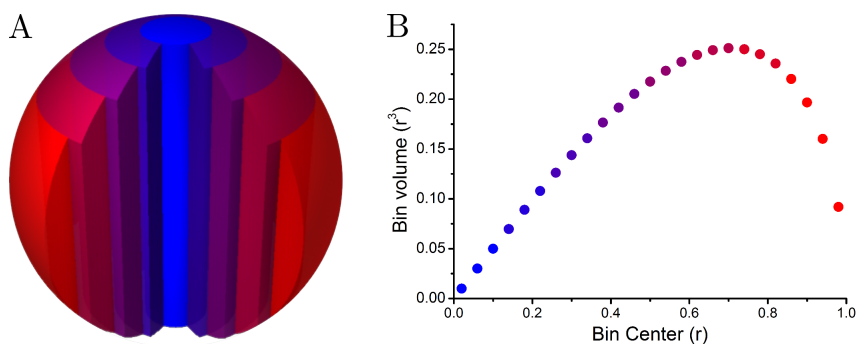


Figure 4.8: Segmentation of a spherical cavity inside the shell into radial bins to compensate for the projection error in the 2D confocal data of the 3D cavity by normalization of volume. **A**: Simplified graphic illustration (only five bins) of the division of the space inside the shell into concentric hollow cylinders of varying height. **B**: The volume of the bins plotted versus bin radius (25 bins).

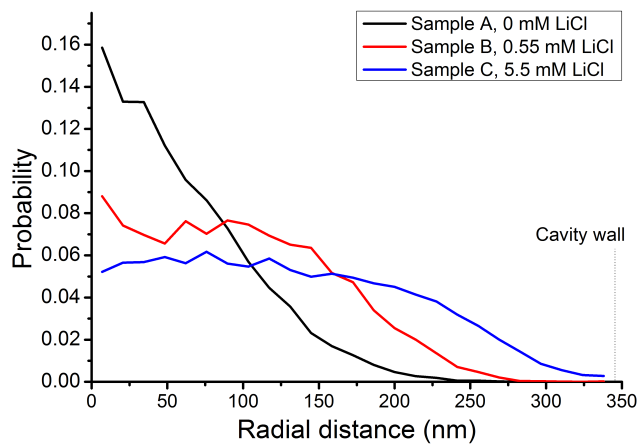


Figure 4.9: Probability of finding a particle as a function of radius from the middle of the shell for three salt concentrations. At low salt concentration, the core is electrostatically confined to the center of the shell. At higher salt concentration, the core particle approaches the shell wall more closely.

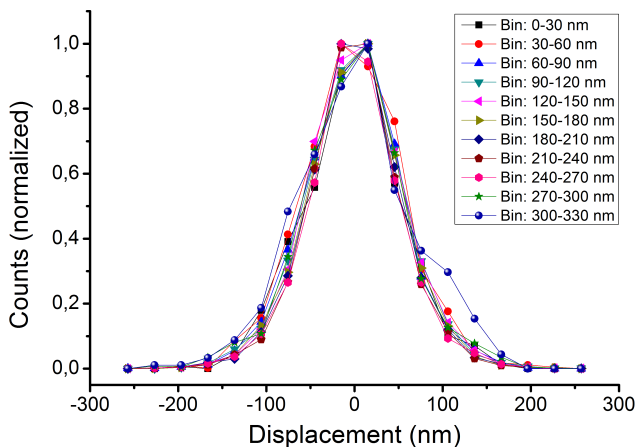


Figure 4.10: Normalized histograms of particle displacements per radial bin. The width of the distribution is determined by the diffusion constant and appeared to be the same in each bin.

jection of the 3D data onto a 2D plane was corrected by dividing the shell into concentric cylindrical sections (bins), as depicted in Figure 4.8A. For simplicity, the sphere in Figure 4.8A is divided into only five segments, we used 25 bins in our analysis. The volumes of all 25 bins are plotted in Figure 4.8B. In this way, the bins in the center of the shell do not truly reflect the core particle's radial distance from the center, because each bin contains a combination of particles close to and far from the wall. However, as the bins move outwards from the center, they contain proportionally more data from particles close to the wall. Therefore, these cylindrical bins should give an indication of separation-dependent behavior.

The average of all particle locations was used as the center of the shell. For each frame, we calculated the distance from the particle to the central axis of the shell, placing it in one of the bins. The number of times a particle was found in each bin was divided by the bin volume to give a probability. The probability of finding the particle as a function of radial distance from the center of the shell is plotted in Figure 4.9 for three salt concentrations. At low salt concentration, the core was confined to the center of the shell, never reaching the wall. As the ionic strength increased, the probability of finding the core closer to the wall increased and close to the center of the shell the probability became more uniform. However, the probability still decreased close to the shell wall ( $\sim 100$  nm) at high ionic strength, indicating that also at 5.5 mM LiCl some electrostatic repulsion remained.

### Diffusion close to the wall

When a particle moves, it must displace the liquid that it is moving through. The flow of the liquid is obstructed close to a barrier, such as a wall. This hydrodynamic resistance slows down the particle when it moves close to a wall. From Figure 4.7 it is clear that particles inside the shells moved more slowly than free particles. Additionally, we investigated the diffusivity as a function of distance from the shell wall. Unfortunately, we did not have access to the full 3D particle position. Instead, we had the 3D position inside the shell projected onto a 2D plane. By dividing the shell interior into concentric radial bins, analogous to the previous section, different behavior close to the wall can be visualized because the bins further from the center contained proportionally more data from particles close to the wall. For this, we used the histogram of the displacements (jumps) of the core particle to measure its diffusion. The width of this histogram is determined by the diffusion constant of the particle. Therefore, if the particle is slowed down, then the histogram should get narrower.

In samples A and B, the core particle remained in the center of the shell for the duration of the measurements. Therefore, we could not investigate the particle diffusivity in close proximity to the wall in these samples. However, in sample C the core particle did come close enough to the wall. As in the previous section, we split the space inside the shell into radial sections. The shell was split into 11 bins in order to retain sufficient statistics in each bin. Histograms of the particle displacements in each bin are plotted in Figure 4.10, normalized to 1. All displacement histograms had the same width, indicating that the diffusion constant was the same, regardless of particle-wall distance. This is surprising, as a large decrease in diffusivity is commonly found.<sup>150</sup> Because the shells we used contain some porosity, it is likely that some liquid flow was possible through the wall. This may have reduced the large increase in hydrodynamic drag close to the wall, thus preventing the drastic reduction in diffusivity. However, the study on a polystyrene particle in a water droplet<sup>147</sup> found that indeed the diffusion in the radial direction became slower as the particle approached the liquid-liquid interface, but that the diffusion parallel to the interface remained constant. Therefore, this may be a feature of the geometry.

## 4.4 Conclusions and outlook

We have investigated the combined effects of electrostatics and hydrodynamics on the diffusion of a confined particle using silica yolk-shell particles. The electrostatic interactions were varied by changing the ionic strength. We found that the diffusion inside the shell was slower than expected when only considering hydrodynamic drag with the shell. We attribute the even lower diffusivity to the electrostatic repulsion from the

shell, which prevented the particle from moving away from the center, effectively creating a potential well. This was reflected in the particle position as well as the slope of the MSD, which was smaller than 1. As the range of the electrostatic repulsion was decreased, the core particle became less confined to the center and the slope of the MSD increased, indicating less restricted, but still not free diffusion. We found that the range of the electrostatic repulsion was larger than expected, especially at low ionic strength. At higher ionic strength, a repulsion-free region developed with a constant particle probability. The diffusivity did not seem to change with particle-wall separation.

Yolk-shell particles with tunable electrostatic interactions between the core particle and the shell provide a convenient system for the study of confined diffusion. The core-cavity ratio and total particle size can be easily changed during the synthesis of the particles. With the use of faster microscopes, the full 3D track of diffusing particles can be obtained, granting more insight into diffusive behavior of particles near walls in confinement. Moreover, cases where the range of the electrostatic repulsion extends beyond the particle diameter may offer other behavior, such as core particles becoming less confined and coupled motion between neighboring particles.

## 4.5 Acknowledgments

The authors wish to thank Henriette Bakker for helping out with the analysis of the microelectrophoresis measurements and Ernest van der Wee for assistance with the tracking code and critical reading of the chapter.

---

# Beam induced dissolution of silica in Liquid Cell Scanning Transmission Electron Microscopy

---

In this chapter we investigate the effect of electron irradiation on silica yolk-shell particles imaged in liquid water using scanning transmission electron microscopy. The particles are fully condensed by heating to 900 °C. The electron beam is found to drastically change the particle, resulting in an increase in the diameter of the core and shell by 10%, followed by gradual shrinkage. Identical particles of a lower density, only heated to 500 °C, demonstrate swelling of only 2-3%. These changes only occur in the scanned area and scale with the electron dose. We hypothesize that these observations are caused by electron beam induced breaking of chemical bonds in the silica matrix. In the presence of water, cleaving of bonds leads to uptake of water through the formation of silanol groups, which causes the increase in particle size. Prolonged irradiation results in further breaking of bonds which in turn leads to loss of material and shrinkage/dissolution of the particle. Surprisingly, the shell retains its shape during these transformations, demonstrating that the silica matrix is capable of internal restructuring to accommodate such plastic deformations. Furthermore, we observe that the particle - the shell in particular - becomes elongated along the scanning direction of the electron beam.

## 5.1 Introduction

Electron microscopy has been an invaluable tool in many scientific fields for decades. The combination of high resolution imaging, diffraction and spectroscopy has made the electron microscope a mainstay from the study of (nano)materials to biomedicine. Unfortunately, electron microscopy studies have always been limited to materials capable of withstanding the high vacuum in the microscope column. In recent years, however, the study of liquid specimens has become a possibility,<sup>25,26</sup> largely due to the development of special windows that are strong enough to withstand the difference in pressure while still allowing the electron beam to pass through virtually unperturbed.<sup>27</sup> Using such a window, it is possible to image the region directly below the window over a liquid reservoir with backscattered electrons in the scanning electron microscope.<sup>161</sup> Moreover, by overlapping two such windows, the electron beam can pass through the sample completely, thus allowing a region of the liquid layer to also be imaged in transmission mode. Additionally, the sample compartment can be heated, electrically biased and can be flushed with liquid during observation. Liquid cell electron microscopy has been used to study nucleation<sup>162</sup> and growth<sup>163,164</sup> of metal nanoparticles, protein distribution in cells,<sup>29</sup> and operation and degradation of Li-ion batteries.<sup>165</sup>

However, there are drawbacks to producing an image using an electron beam. Compared to many forms of optical microscopy, electron microscopy is far more prone to damaging the sample. Common forms of radiation damage include heating, charging, radiolysis/bond breaking and ejection of atoms called ‘knock-on’ damage.<sup>31,166,167</sup> When the sample is in liquid, radiation damage is an even larger problem. In part, this is due to the beam-induced processes that occur in the liquid layer itself, such as the generation of ions, radicals and hydrated electrons, and the effects those have on the material one wishes to study.<sup>32,168</sup> A second complication is the diffusion and dissolution of chemical species in the liquid, resulting in the addition or removal of material. The effect can be so severe that beam effects often completely overshadow the sample’s native behavior, resulting in material transformation, nucleation,<sup>162,169</sup> growth and dissolution of nanoparticles,<sup>32</sup> bubble formation,<sup>30</sup> and the death of cells.<sup>29</sup> Although beam effects may be used favorably to induce certain phenomena, a deep understanding of these effects is crucial for moving in situ liquid cell (scanning) transmission electron microscopy ((S)TEM) to a point where samples may be observed unperturbedly.

In this chapter, we investigated the effects of the electron beam when imaging a sample in liquid water. We chose to study silica, because its chemistry and internal structure are well understood and because silica is commonly used in a wide variety of scientific fields. Moreover, we used particles consisting of a silica sphere inside a silica shell, known as ‘rattlers’ or ‘yolk-shell’ particles. Hollow shells are not commonly studied and their behavior is therefore largely unexplored, whereas solid spheres are

used routinely. The advantage of a combination of spheres and shells is that combined, these particles can display a wide array of effects such as swelling, buckling, cracking, dissolution and deformation over multiple length scales. Additionally, if the shell can form an impenetrable barrier, one could study simultaneously the dynamics of two particles in different media: the sphere in medium one, and the whole particle in medium two.

In order to better understand the properties of the material, we present a brief literature review below. We will first discuss the internal structure of silica particles and the effects of thermal treatment. Next, the effects of electron irradiation on the silica structure are discussed, both when the particles are in a dry state and the available literature of silica particles in water. Although various particle shapes can be synthesized, such as rods<sup>79</sup> and helical fibers,<sup>170</sup> we will only discuss spherical particles prepared using the Stöber method.<sup>16</sup>

### 5.1.1 Silica structure and electron irradiation effects

In order to understand the behavior and properties of silica it is important to know its internal structure. The internal structure of silica is a network of Si-O-Si bonds, called ‘siloxane’ bonds. Although crystalline forms of silica are common, the siloxane network of synthesized silica particles is usually amorphous, even after heating up to 1500 °C.<sup>112</sup> For synthetic silica particles, the siloxane bonds are usually formed from the reaction of two Si-OH groups, called ‘silanol’ groups. During this reaction, called condensation, a water molecule is released. Conversely, siloxane bonds can also be broken in a reverse reaction, called hydrolysis, which consumes a water molecule. The reaction rates of condensation and hydrolysis are pH dependent; both acid and base catalyze the reactions and increase their rates.<sup>17</sup> The thermodynamic equilibrium between hydrolysis and condensation is usually expressed as the solubility of silica. The silica solubility is constant from pH 2 to 9, above which it suddenly increases dramatically.<sup>171</sup>

#### The internal structure of Stöber silica

The particles used in our study were synthesized following the Stöber method,<sup>16</sup> which utilizes ammonia catalyzed hydrolysis of tetraethoxy silicate in ethanol solution. The internal siloxane structure of Stöber silica is not completely condensed, meaning that it is not fully interconnected. As a result, parts of the structure can be removed during the washing procedure, greatly affecting the particle’s porosity.<sup>76</sup> It was also found that directly after synthesis, heating the particles in water to 90 °C for 30 minutes dissolved all of the freshly synthesized silica.<sup>111</sup> However, the siloxane network strengthens over time, particularly the region near the outer surface, becoming able to withstand these etching conditions. Already 14 hours after synthesis, the same etching procedure resulted in hollow shells.<sup>94,111</sup>

Additional heating of the particles to 60 °C in 2-propanol was sufficient to also densify the inner region.<sup>111</sup> Surfactants may facilitate the partial removal of the silica matrix, leading to high porosity. For example, particles that were dispersed in a solution with a surfactant (Lutensol AO5) lost a quarter of their mass, going from six to 31% porosity.<sup>172</sup>

The interconnectivity of the network is usually expressed through the number of siloxane bonds per Si atom, called the Q-value. A Si atom that is only connected to one other Si atom through a bridging oxygen is designated as Q<sup>1</sup>. A Si atom with two siloxane bonds is Q<sup>2</sup>, and so on up to Q<sup>4</sup>. These Q-values can be measured by NMR, and the distribution of Q-values in Stöber silica was found to be approximately 65% Q<sup>4</sup>, 30% Q<sup>3</sup> and a few percent of lower Q-values.<sup>55,110</sup> The density of these particles is usually between 1.8 and 2.0 g/mL, which is below the maximum density of 2.2 g/mL.<sup>24,60,62</sup> These studies demonstrate that the interconnectivity of the Stöber silica matrix is not perfect, even after the initial inherent densification processes. However, the degree of condensation can be improved by high temperature treatment, as will be discussed in the next section.

### The effect of thermal treatment on the structure of Stöber silica

Heating spherical Stöber silica particles caused the internal structure to densify and the crosslinking density to increase. Up to 400 °C, the structure remained predominantly unaffected, and up to 600 °C only minor changes were observed.<sup>112,113</sup> However, above 800 °C, the structure became almost completely condensed. This was most clearly seen in the Q-values. Romeis et al. heated particles to 1000 °C for 12 hours and found that they had converted to 100% Q<sup>4</sup>.<sup>173</sup> In other studies, heating to 900 °C for three hours was sufficient to completely convert the structure to Q<sup>4</sup> and increase the material density to 2.2 g/mL.<sup>174</sup> After the thermal treatment, particles could still be redispersed in ethanol.<sup>174</sup> The restructuring of the silica network is also evident from the loss of porosity,<sup>173</sup> the loss of internal silanol groups,<sup>110</sup> the rise of the Young's modulus,<sup>173</sup> and the decrease in particle volume.

### Electron and ion irradiation of dry Stöber silica

Similar to thermal treatment, electron irradiation leads to a higher particle density and a stronger silica structure. Particles irradiated with a total electron dose of  $5.6 \cdot 10^4$  e/nm<sup>2</sup> decreased in volume by 15-18%.<sup>125</sup> It is important to note that these effects were not caused by electron beam heating. A detailed analysis of the heat generation and conduction as a result of the electron beam found minimal heating ( $10^{-2}$  -  $10^{-3}$  K) for a similar dose rate ( $1.1 \cdot 10^3$  e/nm<sup>2</sup>/s).<sup>175</sup>

The Young's modulus of silica particles was also found to be greatly influenced by exposure to the electron beam.<sup>125</sup> After electron irradiation, silica particles had a higher Young's modulus, close to that of thermally condensed silica. Not only were the particle properties found to have

changed after exposure to the electron beam, they were also found to be different *during* the exposure itself.<sup>125</sup> While irradiated with electron, particles required a smaller force to deform when pressed between a silicon substrate and a diamond anvil than either before or after exposure. The effect was so strong that even particles that had first been hardened by the electron beam were softer than unexposed particles when constantly irradiated. Moreover, deformations induced under electron irradiation were permanent, whereas without the electron beam particles returned to their spherical shape after compression was released. Another study reported a fourfold decrease in contact pressure when the silica particle was deformed while irradiated with the electron beam compared to unirradiated particles.<sup>175</sup> The authors explained this by a constant creation of defects in the silica matrix caused by the electron beam. Initially, the restructuring of the internal structure increased the crosslinking density, leaving a stronger silica matrix. However, when the particle was deformed, these defects allowed for internal rotations and bond switching to occur which facilitated plastic flow.

A different study used a high-energy (MeV) Xe ion beam instead of electrons.<sup>176</sup> This also resulted in local melting of the silica network and deformation of the particle as a whole, which flattened along the beam direction.

### **Electron irradiation of silica particles in liquid**

The presence of water around the silica particles may allow for several other processes to occur while the particle is exposed to the electron beam. Firstly, hydrolysis of siloxane bonds becomes possible due to the presence of water. This is particularly relevant due to the tendency of the electron beam to induce bond breaking and switching in the silica matrix as discussed above. Secondly, molecules such as silicic acid can be dissolved in the water phase and can be transported away from the particle, a process that cannot occur in vacuum. Thirdly, the effect of the electron beam on water itself (and the effects of those radiation products on silica) must be taken into account. In one study, Zecevic et al. speculate that the electron beam produced  $\text{OH}^-$  ions in the water phase, resulting in a rise in pH.<sup>177,178</sup> However, in a later article the same authors postulate the opposite; the electron beam caused the pH to decrease.<sup>179</sup> Calculations involving many radiolysis products have also indicated that the pH becomes lower when exposed to the electron beam.<sup>32</sup> This highlights the complicated and out-of-equilibrium nature of the processes that are caused by the electron beam. On the other hand, the temperature of the sample is not affected by the presence of water. Considering the negligible temperature increase in vacuum (as discussed above) and the fact that surrounding water phase offers greater heat dissipation, it stands to reason that temperature increases in liquid water can be neglected as well.

A recent STEM study of silica nanoparticles in water found that the

nanoparticles gradually dissolved upon prolonged electron beam exposure.<sup>179</sup> Moreover, particles became elongated along the scanning direction of the electron beam, and when the scanning direction was changed, the particles elongated along the new scanning direction. Instead of irradiating already formed silica particles, Van de Put et al.<sup>178</sup> studied a liquid mixture containing the silica precursor tetraethoxy silicate, from which silica particles are routinely synthesized. Upon irradiating the solution with electrons, silica was rapidly precipitated out of the solution. The reaction was found to be fast and local enough that silica formed where the electron beam was scanned, allowing the authors to effectively write with the beam. These studies make it clear that also in liquid water, electron irradiation can alter the internal structure of the silica network, causing particles to change shape and dissolve, and that also dissolved silicates are affected by the electron beam.

## 5.2 Experimental

### 5.2.1 Particle synthesis

The full synthesis procedure is available in Ref. [136]. In brief, the silica core was made by Stöber synthesis.<sup>16</sup> Subsequently, a polystyrene layer was grown around the silica core followed by an outer silica shell. The sacrificial polystyrene layer was burned away by pyrolysis at 500 °C for four hours in air to yield yolk-shell particles. Finally, a high temperature treatment converted the particles to pure SiO<sub>2</sub>. For this, particles were heated to 900 °C (5 °C/min). This temperature was maintained for three hours, after which the sample was allowed to cool down to room temperature overnight. Deionized water used to disperse the particles and to flow through the liquid cell was obtained from a Millipore Direct-Q3 UV purification system.

### 5.2.2 TEM liquid cell assembly

The sample was prepared using a liquid cell holder (Hummingbird Scientific, USA) and two standard silicon chips with a SiN layer, each containing a SiN window of 200x50  $\mu\text{m}$ , with a thickness of 50 nm. One of the chips had a 500 nm spacer layer to prevent the windows from coming in direct contact and to create a channel for liquid flow. Before use, both chips were glow discharged for 15 seconds to make them hydrophilic. A 1.0  $\mu\text{L}$  droplet of particle dispersion was placed on one of the chips and allowed to dry. Subsequently, a 1.0  $\mu\text{L}$  droplet of deionized water was added on top of the sample and the other chip was placed over the top, with the windows parallel. The chip stack was placed inside the holder tip which was then closed and tested for leaks.

### 5.2.3 STEM measurements

STEM measurements were performed on a Tecnai 20 electron microscope (FEI company, USA) equipped with a field emission source, operating at 200 kV. In order to prevent premature accumulation of electron dose, the electron microscope was aligned using a regular copper grid before inserting the liquid cell holder. Searching for suitable particles was performed at low magnification, typically with a scanning window of  $8.95 \times 8.95 \mu\text{m}$ . Once a particle was found, it was centered in view and the electron beam switched off (blanked). For each experiment, an overview image (frame one) was recorded of a particle and its surroundings, followed by a prolonged exposure at higher magnification (frame two through frame (N-1)), and finally another overview image (frame N). Overview images were  $1024 \times 1024$  pixels, had a viewing area of  $4.51 \times 4.51 \mu\text{m}$  with a pixel dwell time of  $8.00 \mu\text{s}$  and a total acquisition time of  $10.0 \text{ s/frame}$ . For the prolonged recording, we used  $512 \times 512$  pixels, a viewing area of  $1.16 \times 1.16 \mu\text{m}$  with a pixel dwell time of  $4.00 \mu\text{s}$  and a total acquisition time of  $1.26 \text{ s/frame}$ . When needed, focusing of the STEM probe was performed on a nearby object. After the measurement, the movies were drift corrected using a custom-made macro in ImageJ, and a two pixel Gaussian blur was applied over the images to reduce noise. The dose rate was calculated by dividing the beam current by the scanning area, while the holder was moved out of the beam path.

## 5.3 Results and discussion

In order to investigate the effect of a scanning electron probe on silica yolk-shell particles we analyzed the size of the core and the shell as a function of total accumulated electron dose. Particles were dispersed in water and imaged using Scanning Transmission Electron Microscopy (STEM). Additionally, we studied the dependence on the dose rate and performed experiments both with and without liquid flow. Finally, we varied the scanning direction of the STEM probe. The experimental details for each measurement are summarized in Table 5.1. For each measurement, a new particle was chosen that had not previously been exposed to the electron beam. In all STEM images, the scanning direction was left to right, starting in the top left corner, unless stated otherwise.

### 5.3.1 Electron beam induced changes to particle size of silica shells and enclosed spheres

Yolk-shell particles were heated in an oven after synthesis to fully densify the silica to  $900 \text{ }^\circ\text{C}$  for three hours. Subsequently, they were redispersed in water and imaged in STEM mode using a liquid cell holder. The particles were imaged and exposed to the electron beam continuously. Therefore, the total electron dose increased proportionally with the duration of the

Table 5.1: Measurement details and conditions of the particles that were recorded in the liquid cell. Particles were dispersed in deionized water after having been heated to 900 °C for three hours in air.

Particle	Flow rate ( $\mu\text{L}/\text{min}$ )	Dose rate ( $\text{e}/\text{nm}^2/\text{s}$ )	Fr. time (s)	#frames	Figure
1	0.0	$1.6 \cdot 10^3$	1.26	1997	
2	0.0	$6.4 \cdot 10^3$	1.26	1998	5.6 & 5.7
3	2.5	$6.4 \cdot 10^3$	1.26	1998	5.6 & 5.7
4	5.0	$4.4 \cdot 10^2$	1.26	1998	
5	5.0	$3.2 \cdot 10^3$	1.26	960	
6	5.0	$6.4 \cdot 10^3$	1.26	998	5.4 & 5.7
7	5.0	$6.4 \cdot 10^3$	1.26	1998	5.1, 5.2 & 5.7, movie S1
8	5.0	$6.9 \cdot 10^3$	0.50	996	
9*	5.0	$2.5 \cdot 10^4$	1.26	698	5.3 movie S2
10**	5.0	$2.5 \cdot 10^4$	1.26	876	5.8 movie S3

\* = Broken shell

\*\* = Rotated scanning direction

imaging. Images from a typical movie are shown in Figure 5.1 (particle 7). Figure 5.1A shows the whole particle, and a close-up of the core is shown in Figure 5.1B. The total accumulated dose is stated above each image and is not necessarily the same between Figure 5.1A and B. This value represents the total electron dose for the whole frame, not only for the particle.

Upon exposure to the electron beam, the shells were first seen to increase in diameter, reaching a maximum of 110% of the original diameter. After this initial expansion, further electron beam exposure led to shells continually decreasing in size, down to 40% of the original diameter and closely surrounding the core particle. During this rather severe expansion and contraction, the shell remained more-or-less spherical. The diameter of the shell was measured throughout the exposure and is plotted in Figure 5.2. The dark green highlighted data points correspond to the images presented in Figure 5.1A.

The core particle inside the shell exhibited similar behavior as the shell, albeit slower and less extensive. Initially, it increased to approximately

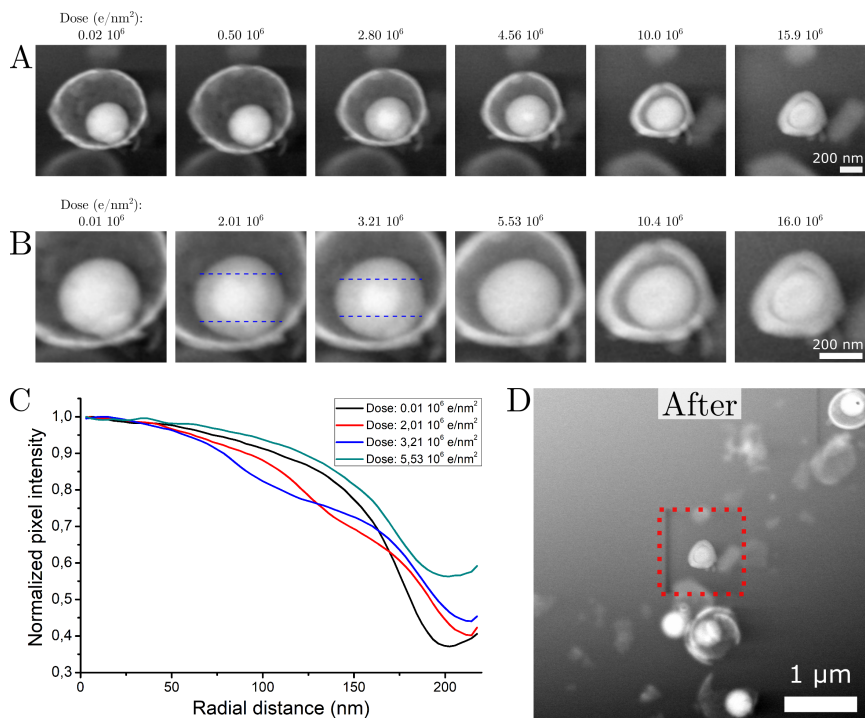


Figure 5.1: **A:** STEM images of yolk-shell particle 7 under electron irradiation (dose rate:  $6.4 \cdot 10^3$   $e/nm^2/s$ , water flow:  $5.0 \mu L/min$ , scalebar is 200 nm). **B:** Close-up images of the core particle from the same measurement (scalebar is 200 nm). The blue dashed lines demarcate the inner region of higher contrast. **C:** The radially averaged pixel intensity (normalized to 1) of the core particle from the center to the rim at several stages during exposure. As the core was irradiated by the electron beam, a high-contrast center became distinct from a darker rim, as evidenced by the shoulder in the pixel intensity plot. **D:** Overview image after the measurement showing the particle, the scanned area (red), and the surrounding area (scalebar is 1  $\mu m$ ). Outside the irradiated area, no changes were observed.

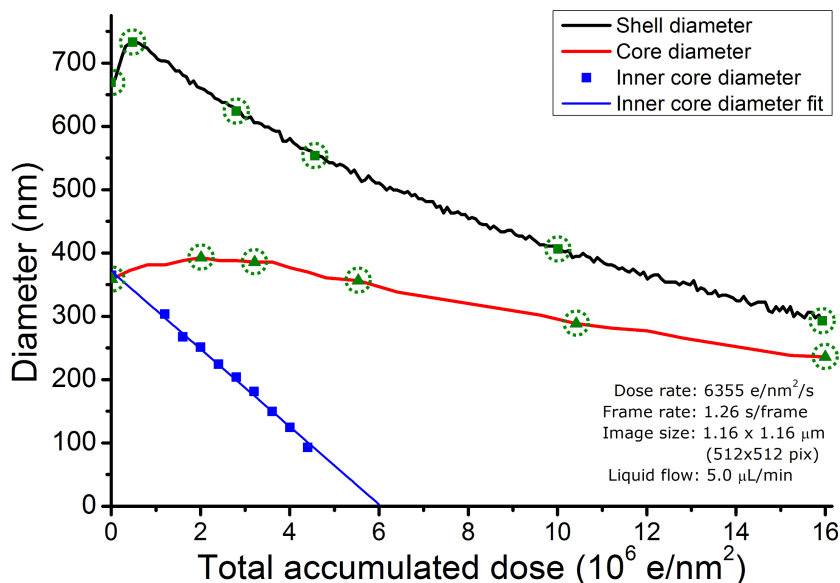


Figure 5.2: Evolution of the shell and core size under electron irradiation for particle 7 (dose rate:  $6.4 \cdot 10^3 \text{ e/nm}^2/\text{s}$ , water flow:  $5.0 \mu\text{L}/\text{min}$ , see movie S1 in Supporting Information). The diameter of the shell and the core were measured orthogonal to the scanning direction. The highlighted dark green data points correspond to the images in Figure 5.1.

110% of its original size, followed by gradual shrinkage. The diameter of the core is also plotted in Figure 5.2 (images of Figure 5.1 are highlighted as dark green points). Inside the core particle, a brighter inner region became distinct from a darker rim as the recording proceeded. This bright region is demarcated by blue dashed lines in Figure 5.1B. The development of this bright core/dark rim is visualized in Figure 5.1C, where the radially averaged pixel intensity from the center of the core to the edge is plotted. At the start of the recording, the intensity decreased smoothly from the center to the edge. As the electron dose increased, a drop in intensity developed, corresponding to the transition from the bright core to the darker outer region. The radial position of this drop-off moved closer to the particle center as the electron dose increased. Eventually, the bright region completely disappeared and the radially averaged contrast decreased smoothly again. The diameter of this bright inner core region is also plotted in Figure 5.2, along with a linear fit. The changes to the core particle radius can be observed in the shift of the minima of the radial intensity plots in Figure 5.1C as well.

Figure 5.1D shows an overview image, taken at lower magnification, of the particle after the recording. The scanned area with the particle is indicated by a dashed red square in the center. A darker region on the left

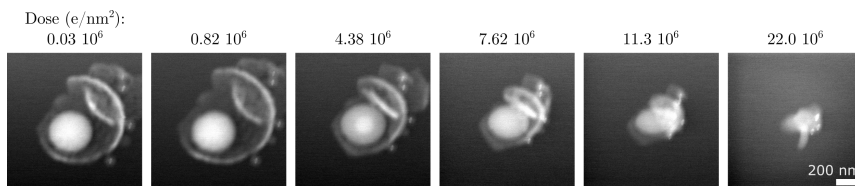


Figure 5.3: STEM images of particle 9, which had a broken shell (dose rate:  $2.5 \cdot 10^4 e/nm^2/s$ , water flow:  $5.0 \mu L/min$ , see movie S2 in Supporting Information). Similar to particles with intact shells, expansion and contraction of the shell and of the core were visible. Also, the core exhibited a brighter and darker region which moved inwards. Scalebar is 200 nm.

of the scanned area is a scanning artifact. After a line is scanned, the beam is returned to the start (left) of the line below it where it is parked briefly before scanning is resumed, causing this area to accumulate a slightly higher exposure compared to the rest of the image. The product of the pixel dwell time and the number of pixels equaled 1.05 seconds, while the total frame time was 1.26 seconds. The overview image shows that only the area irradiated by the electron beam was affected, because the particles just out of frame remained unchanged. It is therefore unlikely that the silica dissolution was only caused by a pH change in the surrounding water and that energy input by the electron beam into the particle material was required as well.

We observed roughly the same morphological changes as described above for a particle with a broken shell. Figure 5.3 shows images of a broken shell with a core particle inside during electron irradiation. Even though a large section of the shell was missing, it exhibited a similar expansion and shrinkage of the silica shell and a gradual change in contrast of the core particle. The occurrence of the same changes to the core and shell for both intact and broken shells demonstrates that these changes did not depend on the interior being separated or closed off as a result of a build up of stress in the shell, nor did it require the interior to be different from the surrounding medium, such as a build-up of pressure or high concentrations of dissolved chemical species inside the shell relative to outside. We conclude from these observations that the expansion, shrinkage, and changes in contrast were related to more local properties of the silica, not the particle geometry per se.

The observations described above can be explained by a combination of three processes: electron beam induced chemical bond breaking in the silica matrix, which is known to occur in vacuum,<sup>175</sup> reaction of broken bonds with water to produce stable silanol groups, a reaction that is well established in silica chemistry,<sup>17</sup> and an electron irradiation induced reduction in yield stress allowing for plastic deformation, which is also known

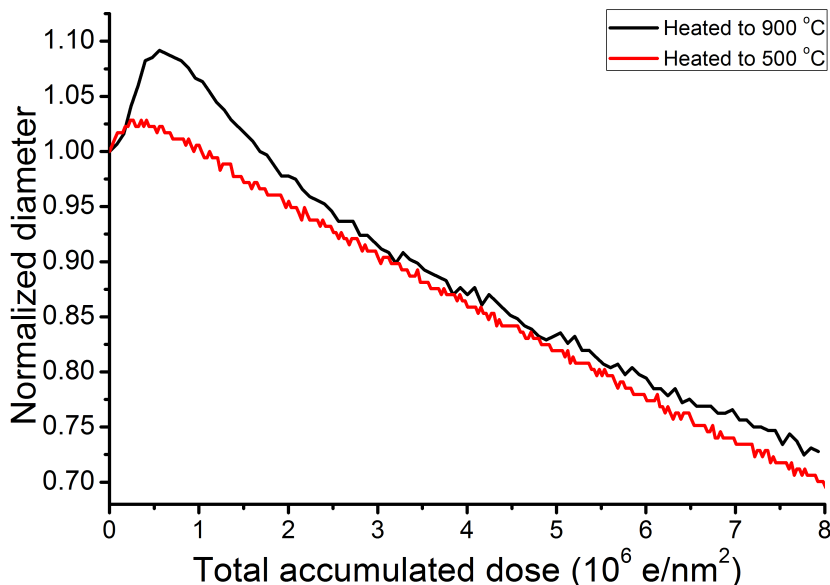


Figure 5.4: Silica shell diameter as a function of dose rate for a completely condensed particle (heated to 900 °C for three hours, particle 6), and a partially condensed particle (only heated to 500 °C for four hours). Liquid flow was 5.0  $\mu\text{l}/\text{min}$  during both measurements.

to occur in vacuum.<sup>125</sup> The presence of water is crucial, because electron irradiation in the absence of water results in opposite behavior, as described in the introduction. We hypothesize that the increase in particle size was caused by a decrease in density as a result of the uptake of water by broken siloxane bonds and that the later shrinkage of the particle was the result of further bond breaking which led to loss of material. At the same time, the continuous bond breaking caused by the electron beam allowed the material to restructure, resulting in high plasticity and allowing the shell to maintain its spherical shape. The siloxane bonds may have been broken directly by the electron beam through radiolysis, and/or by e-beam generated reactive species in the water/particle interior, such as ions and radicals. In either case, when a siloxane bond is broken it consumes a water molecule to produce two silanol groups. The incorporation of water added material/mass to the silica matrix while at the same time decreased its crosslinking density, explaining the initial expansion. Both of these effects led to swelling of the structure and a reduction in density which in turn resulted in the expansion of the particle, most notably the shell. Figure 5.4 shows the shell diameters of a particle heated to 900 °C for three hours and a particle only heated to 500 °C for four hours. Thermal treatment at 500 °C is not enough to fully condense the silica matrix. Indeed, the initial increase in shell diameter was much smaller (2-3% com-

pared to 9.2%) for the partially condensed particle, strongly corroborating our hypothesis that the expansion is caused by a decrease in density.

The reduction in density likely also caused the appearance of a bright inner core region. The contrast generation in these STEM measurements is mainly due to mass contrast, because the sample was amorphous and homogeneously composed of the same elements. Therefore, pixel intensity was determined by sample thickness and density. Initially, the silica structure was completely condensed, owing to the high temperature treatment in a furnace preceding the experiment. Due to the electron beam, siloxane bonds on the surface of the core particle were broken allowing water to penetrate deeper into the particle and cleave bonds there. We hypothesize that the reaction front on the border between a high density (bright) core and a lower density (darker) rim moved inwards with increasing electron dose until all the high density silica was converted to a lower density with fewer siloxane bonds. As the electron dose increased further, more of the siloxane bonds were broken until at a certain point silicon atoms or silicate oligomers were completely disconnected from the silica matrix and went into solution. Due to this loss of material and the high plasticity caused by the weak cross-linking (see section 5.1.1), the particle size decreased which resulted in shrinkage of the core and shell. It is very likely that during this out-of-equilibrium situation - with a lot of dissolved silica present in the water - the reverse process (deposition of silica onto the shell particles and the SiN window) was also taking place.<sup>178</sup>

From the rate at which the edge of the bright inner core region moved inwards, we can calculate how much electron dose was required to convert one nanometer of silica from high density to lower density. This yielded a value of  $3.0 \cdot 10^4$  e/nm<sup>2</sup>, where we have taken into account that the reaction occurred from both sides of the particle. In a similar way, we calculated the dose required to convert one nanometer of silica in the shell. The shell had a thickness of 42 nm and it reached its maximum diameter at a total accumulated dose of  $5.6 \cdot 10^5$  e/nm<sup>2</sup>, which is where we assume all high density silica has been converted. This gives a value of  $2.7 \cdot 10^4$  e/nm<sup>2</sup> to convert one nanometer in the shell (the reaction can occur from two sides). The good agreement between these values suggests that the underlying process was likely of the same nature.

### 5.3.2 Effect of dose rate

The experiment described in the previous section was repeated with a range of dose rates spanning two orders of magnitude, from  $10^2$  to  $10^4$  e/nm<sup>2</sup>/s. For comparison, Van de Put et al.<sup>178</sup> used a dose rate of  $10^0$  to  $10^1$  e/nm<sup>2</sup>/s, and Zecevic et al.<sup>179</sup> used  $10^3$  e/nm<sup>2</sup>/s. For each measurement, a new particle was chosen that had not previously been exposed to electron irradiation. Experimental conditions of all the measurements can be found in Table 5.1. The diameter of the silica shells was measured orthogonal to the scanning direction for all particles and is plotted in Fig-

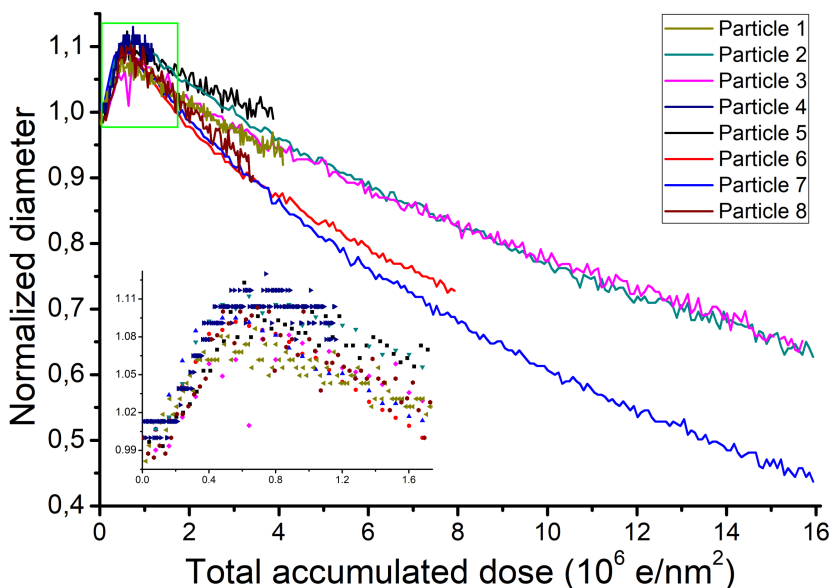


Figure 5.5: Plot of the normalized shell diameter of particles exposed to the electron beam at various dose rates (see Table 5.1 for experimental details). The expansion and contraction of the shell occur at the same total electron dose despite the difference in dose rate. The inset shows a close-up of the maximum in the shell diameter (highlighted in green). The colors of the scatter plot match those of the large graph.

ure 5.5 versus the total accumulated electron dose. In each experiment, the shell expanded by approximately 10%. Additionally, the total dose at which the shell reached its maximum diameter was similar, regardless of dose rate and liquid flow rate. The occurrence of the same behavior in all these experiments demonstrates that they were caused by the electron beam and scale proportionally with the total dose. Although we are unable to determine to what extent, it is likely that the changes to the silica were caused by a combination of direct electron beam (knock-on damage) effects and by radiolysis products. Moreover, it is as of yet unclear whether the electron beam increases or decreases the pH.

The shrinkage of the shells exhibited some spread, with particles 6 and 7 shrinking more rapidly than 2 and 3, for example. We expect that these were caused by variations in shell thickness and experimental conditions such as the thickness of the water layer.

### 5.3.3 Effect of flow rate

We investigated the influence of water flow by performing a measurement with and without flowing water through the TEM holder. Apart from

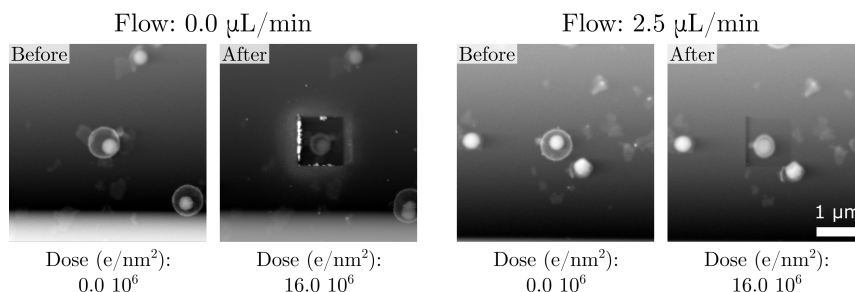


Figure 5.6: Zoomed-out STEM images of particles before and after exposure to the electron beam without and with liquid flow (particle 2 (left) and 3 (right), dose rate  $6.4 \cdot 10^3 \text{ e/nm}^2/\text{s}$ ). Without liquid flow, the surroundings of the viewing area became coated with material. However, with a flow rate of  $2.5 \mu\text{L}/\text{min}$ , almost no deposition of material was observed. Scalebar is  $1 \mu\text{m}$ .

the liquid flow rate, the measurement conditions were identical. Overview images were recorded before and after prolonged exposure to the electron beam, showing the irradiated area, including the particle, and its surrounding region. These images are shown in Figure 5.6 for a measurement performed without liquid flow and one with a liquid flow rate of  $2.5 \mu\text{L}/\text{min}$ . After adjusting/stopping the flow rate, the system was allowed to dissipate residual flow for at least 60 seconds before a measurement was started

In both experiments, only the particle within the scanned region was affected by the electron beam. In the absence of liquid flow, the region around the scanned area became coated with material and small clusters, similar to the study on a mixture of water and silica precursor.<sup>178</sup> Once outside the irradiated area, this material precipitated and deposited on the window, demonstrating that silica was removed from the particle, went into solution, and aggregated/resolidified once no longer exposed to the electron beam. In the experiments with liquid flow, no residual coated material was present around the irradiated region, indicating that this material was carried away by the liquid. These experiments show that silica was dissolved when exposed to electron beam, and that it reformed once no longer irradiated. It is therefore likely that redeposition of silica is occurring continuously during the electron irradiation. In fact, the redeposition and/or local restructuring is the only mechanism by which the shell could so significantly shrink in diameter while still holding its spherical shape around the core particle.

### 5.3.4 Particle elongation in the scanning direction

The particles were imaged using STEM. This is a scanning technique, meaning that the image is built up pixel by pixel. Typically, lines are

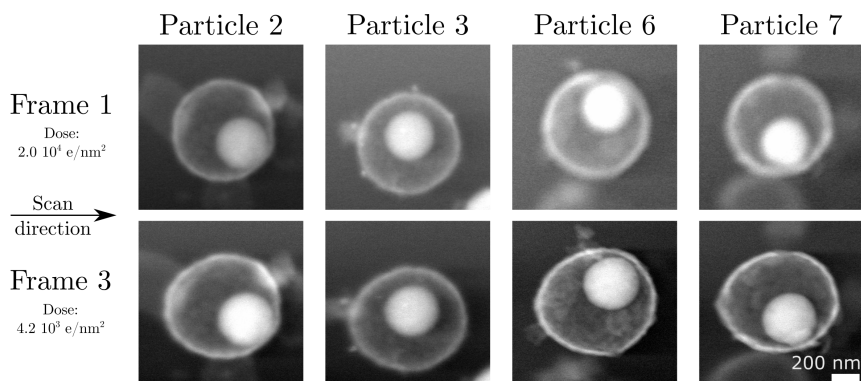


Figure 5.7: The first and third STEM images of particles 2, 3, 6, and 7 in water (see Table 5.1 for experimental details). The first frame was recorded at higher resolution but at lower magnification: 1024x1024 pixels, 4.51x4.51  $\mu\text{m}$ , 10.0 s/frame, 8.00  $\mu\text{s}$  pixel dwell time. Subsequent images were recorded with only the particle in view: 512x512 pixels, 1.16x1.16  $\mu\text{m}$ , 1.26 s/frame, 4.00  $\mu\text{s}$  pixel dwell time. Initially, the particles were all spherical. However, in the third frame, the shells had deformed and stretched slightly along the scanning direction to an aspect ratio of 1.13. The diameter of the shell in the  $y$ -direction remained unchanged. Scalebar is 200 nm.

scanned horizontally from left to right, starting from the top left corner. In doing so, the horizontal and vertical direction in the image become intrinsically different.

When recording the particles in STEM, we observed that the particles were initially spherical, but became stretched along the scanning direction already after two frames. Along the direction orthogonal to the scanning direction, the particle size remained unchanged. This is depicted in Figure 5.7, where the first and third recorded frames are shown (see Experimental section for imaging conditions). In the first frame, shown at the top, the cores and shells appeared spherical, measuring the same diameter vertically and horizontally. However, in the third frame the cores and shells had become stretched along the horizontal direction, parallel to the scanning direction of the STEM probe. This phenomenon was observed for many particles.

Another experiment was performed to further investigate the effect of the scanning direction. In this experiment, the electron beam was used to convert a spherical particle into a much more anisotropic particle; by initially only partially irradiating the core-shell particle, a strong anisotropy in the shape was created that was subsequently strongly enhanced. The results are shown from left to right in the top part of Figure 5.8 (A-E). The total electron dose is stated in each image, and the arrow indicates the scanning direction. A yolk-shell particle (particle 10) was placed on

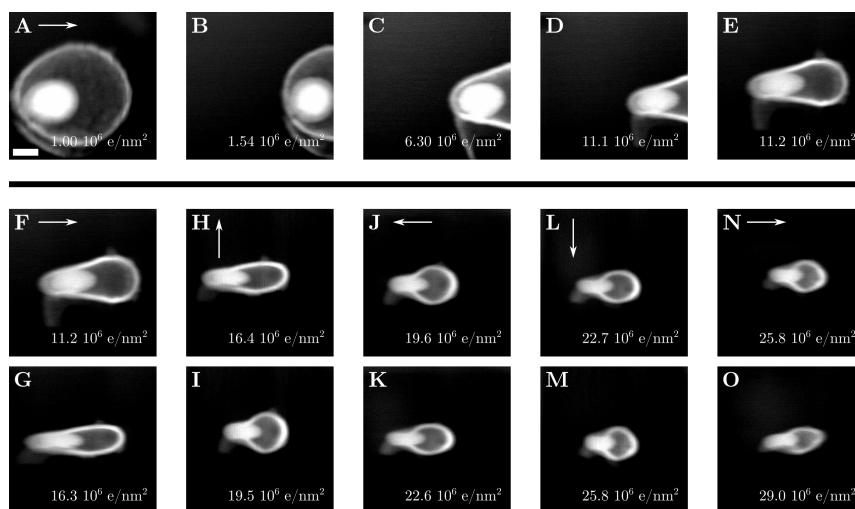


Figure 5.8: STEM images of particle 10 (see movie S3 in Supporting Information). The top part shows the formation of an elongated particle by irradiating only half of a yolk-shell particle to a total dose of  $11.2 \cdot 10^6 \text{ e/nm}^2$  (A-E). The arrow indicates the scanning direction of the electron beam. The bottom part (F-O) displays the influence of the scanning direction. The particle shown in F was exposed to the electron beam, which resulted in stretching of the particle along the scanning direction, shown in G. Then, the scanning direction was rotated by  $90^\circ$  (H) and the exposure was continued. Again, the particle was stretched along the scanning direction, as can be seen from image I. This process repeated for each scanning direction completing a full rotation. The total accumulated dose is shown in each of the images. Scalebar is 200 nm.

the edge of the viewing area and its left half was irradiated by the electron beam, causing it to contract, predominantly in the vertical direction. This resulted in an elongated particle.

The anisotropic particle was then placed in the center of the viewing area and exposed to the electron beam while periodically rotating the scanning direction by  $90^\circ$ . The bottom part of Figure 5.8 (F-O) shows the first (top) and last (bottom) frames of these series of prolonged exposures. Scan direction and total electron doses are shown with the images. In each exposure, the particle was stretched along the scan direction. The aspect ratio of the particle is plotted in Figure 5.9, and can be seen to oscillate as it is stretched along different directions.

Elongation of silica particles in liquid cell STEM has been reported before by Zecevic et al.<sup>179</sup> However, there are some important differences between their study and this one. First, the morphology of the particles: they used small spheres of 53 nm, whereas we used a core-shell particle with an outer diameter of 770 nm. Second, the particles in the previous

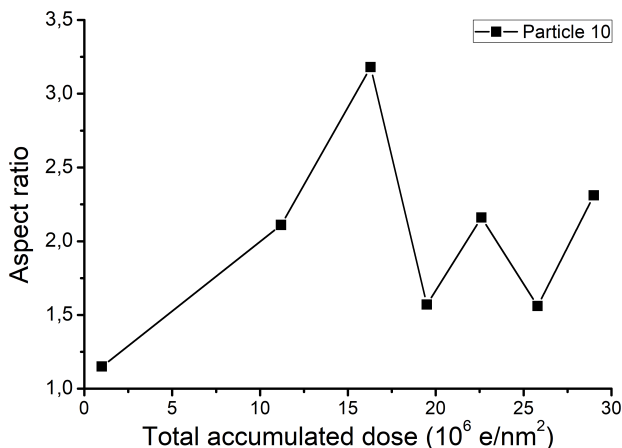


Figure 5.9: Aspect ratio of particle 10, shown in Figure 5.8 (see movie S3 in Supporting Information). Initially, only half of the particle was irradiated (up to  $11.2 \times 10^6$  e/nm<sup>2</sup>), after which the particle was centered in view. The scanning direction was rotated by  $90^\circ$ , causing resulting in stretching of the particle, reflected in the aspect ratio.

study were only heated to  $600^\circ\text{C}$  instead of  $900^\circ\text{C}$  (in both cases, for three hours). Third, the pixel dwell time in their measurements ( $20\ \mu\text{s}$ ) was five times higher than in our study.

Zecevic et al. reported deformation occurring from a total dose of  $3.5 \times 10^5$  e/nm<sup>2</sup>, whereas in the present work this was observed from an order of magnitude lower total dose. The authors explained the elongation by a silica dissolution-precipitation process, whereby more material was released from the middle of the particle than from its edges (top and bottom). The additional material in the middle region around the particle then solidified and extended the middle outwards to the sides (left and right). Although dissolution and precipitation of silica were certainly occurring (see Figure 5.6), it does not explain the rapid particle deformation on the scale we found in our experiments. The elongation of the shell, seen in Figure 5.8, occurred faster and covered more distance than in the case of the small nanoparticles of Zecevic et al. Alternatively, the elongation of the particle along the scanning direction could have been caused by plastic material deformation, a process that is known to be enhanced by electron irradiation.<sup>110,125,173,175</sup> The gradual shrinking of the spherical shell while it retained its shape demonstrates that the material was capable of large plastic deformation and/or restructuring. However, even if the change in particle shape was caused by plastic deformation instead of beam induced dissolution-precipitation of silica, it does not explain why this deformation would occur along the scanning direction. It may be connected to a trail of silica with high plasticity that follows the scanning

electron beam, allowing internal stresses to relax more easily along this direction. This is consistent with the higher dose required by Zecevic et al. to elongate the particles as they used a slower scan speed, effectively shortening the high plasticity trail. Alternatively, it may be related to a beam induced (electric) field or concentration gradient(s). Changing the scan speed and monitoring the particle elongation will provide more insight into the underlying mechanism.

## 5.4 Conclusions and outlook

We have studied the effects of electron irradiation on fully condensed (heated to 900 °C) silica yolk-shell particles in water. Upon electron irradiation, the core particles and shells initially increased in size followed by steady shrinkage, most noticeable for the shells. The maximum increase in diameter - for both core and shell - was 10%. This is in striking contrast to unheated silica particles irradiated in vacuum, which shrunk by 10%.<sup>110</sup> Particles of a lower density (heated to 500 °C) only expanded by 2-3%, indicating that the expansion of the shell was related to a decrease in density. Additionally, upon electron beam exposure, a bright region became distinct in the center of the core particle. The border between the brighter core and the lower-contrast rim moved inward at a constant rate. Identical behavior was observed for a particle with a broken shell, indicating that the observations were not dependent on a difference between the particle interior and exterior. We found that these phenomena were caused by the electron beam and that they scaled with total accumulated electron dose and were independent of dose rate. This is further supported by the fact that material transformation was only observed in the field of view. Moreover, particles just outside the field of view remained unaffected, indicating that reactive species created in the water were not solely responsible for the transformations and that direct exposure to beam was essential. The calculated dose dependency for the conversion of one nanometer of the core and shell were similar,  $3.0 \cdot 10^4$  and  $2.7 \cdot 10^4$  e/nm<sup>2</sup>, respectively, suggesting that these underlying processes were likely of the same nature. We attribute these phenomena to electron beam induced chemical bond breaking in the silica matrix, which is known to occur in vacuum.<sup>175</sup> In the presence of water, these broken bonds were stabilized by forming silanol groups, incorporating water into the structure and swelling the material. Due to the continuous breaking and reforming of chemical bonds, the material was capable of internal restructuring, resulting in high plasticity and allowing the shell to maintain its spherical shape instead of fracturing, which is also known to occur in vacuum.<sup>125</sup> Prolonged irradiation resulted in silicate monomers/oligomers becoming completely detached from the network, causing the particle size to decrease.

In addition to these findings, we also observed elongation of the particle

along the scanning direction of the electron beam. Even at low electron dose, the average aspect ratio of spherical particles increased from 1.03 to 1.13 between the first and third frame (total dose  $1.7 \cdot 10^4$  e/nm<sup>2</sup>/s). The effect was more pronounced for an anisotropic particle. Rotation of the scanning direction resulted in large changes in the aspect ratio of the anisotropic particle, always stretching along the scanning direction. Although we can explain the changes in particle size and contrast based on processes that are known to occur in silica under electron irradiation, elucidating the underlying mechanism of the particle elongation along the scanning direction requires further experiments and modeling.

In future experiments, we plan to repeat the same measurements with shells that do not contain a core particle to investigate to what extent silica from the core particle deposits on the inside of the shell. Additionally, by illuminating only the water around the particle - but not the particle itself - it would be possible to determine to what extent the transformation of the silica is caused directly by the electron beam or indirectly by radiolysis products of water, such as a change in pH. Moreover, directly measuring the change in pH as a function of dose rate would be very valuable to the entire liquid cell community and would supplement and corroborate the calculations performed by Schneider et al.<sup>32</sup> The elongation of the particles along the scanning direction may be dependent on the interplay between the timescale of the image acquisition (scan speed) and the kinetics of the system, such as reaction rates, diffusivities, and stress relaxations. However, it is unclear how these timescales influence each other and how they affect particle elongation. This can be achieved by simultaneously modifying the frame acquisition time and the dose rate to maintain a constant frame dose, thereby changing the ratio between the imposed dynamic changes (such as electric fields or concentration gradients caused by the scanning electron beam) and inherent system dynamics.

The study of electron beam induced phenomena can be of great use in understanding physical and chemical processes. However, of even greater value is the ability to observe (liquid) samples in the electron microscope without immensely altering their behavior and instead studying their native dynamics, facilitating comparison with *ex situ* experiments. In this effort, understanding of electron beam effects is crucial. One sure way of approaching this goal is through a reduction in the required electron dose. More sensitive and faster cameras, such as direct electron detection cameras, are a big step in this direction. A recent TEM liquid cell study of the diffusion of gold nanoparticles reported an acquisition rate of 100 frames per second.<sup>180</sup> Additionally, the importance of measuring effects as a function of dose rate can not be overstated. If low-dose and high-speed imaging becomes available, one could use these yolk-shell particles as *in situ* probes of the local temperature and viscosity by measuring the diffusion of the core particle.

## 5.5 Acknowledgments

The authors wish to thank Sina Sadighikia additional liquid cell measurements and Kanako Watanabe and Daisuke Nagao for the silica yolk-shell particles. Jovana Zecevic, Krijn de Jong and Niels de Jonge are thanked for useful discussions. We thank Wiebke Albrecht for critical reading of the chapter. Chris Schneijdenberg and Hans Meeldijk are gratefully acknowledged for assistance with the electron microscope.

## 5.6 Supporting Information

Full movies of the measurements can be downloaded on the Web from <https://colloid.nl/>. The following movies are available:

- Movie S1: measurement of particle 7, corresponding to Figure 5.2
- Movie S2: measurement of a particle with a broken shell (particle 9), corresponding to Figure 5.3
- Movie S3: partial irradiation of particle 10, followed by rotations of the scanning direction, corresponding to Figure 5.8



# 6

---

## Hydration of MgO Nanocrystals to $\alpha$ -Mg(OH)<sub>2</sub> Monitored at Ambient Pressure by In Situ TEM

---

The hydration reaction of periclase MgO to  $\alpha$ -Mg(OH)<sub>2</sub> is a model hydration reaction and is important to diverse research fields, ranging from catalysis to Earth sciences. We monitor the hydration of MgO nanocrystals in real time and real space, at ambient pressure, and at the single particle level by means of in situ Transmission Electron Microscopy (TEM) using a flow holder. Upon exposure to water vapor and the electron beam, MgO nanocrystals react with water and convert to amorphous Mg(OH)<sub>2</sub>. Recordings of the hydration reaction reveal that the reaction starts at the MgO nanocrystal surface and proceeds inwards at a constant rate while the Mg(OH)<sub>2</sub> shell expands outwards, also at a constant rate. There is no noticeable conversion at electron beam dose rates below 70 electrons nm<sup>-2</sup> s<sup>-1</sup>. At higher values, the measured reaction rate linearly increases with dose rate. We hypothesize that the electron beam irradiation promotes the reaction by creating defects at the MgO{100} surface, thereby activating the MgO for hydroxylation and subsequently full hydration. The roughly linear relation between growth rate and dose rate as well as the dose rate threshold can be explained by this surface defect formation mechanism.

## 6.1 Introduction

Metal oxides, and especially metal oxide nanoparticles, constitute an important class of materials in a wide variety of fields including sensing, optoelectronics,<sup>181</sup> catalysis,<sup>182</sup> and Earth Sciences. The physical and chemical interactions of water with metal oxide surfaces is of general importance to Earth Sciences, as they are known to play a controlling role in processes such as dissolution, precipitation and adsorption.<sup>183</sup> These reactions can modify the composition and quality of natural waters and mediate atmospheric carbon dioxide removal,<sup>184</sup> and metal oxide nanoparticles have shown an increased capacity for scavenging environmental toxins.<sup>185</sup> Within the class of metal oxides, magnesium oxide (MgO) is commonly used as a model system due to its simple cubic crystal lattice and electronic structure. Furthermore, recent research has shown that MgO nanocrystals (NCs) have an enhanced CO<sub>2</sub> capturing capacity<sup>186</sup> and could substantially aid subsurface CO<sub>2</sub> sequestration via mineral carbonation.

This model hydration reaction is therefore also highly relevant in Earth Sciences, where crystalline MgO is known as periclase and Mg(OH)<sub>2</sub> as brucite. The brucite-periclase phase diagram has been determined experimentally for geologically relevant temperatures and pressures.<sup>187,188</sup> Hydroxides such as Mg(OH)<sub>2</sub> can be regarded as analogue materials to serpentine (Mg<sub>3</sub>Si<sub>2</sub>O<sub>5</sub>(OH)<sub>4</sub>), one of the most important hydrous mineral phases within the solid Earth. During plate tectonic movement, hydrous minerals are transported via subduction to the deep Earth, where increased temperature and pressure induce mineral dehydration. The storage and release of water in these minerals is a crucial part of the rock cycle on Earth.<sup>189</sup> The reverse process, the hydration of minerals such as periclase (MgO) and olivine (Mg<sub>2</sub>SiO<sub>4</sub>), are accompanied by large molar volume increases, suggested to promote reaction-induced fracturing of otherwise low-permeability rocks.<sup>190</sup> Hence, it is important that we understand the microscopic processes operating during solid phase hydration reactions, as they have consequences at much larger length scales.

Chemically pure MgO nanocrystals can be prepared by burning a magnesium ribbon in air. The smoke from this reaction contains cubic MgO NCs with edge lengths in the range of 50-200 nm.<sup>191,192</sup> The first step in the conversion to Mg(OH)<sub>2</sub> is hydroxylation of surface sites, whereby the MgO surface is functionalized with (OH)<sup>-</sup> groups. The equilibrium shapes and surface terminations of MgO particles have been studied extensively and the surface energies of these planes depend on the environmental conditions. In total, six surfaces can be considered; the bare and hydroxylated forms of the {001}, {110} and {111} surfaces. In a dry state, without any water molecules present, the non-polar {001} type surfaces are found to be the most stable, followed by the less stable non-polar {110} and the least stable polar {111} type surfaces.<sup>193</sup> This is in agreement with the experimental finding that bare MgO NCs form cubes with exclusively {001} facets. However, in the presence of water (gas or liquid), hydroxylation of

the surface takes place and the order of stability of the surfaces is reversed; the hydroxylated  $\{111\}$  surfaces have now become the most stable.<sup>192</sup> Under these conditions, the new equilibrium shape is an octahedron with eight  $\{111\}$  faces, although the restructuring process is slow (weeks for 200 nm NCs). This shape is indeed found in experiments after immersing cubic MgO smoke crystals in deionized water for seven days.<sup>194</sup> It is thus clear that the hydroxylated crystal faces are very inert and stable. Before the formation of the stable  $\{111\}$  faces, less energetically favorable  $\{110\}$  faces develop on the edges of the cubic crystal. Only after prolonged immersion in liquid water (several days) do  $\{111\}$  faces appear on the corners of the cube, eventually growing in size and finally resulting in a truncated octahedron. This process of surface restructuring has been successfully explained by means of Wulff constructions.<sup>192,194</sup> Eventually, and in particular at slightly elevated temperatures, MgO NCs in liquid water are found to fully convert to crystalline  $\text{Mg}(\text{OH})_2$ . The Gibbs free energy of this reaction at room temperature and ambient pressure is  $-35.6 \text{ kJ mol}^{-1}$ .<sup>195</sup> Like the surface restructuring, the conversion of the material is slow, despite the negative Gibbs free energy. However, the reaction rate increases for decreasing particle size and is strongly dependent on pH; increasing with decreasing pH.<sup>196</sup>

Various groups have investigated the reverse reaction in situ; the conversion of  $\text{Mg}(\text{OH})_2$  to MgO. Yamaguchi et al. investigated this transformation using Transmission Electron Microscopy (TEM).<sup>197</sup> Using both resistive and beam heating, they converted crystalline  $\text{Mg}(\text{OH})_2$  to MgO. From the diffraction patterns, they concluded that this change occurred around  $310^\circ\text{C}$ . Additionally, they reported the crystallographic orientation relation between the two phases, which has also been reported by many other authors.<sup>198–204</sup> Van Aken et al. used TEM and induced decomposition of  $\text{Mg}(\text{OH})_2$  with the electron beam.<sup>202</sup> They followed the release of water from the structure using Electron Energy Loss Spectroscopy (EELS). Using these EELS spectra, they calculated the average oxygen coordination number and were able to determine when crystalline  $\text{Mg}(\text{OH})_2$  had completely converted to MgO. McKelvy et al. used Environmental TEM (ETEM) at a water vapor pressure of 1 Torr to slow down the decomposition reaction.<sup>205</sup> Using either resistive heating or the electron beam, they observed lamellar dehydroxylation, where a plane of opposing OH-groups converted to a plane of oxygen atoms. During this process, which they named “delamination,” the overall crystal orientation was retained, but it also resulted in internal stresses in the crystal which led to fracturing.

The forward reaction of MgO to  $\text{Mg}(\text{OH})_2$  has also been studied by various groups. For a recent overview of available literature, we refer to the paper by Newberg et al., who performed an in situ XPS study of the conversion process at ambient pressure. They found that surface defects play an important role in the reaction. At low vapor pressure, hydroxylation only took place at point defects at the  $\text{MgO}\{100\}$  surface whereas at higher vapor pressure also terrace steps contributed greatly to the reaction.

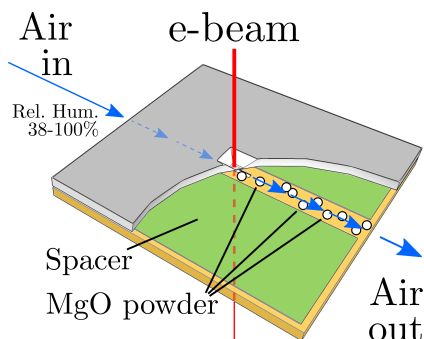


Figure 6.1: A schematic representation of the experimental setup for the in situ TEM flow experiments. A circular cut-out of the upper Si chip is not shown to better illustrate the setup. MgO nanocrystals were contained in a thin channel between two silicon chips with 50 nm thick silicon nitride windows. The channel is created by two 500 nm thick spacer layers. Air with a certain Relative Humidity (23 °C) was passed through the holder.

Gajdardziska-Josifovska et al. investigated the reaction using ETEM at a vapor pressures up to 0.53 Torr (0.71 mbar) or lower.<sup>206</sup> The MgO NCs converted to  $\text{Mg}(\text{OH})_2$  from the outside inwards, leaving a crystalline MgO core covered by a layer of amorphous  $\text{Mg}(\text{OH})_2$ . After longer exposure to water vapor, crystals swelled and left a disordered amorphous phase with large cavities, no longer reminiscent of the original crystals. Notably, they found that without the e-beam no reaction took place at all.

Unfortunately, it is not possible to directly relate the real space studies with the in situ studies performed at ambient conditions, as the real space TEM analysis of MgO NCs in liquid water were collected ex situ, the TEM analysis in the ETEM was performed at low pressures below 1 mbar, while the XPS, IR, and XPS in situ studies carried out in liquid water or at ambient pressure do not provide space-resolved information. To the best of our knowledge, there is no prior study combining real space imaging at the single particle level at ambient conditions with a pressure of about 1.0 bar.

In this work, we imaged crystalline MgO NCs at ambient pressure using in situ TEM using a Liquid Cell flow holder. The hydration to amorphous  $\text{Mg}(\text{OH})_2$  was followed at different water vapor concentrations, in real and reciprocal space, in real time, and at various electron beam current densities.

Table 6.1: Experimental conditions and average  $\text{Mg}(\text{OH})_2$  growth rates for all measurements.

No.	Air flow (RH)	Dose rate ( $\text{e nm}^{-2} \text{ s}^{-1}$ )	Time (s)	Frame dose ( $\text{e nm}^{-2}$ )	Growth rate ( $\text{pm s}^{-1}$ )	Figure
1	38%	2.1	1549	20.8	0	
2	38%	13.1	1703	65.7	0	
3	None	65	936	416	0	SI 1
4*	38%	76	2379	152	-	6.5, SI 5
5	38%	153	1316	767	9.5	6.3, SI 3
6	38%	228	2325	1142	9.6	
7	38%	263	1585	1316	17.3	
8	100%	324	2272	2074	9.2	6.2, SI 2
9	38%	330	308	1650	28	
10	38%	504	334	2522	23	
11	38%	1370	406	6848	76	SI 4

\* = diffraction mode

## 6.2 Experimental

Cubic MgO NCs in powder form, average crystal edge length 50 nm, was purchased from UBE Material Industries and used as received. Images were recorded using an Tecnai 20 electron microscope (FEI company, USA) equipped with a field emission source operating at 200 kV. In situ measurements were performed using a TEM liquid flow holder (Hummingbird Scientific, USA). The holder was used in flow mode in combination with a syringe pump, using a gas flow rate of  $10 \mu\text{L min}^{-1}$ . The actual flow rate in the viewing area of the liquid cell is likely lower, as the small spatial dimensions led to a locally higher flow resistance. The specimen was prepared by depositing MgO powder on a silicon chip with a  $50 \times 200 \mu\text{m}$  silicon nitride window (50 nm thickness). A second chip was placed on top, overlapping the windows. A 500 nm spacer layer on one of the silicon chips prevented direct contact of the windows and created a channel to allow for vapor flow. The two chips were then placed in the tip of a sample holder and the assembly was closed. A schematic of the experimental setup is shown in Figure 6.1. This sample preparation and assembly was carried out at 21 °C, 45% relative humidity (RH) and took several minutes. The holder was inserted in the microscope and tubing for the vapor flow was connected. Vapor flow with different RH was created as follows. Saturated vapor (RH = 100%) at room temperature was created by pass-

ing ambient air through a vial partially filled with deionized water. The atmosphere above the liquid was flowed through the tubing of the TEM holder, through the channel between the silicon chips, and out of the other side of the holder. The temperature in the microscope room during the measurements was 23 °C. Although the temperature of the liquid cell in the microscope was not controlled, the increase in temperature due to the beam has been calculated to be negligible for the dose rates used in this work.<sup>175</sup> Air containing a lower concentration of water vapor was created using a sealed reservoir partially filled with water and equipped with a temperature and humidity sensor. The reservoir was equilibrated at 7.2 °C for several hours. After equilibration, the atmosphere inside the vessel was measured to be 100.0% RH, which is equivalent to 38% RH at 23 °C (the temperature in the room during the measurement). Relative humidities in the rest of the text are all stated for 23 °C. A syringe was filled with some of the atmosphere from the reservoir and allowed to reach room temperature. The syringe was subsequently placed in a syringe pump and connected to the TEM holder. Regions of interest were illuminated continuously with the electron beam at a constant beam current. Movies were recorded using a BM Multiscan CCD camera. The dose rate, total illumination time, and frame dose for each experiment are given in Table 6.1.

### 6.3 Results

MgO NCs were imaged and monitored for beam effects as a result of prolonged irradiation without air flow through the TEM holder (see Supporting Information movie S1 for full recording). Aside from some sample drift, no change was observed after 936 seconds at a dose rate of  $65 \text{ e nm}^{-2} \text{ s}^{-1}$ . Subsequently, a water vapor flow (100% RH, 23 °C) was started and a new cluster of MgO NCs was imaged for 2722 seconds at an electron dose rate of  $324 \text{ e nm}^{-2} \text{ s}^{-1}$ . The beginning, middle and end of this movie are shown in Figure 6.2A (Supporting Information movie S2). At the start of the measurement, a thin layer of amorphous material was already present around the MgO cores. The crystalline MgO cores could be easily distinguished from the amorphous shell ( $\text{Mg}(\text{OH})_2$ ) by its strong diffraction contrast. Diffraction contrast is typical for crystalline material and is caused by electrons reflecting off of the crystal planes when the angle of the NC with respect to the incident beam satisfies the diffraction condition. The diffraction condition is highly sensitive to this angle and small rotations result in large changes in contrast of the material. Moreover, diffracted electrons of a particular crystal may appear as a bright spot with the same shape elsewhere in the image. One such spot is indicated with an arrow in Figure 6.2C. The MgO cores in the movies clearly exhibited diffraction contrast, confirming that they were crystalline. The  $\text{Mg}(\text{OH})_2$  shell was amorphous as it did not show this effect; its contrast only depended on its

thickness.

The hydration reaction started on the outside surface of the cubic MgO NCs and proceeded inward, consuming the MgO and converting it to an amorphous Mg(OH)<sub>2</sub> shell. MgO has a higher density than Mg(OH)<sub>2</sub> (more than double compared to crystalline Mg(OH)<sub>2</sub>).<sup>199</sup> Therefore, the total volume of the MgO/Mg(OH)<sub>2</sub> particle increased as the conversion proceeded. Three NCs are highlighted in Figure 6.2A. Detailed images of these NCs throughout the reaction are shown in Figure 6.2B-D. For each region of interest, the movie was drift-corrected to obtain a stable movie of the NC to be analyzed. A line was drawn across the NC as indicated by the yellow lines in Figure 6.2B-D, and the pixel intensity along these lines was measured as the reaction proceeded. These line profiles are plotted in Figure 6.2E where the pixel intensity is shown as a color table (linearly stretched from zero to 255 to optimize contrast). This allowed for quantitative monitoring of the evolution of the NC core and shell. From the straight slopes in Figure 6.2E it is clear that the shrinkage of the MgO core and the growth of the Mg(OH)<sub>2</sub> shell were nearly constant in time. The diameter of the crystalline MgO core decreased by 13 nm and the average increase in the shell thickness was 22 nm over 2722 seconds, giving a growth rate of 9.2 pm s<sup>-1</sup>. The experimental conditions and average growth rates are summarized in Table 6.1. Additionally, expansion of the converting NCs caused significant shifts and movement among large assemblies of NCs, as can be seen in Figure 6.2A.

A second experiment was performed, with new silicon chips and fresh MgO powder, while flowing air with a RH of 38%. MgO NCs were exposed to the electron beam at a dose rate of 153 e nm<sup>-2</sup> s<sup>-1</sup>. Frames from the resulting movie are shown in Figure 6.3 (Supporting Information movie S3). The analysis was performed in the same manner as described above and the results were qualitatively similar to those obtained at higher RH. The growth rate of the Mg(OH)<sub>2</sub> shell (the distance between the MgO/Mg(OH)<sub>2</sub> interface and the outer surface) was again found to be constant throughout the exposure, with an average value of 9.5 pm s<sup>-1</sup>, which is almost identical to the value obtained at higher RH.

Additional measurements were performed at various electron beam dose rates. Each measurement was carried out on NCs that had not yet been exposed to the electron beam. Movies were recorded in real space while flowing 38% RH air. Growth rates of the Mg(OH)<sub>2</sub> shell were obtained in the same way as described above and were all found to be constant throughout the measurement. The growth rate of the Mg(OH)<sub>2</sub> shell is plotted versus electron dose rate in Figure 6.4. Below a dose rate of 65 e nm<sup>-2</sup> s<sup>-1</sup> no reaction was detected, even after prolonged exposure. Above a dose rate of approximately 70 e nm<sup>-2</sup> s<sup>-1</sup>, the particle size increased due to the formation of an amorphous layer around the NC, indicating that the NCs reacted with water vapor. In this dose rate range, the reaction rate was found to increase with increasing dose rate. Above a total electron dose of approximately 1-2 10<sup>4</sup> e nm<sup>-2</sup>, nanocavities started

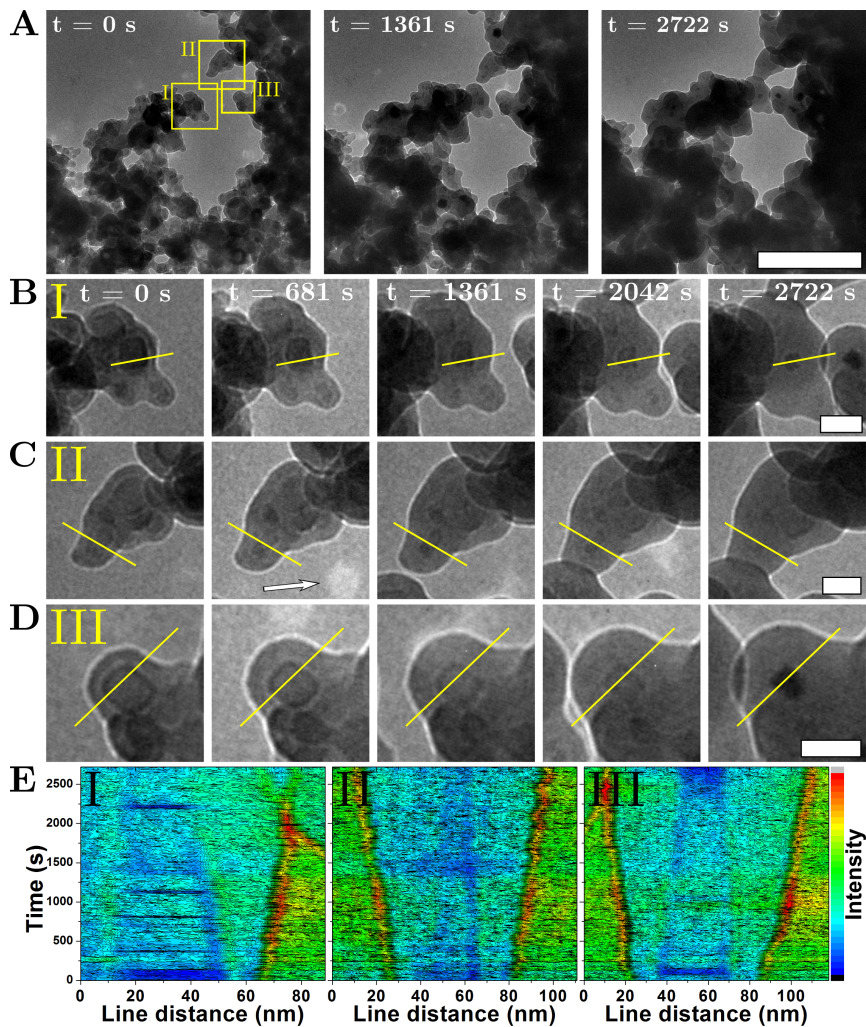


Figure 6.2: In situ hydration of MgO NCs during exposure to air with 100% RH at 23 °C and a dose rate of  $324 \text{ e nm}^{-2} \text{ s}^{-1}$ . **A:** images of the cluster at the start, halfway and at the end of the reaction (scalebar is 500 nm). Detailed view of regions I, II and III are shown in **B-D** (scalebars are 50 nm). The arrow in **C** points to a bright spot caused by the diffraction contrast of the NCs. **E:** the intensity profile along the lines drawn in **B-D** evolving in time, showing the constant shrinkage of the MgO core and constant growth of the Mg(OH)<sub>2</sub> shell. Colors represent intensity gray values (0-255). The full recording is available in Supporting Information as movie S2.

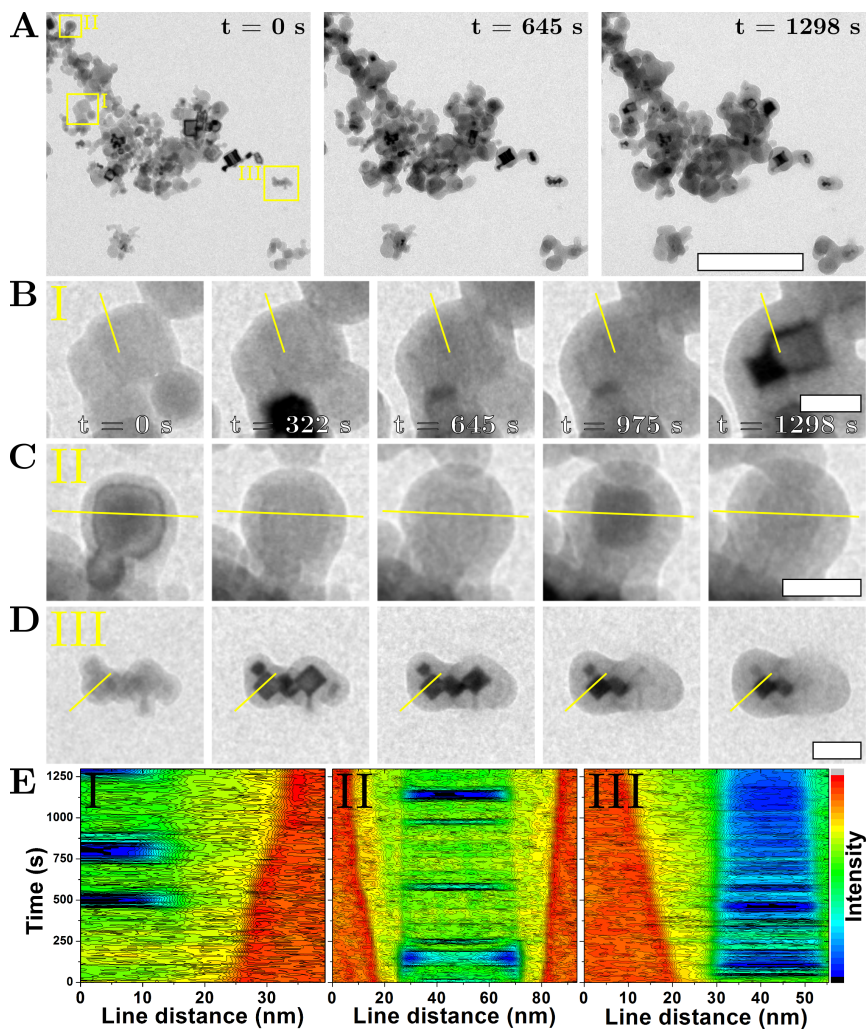


Figure 6.3: In situ hydration of MgO NCs during exposure to air with 38% RH at 23 °C and a dose rate of  $153 \text{ e nm}^{-2} \text{ s}^{-1}$ . **A**: images of the start, middle and end of the reaction (scalebar is 500 nm). **B-D** show the detailed regions I, II and III (scalebars are 50 nm). **E**: the intensity profile along the lines drawn in **B-D** evolving in time. Colors represent intensity gray values (0-255). See Supporting Information movie S3.

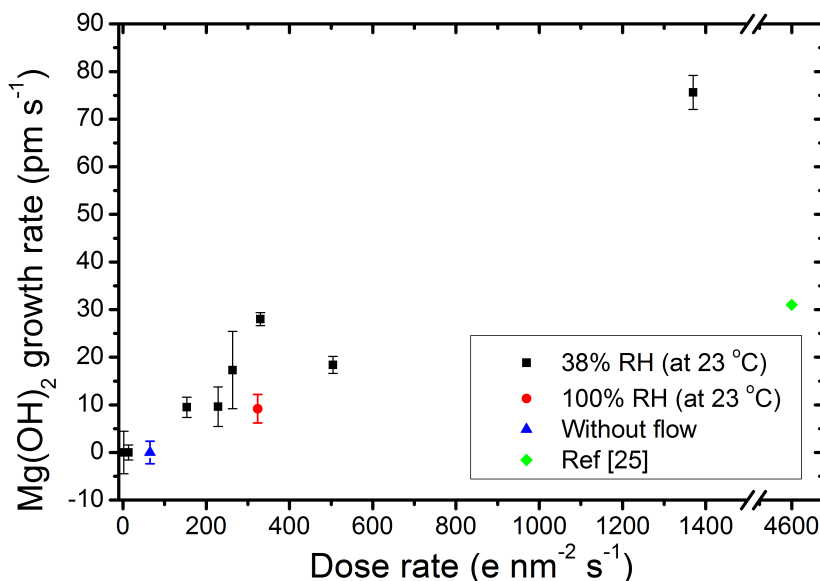


Figure 6.4: Growth rate of the  $\text{Mg(OH)}_2$  shell as a function of dose rate while flowing air with either 38% or 100% RH at 23 °C or without flow. The experiment in Ref. [206] was performed at 2% RH.

to appear in the amorphous  $\text{Mg(OH)}_2$  (see Supporting Information movie S4). Moreover, these nanocavities were observed in experiments using dose rates from 228 to 1370  $e \text{ nm}^{-2} \text{ s}^{-1}$ .

In addition to the real space studies, the reaction was also monitored in reciprocal space. A large cluster of MgO NCs, not previously exposed to the electron beam, was irradiated for 2379 seconds at a dose rate of 76  $e \text{ nm}^{-2} \text{ s}^{-1}$  while flowing 38% RH air. Figure 6.5 shows the real space images and the corresponding diffraction patterns before and after exposure to the electron beam (Supporting Information movie S5). MgO reference data and lattice constants were obtained from WEBEMAPS.<sup>207</sup> The yellow dashed circles indicate the area irradiated to record the diffraction patterns. Radial averages of the diffraction patterns recorded during the reaction are plotted in Figure 6.5C. The diffraction data show the loss of crystallinity over time, which is consistent with the real space images. Also, it is clear from the real space image that the reaction only occurred in the irradiated area, and that NCs just outside the irradiated area remained crystalline.

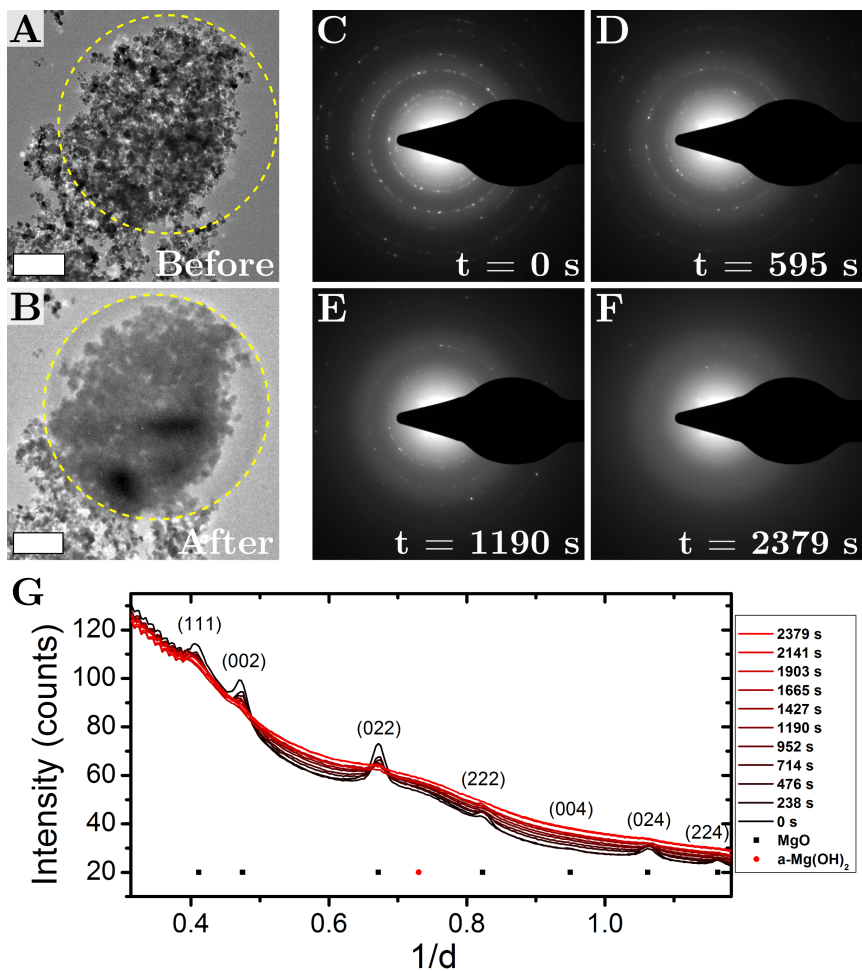


Figure 6.5: The hydration of MgO NCs monitored in diffraction space. NCs were exposed to a dose rate of  $76 \text{ e nm}^{-2} \text{ s}^{-1}$  for 2379 seconds while flowing air with 38% RH at  $23 \text{ }^\circ\text{C}$ . A bright field image of a large cluster before and after exposure is shown in **A** and **B** (scalebars are 500 nm). The dashed yellow circles outline the irradiated area. **C-F**: stills from diffraction pattern recording. The radial averages of the diffraction patterns are plotted in **G**, along with the known reflections for MgO. The reciprocal space was calibrated from the MgO reflections. Full recording can be found in the Supporting Information as movie S5.

## 6.4 Discussion

Below, we will discuss the dependence on the electron dose rate and the Relative Humidity (RH), and elaborate on the formation of the amorphous  $\text{Mg}(\text{OH})_2$  shell. Furthermore, we propose a mechanism to explain the experimental observations.

### 6.4.1 Electron beam activation

The electron beam played a crucial role in the hydration reaction. Without the e-beam irradiation, no reaction took place and the MgO NCs remained completely crystalline. This is consistent with the findings that even MgO NCs immersed in liquid water (outside the TEM) required several days to convert to  $\text{Mg}(\text{OH})_2$ ,<sup>192</sup> which is at a time scale much larger than in our experiments (five to 60 minutes). The promotion of the reaction by the e-beam could be related to several factors such as a local temperature increase (on short time scales), ionizations and excitations, cleavage of chemical bonds in the MgO and/or adsorbed water, or a combination of these effects. The boundary between irradiated/reacted and unreacted NCs can be seen clearly in Figure 6.5B and the dependence of the MgO conversion on the e-beam allowed for sequential initiation of hydration reactions in the same sample. Furthermore, there appeared to be a minimum electron dose rate needed to promote the hydration reaction. MgO cubes irradiated at a dose rate of  $65 \text{ e nm}^{-2} \text{ s}^{-1}$  (movie S1), showed no sign of transformation, even after accumulating a total dose of more than  $6 \cdot 10^4 \text{ e nm}^{-2}$ . The NC cluster in movie S1 consisted of many irregularly connected particles, so even a small (sub-pixel) growth of each NC would have led to a large increase in the overall cluster size. No such increase was observed, from which we concluded that at the dose rate of  $65 \text{ e nm}^{-2} \text{ s}^{-1}$  the reaction rate was very close to zero. However, in the diffraction experiment (Figure 6.5, movie S5) the NCs were exposed to a dose rate of  $76 \text{ e nm}^{-2} \text{ s}^{-1}$  and these NCs clearly reacted. Thus, the threshold for promoting the reaction was approximately  $70 \text{ e nm}^{-2} \text{ s}^{-1}$ .

Above the threshold of  $70 \text{ e nm}^{-2} \text{ s}^{-1}$ , e-beam irradiation resulted in conversion of the MgO NCs to  $\text{Mg}(\text{OH})_2$  on the order of (tens of) minutes. The growth rate of the  $\text{Mg}(\text{OH})_2$  layer was used to quantify the reaction rate of the hydration reaction. Constant  $\text{Mg}(\text{OH})_2$  growth rates were found for all dose rates above the threshold and monotonously increased for each higher dose rate, indicating that reaction kinetics were similar throughout this range of dose rates. Growth rates varied slightly among NCs measured in a single experiment, likely due to variations in local environment such as RH, local flow rate and proximity to other (clusters of) NCs.

### 6.4.2 Effect of Relative Humidity

No difference in reaction rate was observed when flowing air with different RH, indicating that the reaction was not sensitive to the concentration of water vapor in the range between 38% and 100%. From this we concluded that the availability of water vapor was not part of the rate-limiting step of the hydration process. In previous work, Gajdardziska-Josifovska et al. monitored the same reaction using ETEM at 0.41 Torr water pressure, which corresponds to a RH in our experiment of 2.0%.<sup>206</sup> From their results, we have calculated a growth rate of  $31 \text{ pm s}^{-1}$  at their reported dose rate of  $4.6 \cdot 10^3 \text{ e nm}^{-2} \text{ s}^{-1}$ . This growth rate is lower than what we find in our experiments, despite their higher dose rate. It is possible that under these conditions the availability of water could have become the limiting factor, resulting in a lower reaction rate. This indicates that given the right conditions, the reaction rate could perhaps be tuned through the RH while keeping the dose rate constant.

### 6.4.3 Formation of amorphous $\text{Mg}(\text{OH})_2$

We observed only the formation of amorphous  $\text{Mg}(\text{OH})_2$ . It is possible that the temperature was not high enough to induce crystallization of the  $\text{Mg}(\text{OH})_2$ , or that the growth rate was too high to allow crystallization to occur. Heating due to the electron beam has been calculated to be  $10^{-2}$ - $10^{-3}$  K for the dose rates used here.<sup>175</sup> Another possibility is that crystalline  $\text{Mg}(\text{OH})_2$  was continuously formed but then amorphized by the electron beam. Conducting similar experiments at elevated temperature will make the internal dynamics of the system more evident and decrease the importance of beam induced effects and possibly lead to the formation of crystalline  $\text{Mg}(\text{OH})_2$ . From ex situ experiments it is known that crystalline  $\text{Mg}(\text{OH})_2$  is normally found. The nanocavities that appeared in the  $\text{Mg}(\text{OH})_2$  above an electron dose of  $1$ - $2 \cdot 10^4 \text{ e nm}^{-2}$  were most likely caused by radiation damage, leading to the boiling of water (either adsorbed water or molecules in the  $\text{Mg}(\text{OH})_2$  structure), generation of gases such as  $\text{H}_2$ , or sublimation of the material. However, because the  $\text{Mg}(\text{OH})_2$  shell thickness and the accumulated dose were directly correlated, the formation of nanocavities may also be connected to the thickness of the shell impacting transport or relaxation mechanisms within the material.

### 6.4.4 Reaction mechanism

In this section, we present a plausible mechanism for the electron beam induced transformation of  $\text{MgO}$  to  $\text{Mg}(\text{OH})_2$ , involving the creation of defects on the  $\text{MgO}$  surface by the electron beam. This mechanism explains the experimental observations presented in Figure 6.2E and Figure 6.3E, showing that the velocity of the reaction front was constant in time, and that the reaction occurred only in the area exposed by the electron beam.

Additionally, our mechanism reproduces the linear dependence on the dose rate and can explain the dose rate threshold ( $70 \text{ e nm}^{-2} \text{ s}^{-1}$ ).

The availability of water vapor or generation of reactive species from water molecules were also considered as possible mechanisms that governed the transformation reaction. However, as discussed earlier, the growth rate of the  $\text{Mg}(\text{OH})_2$  shell did not change with shell thickness nor was it sensitive to the concentration of water vapor. Therefore, it is unlikely that the diffusion of water to the NC surface/interface was the limiting step. The transformation of  $\text{MgO}$  to  $\text{Mg}(\text{OH})_2$  could have been the result of the beam induced generation of active/reactive species from water molecules. Activation through excitation of the water can involve many different species, such as excited water molecules and dissociation products including  $\text{H}^+$ ,  $\text{H}_3\text{O}^+$ ,  $\text{OH}^-$ , hydrated electrons, and clusters of multiple molecules or ions.<sup>32</sup> Moreover,  $\text{MgO}$  is known to be highly susceptible to hydration in acidic media, and therefore  $\text{H}^+$ ,  $\text{H}_3\text{O}^+$  are plausible candidates for causing an increased reaction rate.<sup>201</sup> If generation of reactive water species by the electron beam was the dominating mechanism, then it is to be expected that the reaction rate would scale approximately linearly with the dose rate, in agreement with the observations. However, this does not explain the experimentally observed threshold dose rate below which no reaction occurred within the time frames of our experiments. Additionally, the reactive water species that are generated by the electron beam could diffuse out of view, resulting in transformations in particles outside the field of view, which we did not observe.

The generation of similar reactive species in the  $\text{MgO}$  itself, such as surface defects, can explain the experimental observations. Previous studies of hydroxylation and hydration of  $\text{MgO}$  describe that the presence of defects at the  $\text{MgO}\{100\}$  surface greatly enhances the reaction rate. In the in situ XPS study by Newberg et al.,<sup>208</sup> it is described that at low levels of RH, dissociative adsorption takes place only at defect sites, and that at higher RH levels hydroxylation occurs also at terrace sites of the  $\text{MgO}(100)$  surface. Therefore, introduction of defects in  $\text{MgO}$  by the electron beam could very likely promote the reaction. Additionally, the highly local effect of the electron beam can be adequately explained, as  $\text{MgO}$  can not diffuse out of the field of view. The threshold dose rate may be related to the combination and reconstructing of defects; if the dose rate - and through it the defect generation rate - is too low, then the defect density on the surface may not be high enough for defects to combine into more stable yet reactive crystal faces before restructuring back into a smooth surface. Thus, only above a certain defect density would more stable crystal faces appear on the surface. Surface modification by e-beam irradiation is discussed into more detail in the following section.

### MgO surface modification

The activation of the MgO is likely related to MgO surface modification by the e-beam. Bare MgO{100} surfaces (the six facets of the MgO nanocubes) are very stable and chemically inert, but for example the polar MgO{111} surfaces (absent under equilibrium conditions in vacuum) are much more reactive. As a plausible explanation, we suggest that the electron beam generates many Frenkel defects (vacancy-interstitial pairs) at the surface, thereby creating adatoms, ridges, and unstable nanofacets which then become available for the hydroxylation/hydration reaction. Electrons with a beam energy of 200 keV will completely pass through the holder with the MgO sample and will in general be only slightly deviated from their incident direction, but will generally create electronic excitations and possibly atomic displacements along their path. The beam energy of 200 keV is not sufficient to create atomic displacements (so-called knock-on damage, O and Mg Frenkel pairs) in bulk MgO. The recommended threshold displacement energy for O and Mg is 55 eV for both atoms.<sup>209</sup> These threshold displacement energies are always higher than defect formation energies because of the out-of-equilibrium conditions during collisions (amongst others, the surrounding lattice does not have time to relax during the collision). The threshold displacement energies are related to threshold electron beam acceleration energies  $E_{th}$  through the relationship<sup>31,209</sup>

$$E_d = E_{th}(1.02 + /10^{-6} E_{th})/(465.7 * A) \quad (5)$$

where both energies are in eV and A is the atomic mass in a.m.u. (16.0 for O and 24.3 for Mg). This yields values of  $E_{th}$  of 309 keV for O and 430 keV for Mg. Therefore, Frenkel defect formation in MgO bulk will not take place at acceleration voltages of 200 kV. However, it is also known that for generation of defects at surfaces (surface sputtering), only about a quarter to a half of that acceleration voltage is required,<sup>210</sup> making surface modification by e-beam irradiation a likely process at 200 kV. To partially validate this hypothesis by simulations, density functional theory (DFT) calculations were performed on defective MgO{100} surfaces, and it was found that the formation energy of Frenkel defects at the surface is substantially lower than in the bulk [H. van Gog, M. Dijkstra, M.A. van Huis, unpublished results]. Furthermore, a multitude of defect states is generated in the band gap when Frenkel defects are introduced at the surface, suggesting that the defective MgO{100} surface is more likely to undergo chemical reactions in general. The proposed mechanism of surface modification explains, first of all, that the reaction rate scales more or less linearly with the electron dose rate. Second, it explains the dose rate threshold. The defective MgO surface will survive as long as the beam intensity is sufficiently high. When the dose rate drops below the threshold value, there is sufficient time for the MgO surface to reconstruct back into a nearly perfect MgO{100} surface (the defects are 'annealed out' at room temperature), so that the reaction is nearly halted and is no longer

observed. Third, activation through the non-mobile MgO is consistent with the highly local effect of the e-beam. We therefore believe that e-beam induced MgO surface modification is the dominating mechanism for activation of MgO hydration. Of course, the reaction may also be aided by water activation and its radicals and ionic species that are formed as a product of water radiolysis, if these deactivate quickly with respect to diffusion out of the irradiated region. Finally, we mention that other effects may play a role as well. MgO is known as an efficient secondary electron emitter, in particular upon charging of the crystal, and is integrated for that purpose in photomultiplier tubes and plasma screens. Charging effects and secondary electron emission may assist in generating excited electronic states at the MgO surface and adjacent water molecules.

For the overall reaction, the generation of reactive species and the hydration reaction itself are possible rate-limiting steps, having ruled out the dependence on diffusion of water from the sample cell. If the activation step is rate-limiting, then the concentration of active species would be close to zero and any active species that are produced will immediately react further. Conversely, if the hydration is rate-limiting, then reactants are produced more quickly than they are consumed, leading to an increase of reactant concentration instead of conversion to  $\text{Mg}(\text{OH})_2$ . This build-up of reactants accelerates the hydration reaction until it is equally fast as the production of the reactants. If the build up of reactants occurs within the first few frames of our measurement, then the reaction rate will have stabilized at a constant value also yielding a constant growth rate in our measurements. However, the lack of sensitivity of the reaction rate to the water vapor concentration indicates that the hydration reaction is not affected by increased concentration of reactants. Therefore, the rate-limiting step is most likely the production of active species, i.e. the generation of defects on the surface of the  $\text{MgO}\{100\}$ .

## 6.5 Conclusion

The hydration of MgO NCs to  $\text{Mg}(\text{OH})_2$  in the presence of water vapor was monitored by in situ TEM at ambient pressure ( $\sim 1.0$  bar), allowing us to extract growth rates at the single crystal particle level. We found that the reaction started at the NC surface and that the reaction front moved inwards at a constant rate, while the  $\text{Mg}(\text{OH})_2$  shell grew outwards at a constant rate. From a comparison of experiments performed at different electron beam dose rates, it was found that the reaction rate increased with increasing electron beam dose rate. The reaction was found not to take place below a threshold dose rate of  $70 \text{ e nm}^{-2} \text{ s}^{-1}$ . These observations can be plausibly explained by a reaction mechanism in which the e-beam creates defects on the MgO surface, thereby activating it for hydroxylation and subsequent full hydration to amorphous  $\text{Mg}(\text{OH})_2$ . The creation of

these defects is likely the rate limiting step, although it is expected that the process is also aided by activated water molecules and dissociation products from hydrolysis, such as  $\text{H}^+$  and  $(\text{OH})^-$  ions. Above a total electron dose of  $1\text{--}2 \times 10^4 \text{ e nm}^{-2}$  nanocavities appeared in the amorphous  $\text{Mg}(\text{OH})_2$ , most likely due to radiation damage. In summary, from the in situ observations, we have quantified the growth rates at the single particle level and we have presented a plausible reaction mechanism to explain both the irradiation threshold and the enhanced conversion at higher electron beam dose rates.

## 6.6 Acknowledgments

The authors wish to thank Hans Meeldijk and Chris Schneijdenberg for support with the electron microscopes, and would like to acknowledge Krijn de Jong and Jovana Zečević for helpful discussions.

## 6.7 Supporting Information

Full movies of the measurements can be downloaded on the Web from <https://colloid.nl/>. The following movies are available:

- Movie S1: MgO NCs remaining unaffected while being irradiated at a dose rate of  $65 \text{ e nm}^{-2} \text{ s}^{-1}$
- Movie S2: measurement corresponding to Figure 6.2
- Movie S3: measurement corresponding to Figure 6.3
- Movie S4: generation of nanocavities in NCs irradiated at a dose rate of  $1370 \text{ e nm}^{-2} \text{ s}^{-1}$
- Movie S5: recording of the diffraction pattern, corresponding to Figure 6.5



---

# References

---

- [1] *Definition and Classification of Colloids*. [http://old.iupac.org/reports/2001/colloid\\_2001/manual\\_of\\_s\\_and\\_t/node33.html](http://old.iupac.org/reports/2001/colloid_2001/manual_of_s_and_t/node33.html). [Accessed Aug. 2017].
- [2] A. Einstein, *Über die von der molekularkinetischen Theorie der Wärme geforderte Bewegung von in ruhenden Flüssigkeiten suspendierten Teilchen*. *Ann. Phys.*, 322(8):549–560, Jan. 1905.
- [3] A. Yethiraj and A. van Blaaderen, *A colloidal model system with an interaction tunable from hard sphere to soft and dipolar*. *Nature*, 421(6922):513–517, Jan. 2003.
- [4] D. Babič, C. Schmitt, and C. Bechinger, *Colloids as model systems for problems in statistical physics*. *Chaos*, 15(2):026114, June 2005.
- [5] M. E. Leunissen, C. G. Christova, A.-P. Hynninen, C. P. Royall, A. I. Campbell, A. Imhof, M. Dijkstra, R. van Roij, and A. van Blaaderen, *Ionic colloidal crystals of oppositely charged particles*. *Nature*, 437(7056):235–240, Sept. 2005.
- [6] G. Malescio, *Intermolecular potentials — past, present, future*. *Nat Mater*, 2(8):501–503, Aug. 2003.
- [7] B. V. Derjaguin and L. Landau, *Theory of the Stability of Strongly Charged Lyophobic Sols and of the Adhesion of Strongly Charged Particles in Solutions of Electrolytes*. *Acta Phys. Chim. URSS*, 14:633–662, 1941.
- [8] E. J. W. Verwey and J. T. G. Overbeek. *Theory of the stability of lyophobic colloids : the interaction of sol particles having an electric double layer*. New York, Elsevier Pub. Co, 1948.
- [9] J. W. Goodwin, R. H. Ottewill, and R. Pelton, *Studies on the preparation and characterization of monodisperse polystyrene latices V.: The preparation of cationic latices*. *Colloid & Polymer Sci*, 257(1):61–69, Jan. 1979.
- [10] G. Bosma, C. Pathmamanoharan, E. H. A. de Hoog, W. K. Kegel, A. van Blaaderen, and H. N. W. Lekkerkerker, *Preparation of Monodisperse, Fluorescent PMMA–Latex Colloids by Dispersion Polymerization*. *Journal of Colloid and Interface Science*, 245(2):292–300, Jan. 2002.
- [11] B. Peng, E. van der Wee, A. Imhof, and A. van Blaaderen, *Synthesis of Monodisperse, Highly Cross-Linked, Fluorescent PMMA Particles by Dispersion Polymerization*. *Langmuir*, 28(17):6776–6785, May 2012.

- [12] A. van Blaaderen, J. Van Geest, and A. Vrij, *Monodisperse colloidal silica spheres from tetraalkoxysilanes: Particle formation and growth mechanism*. *Journal of Colloid and Interface Science*, 154(2):481–501, Dec. 1992.
- [13] A. F. Demirörs, A. van Blaaderen, and A. Imhof, *A General Method to Coat Colloidal Particles with Titania*. *Langmuir*, 26(12):9297–9303, June 2010.
- [14] A. F. Demirörs, A. Jannasch, P. D. J. van Oostrum, E. Schäffer, A. Imhof, and A. van Blaaderen, *Seeded Growth of Titania Colloids with Refractive Index Tunability and Fluorophore-Free Luminescence*. *Langmuir*, 27(5):1626–1634, Mar. 2011.
- [15] M. A. Haq, Y. Su, and D. Wang, *Mechanical properties of PNIPAM based hydrogels: A review*. *Materials Science and Engineering: C*, 70:842–855, Jan. 2017.
- [16] W. Stöber, A. Fink, and E. Bohn, *Controlled growth of monodisperse silica spheres in the micron size range*. *Journal of Colloid and Interface Science*, 26(1):62–69, Jan. 1968.
- [17] R. K. Iler. *The Chemistry of Silica: Solubility, Polymerization, Colloid and Surface Properties and Biochemistry of Silica*. Wiley, New York, 1979.
- [18] C. J. Brinker, *Hydrolysis and condensation of silicates: Effects on structure*. *Journal of Non-Crystalline Solids*, 100(1):31–50, Mar. 1988.
- [19] J. K. Bailey and M. L. Mecartney, *Formation of colloidal silica particles from alkoxides*. *Colloids and Surfaces*, 63(1):151–161, May 1992.
- [20] D. Pontoni, T. Narayanan, and A. R. Rennie, *Time-Resolved SAXS Study of Nucleation and Growth of Silica Colloids*. *Langmuir*, 18(1):56–59, Jan. 2002.
- [21] C. C. M. C. Carcouët, M. W. P. van de Put, B. Mezari, P. C. M. M. Magusin, J. Laven, P. H. H. Bomans, H. Friedrich, A. C. C. Esteves, N. A. J. M. Sommerdijk, R. A. T. M. van Benthem, and G. de With, *Nucleation and Growth of Monodisperse Silica Nanoparticles*. *Nano Lett.*, 14(3):1433–1438, Mar. 2014.
- [22] G. H. Bogush and C. F. Zukoski, *Uniform silica particle precipitation: An aggregative growth model*. *Journal of Colloid and Interface Science*, 142(1):19–34, Mar. 1991.
- [23] G. H. Bogush and C. F. Zukoski, *Studies of the kinetics of the precipitation of uniform silica particles through the hydrolysis and condensation of silicon alkoxides*. *Journal of Colloid and Interface Science*, 142(1):1–18, Mar. 1991.
- [24] A. van Blaaderen and A. Vrij, *Synthesis and characterization of colloidal dispersions of fluorescent, monodisperse silica spheres*. *Langmuir*, 8(12):2921–2931, Dec. 1992.
- [25] M. J. Williamson, R. M. Tromp, P. M. Vereecken, R. Hull, and F. M. Ross, *Dynamic microscopy of nanoscale cluster growth at the solid–liquid interface*. *Nat Mater*, 2(8):532–536, Aug. 2003.
- [26] N. de Jonge and F. M. Ross, *Electron microscopy of specimens in liquid*. *Nat Nano*, 6(11):695–704, Nov. 2011.

- [27] D. R. Ciarlo, *Silicon Nitride Thin Windows for Biomedical Microdevices*. Biomedical Microdevices, 4(1):63–68, Mar. 2002.
- [28] J. F. Creemer, S. Helveg, G. H. Hoveling, S. Ullmann, A. M. Molenbroek, P. M. Sarro, and H. W. Zandbergen, *Atomic-scale electron microscopy at ambient pressure*. Ultramicroscopy, 108(9):993–998, Aug. 2008.
- [29] N. de Jonge, D. B. Peckys, G. J. Kremers, and D. W. Piston, *Electron microscopy of whole cells in liquid with nanometer resolution*. PNAS, 106(7):2159–2164, Feb. 2009.
- [30] J. M. Grogan, N. M. Schneider, F. M. Ross, and H. H. Bau, *Bubble and Pattern Formation in Liquid Induced by an Electron Beam*. Nano Lett., 14(1):359–364, Jan. 2014.
- [31] R. F. Egerton, P. Li, and M. Malac, *Radiation damage in the TEM and SEM*. Micron, 35(6):399–409, Aug. 2004.
- [32] N. M. Schneider, M. M. Norton, B. J. Mendel, J. M. Grogan, F. M. Ross, and H. H. Bau, *Electron–Water Interactions and Implications for Liquid Cell Electron Microscopy*. J. Phys. Chem. C, 118(38):22373–22382, Sept. 2014.
- [33] X. Huang and M. A. El-Sayed, *Plasmonic photo-thermal therapy (PPTT)*. Alexandria Journal of Medicine, 47(1):1–9, Mar. 2011.
- [34] A. Okada, D. Nagao, T. Ueno, H. Ishii, and M. Konno, *Colloidal Polarization of Yolk/Shell Particles by Reconfiguration of Inner Cores Responsive to an External Magnetic Field*. Langmuir, 29(28):9004–9009, July 2013.
- [35] A. van Blaaderen and P. Wiltzius, *Real-Space Structure of Colloidal Hard-Sphere Glasses*. Science, 270(5239):1177–1179, Nov. 1995.
- [36] M. N. van der Linden, D. El Masri, M. Dijkstra, and A. van Blaaderen, *Expansion of charged colloids after centrifugation: formation and crystallisation of long-range repulsive glasses*. Soft Matter, 9(48):11618–11633, Nov. 2013.
- [37] D. H. Napper. *Polymeric Stabilisation of Colloidal Dispersions*. Academic Press, London, 1984.
- [38] R. J. Hunter. *Foundations of colloid science*. Oxford New York Oxford University Press, second edition edition, 2001.
- [39] C. P. Royall, M. E. Leunissen, A.-P. Hynninen, M. Dijkstra, and A. van Blaaderen, *Re-entrant melting and freezing in a model system of charged colloids*. The Journal of Chemical Physics, 124(24):244706, June 2006.
- [40] R. Piazza, S. Buzzaccaro, E. Secchi, and A. Parola, *On the general concept of buoyancy in sedimentation and ultracentrifugation*. Phys. Biol., 10(4):045005, 2013.
- [41] R. Piazza, *Settled and unsettled issues in particle settling*. Rep. Prog. Phys., 77(5):056602, 2014.
- [42] R. Piazza, T. Bellini, and V. Degiorgio, *Equilibrium sedimentation profiles of screened charged colloids: A test of the hard-sphere equation of state*. Phys. Rev. Lett., 71(25):4267–4270, Dec. 1993.
- [43] R. van Roij, *Defying gravity with entropy and electrostatics: sedimentation of charged colloids*. J. Phys.: Condens. Matter, 15(48):S3569, 2003.

- [44] M. Raša and A. P. Philipse, *Evidence for a macroscopic electric field in the sedimentation profiles of charged colloids*. *Nature*, 429(6994):857–860, June 2004.
- [45] C. P. Royall, R. v. Roij, and A. v. Blaaderen, *Extended sedimentation profiles in charged colloids: the gravitational length, entropy, and electrostatics*. *J. Phys.: Condens. Matter*, 17(15):2315, 2005.
- [46] A.-P. Hynninen, R. v. Roij, and M. Dijkstra, *Sedimentation profiles of charged colloids: Entropic lift and charge separation*. *EPL (Europhysics Letters)*, 65(5):719, 2004.
- [47] S. H. Behrens and D. G. Grier, *Pair interaction of charged colloidal spheres near a charged wall*. *Phys. Rev. E*, 64(5):050401, Oct. 2001.
- [48] C. P. Royall, M. E. Leunissen, and A. van Blaaderen, *A new colloidal model system to study long-range interactions quantitatively in real space*. *J. Phys.: Condens. Matter*, 15(48):S3581, 2003.
- [49] Z. W. Salsburg, R. W. Zwanzig, and J. G. Kirkwood, *Molecular Distribution Functions in a One-Dimensional Fluid*. *The Journal of Chemical Physics*, 21(6):1098–1107, June 1953.
- [50] R. L. Henderson, *A uniqueness theorem for fluid pair correlation functions*. *Physics Letters A*, 49(3):197–198, Sept. 1974.
- [51] A.-P. Hynninen, M. Dijkstra, and R. v. Roij, *Effect of triplet attractions on the phase diagram of suspensions of charged colloids*. *J. Phys.: Condens. Matter*, 15(48):S3549, 2003.
- [52] J.-P. Hansen and I. R. McDonald. *Theory of simple liquids: with applications to soft matter*. Academic Press, 2013.
- [53] A. D. Dinsmore, E. R. Weeks, V. Prasad, A. C. Levitt, and D. A. Weitz, *Three-dimensional confocal microscopy of colloids*. *Appl. Opt.*, AO, 40(24):4152–4159, Aug. 2001.
- [54] M. N. van der Linden, J. C. P. Stiefelhagen, G. Heessels-Gürboğa, J. E. S. van der Hoeven, N. A. Elbers, M. Dijkstra, and A. van Blaaderen, *Charging of Poly(methyl methacrylate) (PMMA) Colloids in Cyclohexyl Bromide: Locking, Size Dependence, and Particle Mixtures*. *Langmuir*, 31(1):65–75, Jan. 2015.
- [55] A. van Blaaderen and A. P. M. Kentgens, *Particle morphology and chemical microstructure of colloidal silica spheres made from alkoxyxilanes*. *Journal of Non-Crystalline Solids*, 149(3):161–178, Nov. 1992.
- [56] C. Graf, D. L. J. Vossen, A. Imhof, and A. van Blaaderen, *A General Method To Coat Colloidal Particles with Silica*. *Langmuir*, 19(17):6693–6700, Aug. 2003.
- [57] B. Liu, T. H. Besseling, M. Hermes, A. F. Demirörs, A. Imhof, and A. van Blaaderen, *Switching plastic crystals of colloidal rods with electric fields*. *Nature Communications*, 5, Jan. 2014.
- [58] B. Liu, T. H. Besseling, A. van Blaaderen, and A. Imhof, *Confinement Induced Plastic Crystal-to-Crystal Transitions in Rodlike Particles with Long-Range Repulsion*. *Phys. Rev. Lett.*, 115(7):078301, Aug. 2015.
- [59] R. D. Badley, W. T. Ford, F. J. McEnroe, and R. A. Assink, *Surface modification of colloidal silica*. *Langmuir*, 6(4):792–801, Apr. 1990.

- [60] G. H. Bogush, M. A. Tracy, and C. F. Zukoski, *Preparation of monodisperse silica particles: Control of size and mass fraction*. Journal of Non-Crystalline Solids, 104(1):95–106, Aug. 1988.
- [61] H. Giesche, *Synthesis of monodispersed silica powders I. Particle properties and reaction kinetics*. Journal of the European Ceramic Society, 14(3):189–204, Jan. 1994.
- [62] A. K. Van Helden, J. W. Jansen, and A. Vrij, *Preparation and characterization of spherical monodisperse silica dispersions in nonaqueous solvents*. Journal of Colloid and Interface Science, 81(2):354–368, June 1981.
- [63] J. C. Crocker and D. G. Grier, *Methods of Digital Video Microscopy for Colloidal Studies*. Journal of Colloid and Interface Science, 179(1):298–310, Apr. 1996.
- [64] *Particle tracking using IDL*. <http://www.physics.emory.edu/faculty/weeks/idl/index.html>. [Accessed Apr. 2017].
- [65] D. El Masri, T. Vissers, S. Badaire, J. C. P. Stiefelhagen, H. R. Vutukuri, P. Helfferich, T. H. Zhang, W. K. Kegel, A. Imhof, and A. van Blaaderen, *A qualitative confocal microscopy study on a range of colloidal processes by simulating microgravity conditions through slow rotations*. Soft Matter, 8(26):6979–6990, 2012.
- [66] T. Vissers, A. Imhof, F. Carrique, Á. V. Delgado, and A. van Blaaderen, *Electrophoresis of concentrated colloidal dispersions in low-polar solvents*. Journal of Colloid and Interface Science, 361(2):443–455, Sept. 2011.
- [67] H. E. Bakker, T. H. Besseling, J. E. G. J. Wijnhoven, P. H. Helfferich, A. van Blaaderen, and A. Imhof, *Microelectrophoresis of Silica Rods Using Confocal Microscopy*. Langmuir, 33(4):881–890, Jan. 2017.
- [68] M. E. Leunissen. *Manipulating Colloids with Charges & Electric Fields*. PhD, Utrecht University, Utrecht, 2007.
- [69] M. E. Leunissen, A. v. Blaaderen, A. D. Hollingsworth, M. T. Sullivan, and P. M. Chaikin, *Electrostatics at the oil–water interface, stability, and order in emulsions and colloids*. PNAS, 104(8):2585–2590, Feb. 2007.
- [70] M. T. Elsesser, A. D. Hollingsworth, K. V. Edmond, and D. J. Pine, *Large Core-Shell Poly(methyl methacrylate) Colloidal Clusters: Synthesis, Characterization, and Tracking*. Langmuir, 27(3):917–927, Feb. 2011.
- [71] A. F. Demirörs, D. Courty, R. Libanori, and A. R. Studart, *Periodically microstructured composite films made by electric- and magnetic-directed colloidal assembly*. PNAS, 113(17):4623–4628, Apr. 2016.
- [72] U. Dassanayake, S. Fraden, and A. van Blaaderen, *Structure of electrorheological fluids*. The Journal of Chemical Physics, 112(8):3851–3858, Feb. 2000.
- [73] J. N. Israelachvili. *Intermolecular and Surface Forces*. Academic Press, 2nd edition, Jan. 1992.
- [74] A. Labrosse and A. Burneau, *Characterization of porosity of ammonia catalysed alkoxysilane silica*. Journal of Non-Crystalline Solids, 221(2):107–124, Dec. 1997.

- [75] M. Szekeres, J. Tóth, and I. Dékány, *Specific Surface Area of Stoeber Silica Determined by Various Experimental Methods*. *Langmuir*, 18(7):2678–2685, Apr. 2002.
- [76] S. Li, Q. Wan, Z. Qin, Y. Fu, and Y. Gu, *Understanding Stöber Silica's Pore Characteristics Measured by Gas Adsorption*. *Langmuir*, 31(2):824–832, Jan. 2015.
- [77] M. E. Leunissen, J. Zwanikken, R. van Roij, P. M. Chaikin, and A. van Blaaderen, *Ion partitioning at the oil–water interface as a source of tunable electrostatic effects in emulsions with colloids*. *Physical Chemistry Chemical Physics*, 9(48):6405–6414, 2007.
- [78] N. A. Elbers, J. E. S. van der Hoeven, D. A. M. de Winter, C. T. W. M. Schneijdenberg, M. N. van der Linden, L. Filion, and A. van Blaaderen, *Repulsive van der Waals forces enable Pickering emulsions with non-touching colloids*. *Soft Matter*, 12(35):7265–7272, Aug. 2016.
- [79] A. Kuijk, A. van Blaaderen, and A. Imhof, *Synthesis of Monodisperse, Rodlike Silica Colloids with Tunable Aspect Ratio*. *J. Am. Chem. Soc.*, 133(8):2346–2349, Mar. 2011.
- [80] A. M. Wierenga, T. A. J. Lenstra, and A. P. Philipse, *Aqueous dispersions of colloidal gibbsite platelets: synthesis, characterisation and intrinsic viscosity measurements*. *Colloids and Surfaces A: Physicochemical and Engineering Aspects*, 134(3):359–371, Mar. 1998.
- [81] H. R. Vutukuri, S. Badaire, D. A. M. de Winter, A. Imhof, and A. van Blaaderen, *Directed Self-Assembly of Micron-Sized Gold Nanoplatelets into Oriented Flexible Stacks with Tunable Interplate Distance*. *Nano Lett.*, 15(8):5617–5623, Aug. 2015.
- [82] T. Sugimoto, M. M. Khan, and A. Muramatsu, *Preparation of monodisperse peanut-type  $\alpha$ -Fe<sub>2</sub>O<sub>3</sub> particles from condensed ferric hydroxide gel*. *Colloids and Surfaces A: Physicochemical and Engineering Aspects*, 70(2):167–169, Mar. 1993.
- [83] L. Rossi, S. Sacanna, W. T. M. Irvine, P. M. Chaikin, D. J. Pine, and A. P. Philipse, *Cubic crystals from cubic colloids*. *Soft Matter*, 7(9):4139–4142, Apr. 2011.
- [84] H. R. Vutukuri, F. Smallenburg, S. Badaire, A. Imhof, M. Dijkstra, and A. van Blaaderen, *An experimental and simulation study on the self-assembly of colloidal cubes in external electric fields*. *Soft Matter*, 10(45):9110–9119, 2014.
- [85] L. Scarabelli, M. Coronado-Puchau, J. J. Giner-Casares, J. Langer, and L. M. Liz-Marzán, *Monodisperse Gold Nanotriangles: Size Control, Large-Scale Self-Assembly, and Performance in Surface-Enhanced Raman Scattering*. *ACS Nano*, 8(6):5833–5842, June 2014.
- [86] C. J. DeSantis and S. E. Skrabalak, *Size-Controlled Synthesis of Au/Pd Octopods with High Refractive Index Sensitivity*. *Langmuir*, 28(24):9055–9062, June 2012.
- [87] M. P. Arciniegas, M. R. Kim, J. de Graaf, R. Brescia, S. Marras, K. Miszta, M. Dijkstra, R. van Roij, and L. Manna, *Self-Assembly of Octapod-Shaped Colloidal Nanocrystals into a Hexagonal Ballerina Network Embedded in a Thin Polymer Film*. *Nano Lett.*, 14(2):1056–1063, Feb. 2014.

- [88] M. Corricelli, N. Depalo, E. D. Carlo, E. Fanizza, V. Laquintana, N. Denora, A. Agostiano, M. Striccoli, and M. L. Curri, *Biotin-decorated silica coated PbS nanocrystals emitting in the second biological near infrared window for bioimaging*. *Nanoscale*, 6(14):7924–7933, June 2014.
- [89] I. E. Sendroui, M. E. Warner, and R. M. Corn, *Fabrication of Silica-Coated Gold Nanorods Functionalized with DNA for Enhanced Surface Plasmon Resonance Imaging Biosensing Applications*. *Langmuir*, 25(19):11282–11284, Oct. 2009.
- [90] R. Purbia and S. Paria, *Yolk/shell nanoparticles: classifications, synthesis, properties, and applications*. *Nanoscale*, 7(47):19789–19873, Nov. 2015.
- [91] D. Nagao, C. M. van Kats, K. Hayasaka, M. Sugimoto, M. Konno, A. Imhof, and A. van Blaaderen, *Synthesis of Hollow Asymmetrical Silica Dumbbells with a Movable Inner Core*. *Langmuir*, 26(7):5208–5212, Apr. 2010.
- [92] B. Liu, W. Zhang, H. Feng, and X. Yang, *Rattle-type microspheres as a support of tiny gold nanoparticles for highly efficient catalysis*. *Chem. Commun.*, 47(42):11727–11729, Oct. 2011.
- [93] M. Priebe and K. M. Fromm, *Nanorattles or Yolk–Shell Nanoparticles—What Are They, How Are They Made, and What Are They Good For?* *Chem. Eur. J.*, 21(10):3854–3874, Mar. 2015.
- [94] M. Roca and A. J. Haes, *Silica-Void-Gold Nanoparticles: Temporally Stable Surface-Enhanced Raman Scattering Substrates*. *J. Am. Chem. Soc.*, 130(43):14273–14279, Oct. 2008.
- [95] L. Zhang, T. Wang, L. Yang, C. Liu, C. Wang, H. Liu, Y. A. Wang, and Z. Su, *General Route to Multifunctional Uniform Yolk/Mesoporous Silica Shell Nanocapsules: A Platform for Simultaneous Cancer-Targeted Imaging and Magnetically Guided Drug Delivery*. *Chem. Eur. J.*, 18(39):12512–12521, Sept. 2012.
- [96] P. Du and P. Liu, *Novel Smart Yolk/Shell Polymer Microspheres as a Multiply Responsive Cargo Delivery System*. *Langmuir*, 30(11):3060–3068, Mar. 2014.
- [97] J. Liu, S. Zhang Qiao, J. Song Chen, X. W. D. Lou, X. Xing, and G. Q. M. Lu, *Yolk/shell nanoparticles : new platforms for nanoreactors, drug delivery and lithium-ion batteries*. *Chemical Communications*, 47(47):12578–12591, 2011.
- [98] B. K. Shrestha and A. J. Haes, *Improving surface enhanced Raman signal reproducibility using gold-coated silver nanospheres encapsulated in silica membranes*. *J. Opt.*, 17(11):114017, 2015.
- [99] G. Lu, B. Shrestha, and A. J. Haes, *Importance of Tilt Angles of Adsorbed Aromatic Molecules on Nanoparticle Rattle SERS Substrates*. *J. Phys. Chem. C*, 120(37):20759–20767, Sept. 2016.
- [100] K. Watanabe, D. Nagao, H. Ishii, and M. Konno, *Rattle-Type Colloidal Crystals Composed of Spherical Hollow Particles Containing an Anisotropic, Movable Core*. *Langmuir*, 31(19):5306–5310, May 2015.
- [101] D. Chen, L. Li, F. Tang, and S. Qi, *Facile and Scalable Synthesis of Tailored Silica “Nanorattle” Structures*. *Adv. Mater.*, 21(37):3804–3807, Oct. 2009.

- [102] Y. Chen, H.-R. Chen, and J.-L. Shi, *Construction of Homogeneous/Heterogeneous Hollow Mesoporous Silica Nanostructures by Silica-Etching Chemistry: Principles, Synthesis, and Applications*. Acc. Chem. Res., 47(1):125–137, Jan. 2014.
- [103] A. Mohamed El-Toni, A. Khan, M. Abbas Ibrahim, J. Puzon Labis, G. Badr, M. Al-Hoshan, S. Yin, and T. Sato, *Synthesis of double mesoporous core-shell silica spheres with tunable core porosity and their drug release and cancer cell apoptosis properties*. Journal of Colloid and Interface Science, 378(1):83–92, July 2012.
- [104] Q. Yu, P. Wang, S. Hu, J. Hui, J. Zhuang, and X. Wang, *Hydrothermal Synthesis of Hollow Silica Spheres under Acidic Conditions*. Langmuir, 27(11):7185–7191, June 2011.
- [105] T. Zhang, J. Ge, Y. Hu, Q. Zhang, S. Aloni, and Y. Yin, *Formation of Hollow Silica Colloids through a Spontaneous Dissolution-Regrowth Process*. Angewandte Chemie International Edition, 47(31):5806–5811, July 2008.
- [106] Y. Hu, Q. Zhang, J. Goebel, T. Zhang, and Y. Yin, *Control over the permeation of silica nanoshells by surface-protected etching with water*. Phys. Chem. Chem. Phys., 12(38):11836–11842, Sept. 2010.
- [107] X. Wu, L. Tan, D. Chen, X. He, H. Liu, X. Meng, and F. Tang, *Alkylaminosilane-Assisted Simultaneous Etching and Growth Route to Synthesis Metal Nanoparticles Encapsulated by Silica Nanorattles*. Chem. Eur. J., 18(49):15669–15675, Dec. 2012.
- [108] X.-J. Wu and D. Xu, *Soft Template Synthesis of Yolk/Silica Shell particles*. Adv. Mater., 22(13):1516–1520, Apr. 2010.
- [109] A.-P. Hynninen, C. G. Christova, R. van Roij, A. van Blaaderen, and M. Dijkstra, *Prediction and Observation of Crystal Structures of Oppositely Charged Colloids*. Phys. Rev. Lett., 96(13):138308, Apr. 2006.
- [110] J. Paul, S. Romeis, M. Mačković, V. R. R. Marthala, P. Herre, T. Przybilla, M. Hartmann, E. Spiecker, J. Schmidt, and W. Peukert, *In situ cracking of silica beads in the SEM and TEM — Effect of particle size on structure-property correlations*. Powder Technology, 270:337–347, Jan. 2015.
- [111] Y. J. Wong, L. Zhu, W. S. Teo, Y. W. Tan, Y. Yang, C. Wang, and H. Chen, *Revisiting the Stöber Method: Inhomogeneity in Silica Shells*. J. Am. Chem. Soc., 133(30):11422–11425, Aug. 2011.
- [112] F. García-Santamaría, H. Míguez, M. Ibisate, F. Meseguer, and C. López, *Refractive Index Properties of Calcined Silica Submicrometer Spheres*. Langmuir, 18(5):1942–1944, Mar. 2002.
- [113] H. Míguez, F. Meseguer, C. López, Á. Blanco, J. S. Moya, J. Requena, A. Mifsud, and V. Fornés, *Control of the Photonic Crystal Properties of fcc-Packed Submicrometer SiO<sub>2</sub> Spheres by Sintering*. Adv. Mater., 10(6):480–483, Apr. 1998.
- [114] C.-M. Ho and Y.-C. Tai, *Micro-electro-mechanical-systems (mems) and fluid flows*. Annu. Rev. Fluid Mech., 30(1):579–612, Jan. 1998.
- [115] J. M. Bustillo, R. T. Howe, and R. S. Muller, *Surface Micromachining for Microelectromechanical Systems*. Proc. IEEE, 86(8):1552–1574, Aug. 1998.

- 
- [116] G. A. C. M. Spierings, *Wet chemical etching of silicate glasses in hydrofluoric acid based solutions*. J Mater Sci, 28(23):6261–6273, 1993.
- [117] D. J. Monk, D. S. Soane, and R. T. Howe, *A review of the chemical reaction mechanism and kinetics for hydrofluoric acid etching of silicon dioxide for surface micromachining applications*. Thin Solid Films, 232(1):1–12, Sept. 1993.
- [118] N. A. M. Verhaegh and A. van Blaaderen, *Dispersions of Rhodamine-Labeled Silica Spheres: Synthesis, Characterization, and Fluorescence Confocal Scanning Laser Microscopy*. Langmuir, 10(5):1427–1438, May 1994.
- [119] A. van Blaaderen and A. Vrij, *Synthesis and Characterization of Monodisperse Colloidal Organo-silica Spheres*. Journal of Colloid and Interface Science, 156(1):1–18, Mar. 1993.
- [120] K. Nozawa, H. Gailhanou, L. Raison, P. Panizza, H. Ushiki, E. Sellier, J. P. Delville, and M. H. Delville, *Smart Control of Monodisperse Stöber Silica Particles: Effect of Reactant Addition Rate on Growth Process*. Langmuir, 21(4):1516–1523, Feb. 2005.
- [121] A. P. Philipse and A. Vrij, *Preparation and properties of nonaqueous model dispersions of chemically modified, charged silica spheres*. Journal of Colloid and Interface Science, 128(1):121–136, Mar. 1989.
- [122] P. M. Johnson, C. M. van Kats, and A. van Blaaderen, *Synthesis of Colloidal Silica Dumbbells*. Langmuir, 21(24):11510–11517, Nov. 2005.
- [123] A. A. Volkert, M. C. S. Pierre, B. Shrestha, and A. J. Haes, *Implications of sample aging on the formation of internally etched silica coated gold nanoparticles*. RSC Adv., 5(5):3774–3780, Dec. 2014.
- [124] L. Zhang, M. D’Acunzi, M. Kappl, G. K. Auernhammer, D. Vollmer, C. M. van Kats, and A. van Blaaderen, *Hollow Silica Spheres: Synthesis and Mechanical Properties*. Langmuir, 25(5):2711–2717, Mar. 2009.
- [125] M. Mačković, F. Niekietel, L. Wondraczek, and E. Spiecker, *Direct observation of electron-beam-induced densification and hardening of silica nanoballs by in situ transmission electron microscopy and finite element method simulations*. Acta Materialia, 79:363–373, Oct. 2014.
- [126] J. Yi, H. S. Jang, J. S. Lee, and W. I. Park, *Bioinspired Morphogenesis of Highly Intricate and Symmetric Silica Nanostructures*. Nano Lett., 12(7):3743–3748, July 2012.
- [127] R. Gunn, *Diffusion charging of atmospheric droplets by ions, and the resulting combination coefficients*. J. Meteor., 11(5):339–347, Oct. 1954.
- [128] H. Brenner, *The slow motion of a sphere through a viscous fluid towards a plane surface*. Chemical Engineering Science, 16(3):242–251, Dec. 1961.
- [129] F. Roosen-Runge, M. Hennig, F. Zhang, R. M. J. Jacobs, M. Sztucki, H. Schober, T. Seydel, and F. Schreiber, *Protein self-diffusion in crowded solutions*. PNAS, 108(29):11815–11820, July 2011.
- [130] B. ten Hagen, S. van Teeffelen, and H. Löwen, *Brownian motion of a self-propelled particle*. J. Phys.: Condens. Matter, 23(19):194119, 2011.
- [131] D. C. Prieve, *Measurement of colloidal forces with TIRM*. Advances in Colloid and Interface Science, 82(1–3):93–125, Oct. 1999.

- [132] L. Lobry and N. Ostrowsky, *Diffusion of Brownian particles trapped between two walls: Theory and dynamic-light-scattering measurements*. Phys. Rev. B, 53(18):12050–12056, May 1996.
- [133] B. Cichocki and R. B. Jones, *Image representation of a spherical particle near a hard wall*. Physica A: Statistical Mechanics and its Applications, 258(3):273–302, Sept. 1998.
- [134] S. Chandrasekhar, *Stochastic Problems in Physics and Astronomy*. Rev. Mod. Phys., 15(1):1–89, Jan. 1943.
- [135] J. I. Jiménez-Aquino, R. M. Velasco, and F. J. Uribe, *Brownian motion of a classical harmonic oscillator in a magnetic field*. Phys. Rev. E, 77(5):051105, May 2008.
- [136] K. Watanabe, H. Ishii, M. Konno, A. Imhof, A. van Blaaderen, and D. Nagao, *Yolk/Shell Colloidal Crystals Incorporating Movable Cores with Their Motion Controlled by an External Electric Field*. Langmuir, 33(1):296–302, Jan. 2017.
- [137] J. C. Crocker, *Measurement of the hydrodynamic corrections to the Brownian motion of two colloidal spheres*. The Journal of Chemical Physics, 106(7):2837–2840, Feb. 1997.
- [138] G. A. Schumacher and T. G. M. van de Ven, *Brownian motion of charged colloidal particles surrounded by electric double layers*. Faraday Discuss. Chem. Soc., 83(0):75–85, Jan. 1987.
- [139] F. Strubbe, F. Beunis, T. Brans, M. Karvar, W. Woestenborghs, and K. Neyts, *Electrophoretic Retardation of Colloidal Particles in Nonpolar Liquids*. Phys. Rev. X, 3(2):021001, Apr. 2013.
- [140] P. Holmqvist, J. K. G. Dhont, and P. R. Lang, *Anisotropy of Brownian motion caused only by hydrodynamic interaction with a wall*. Phys. Rev. E, 74(2):021402, Aug. 2006.
- [141] A. J. Goldman, R. G. Cox, and H. Brenner, *Slow viscous motion of a sphere parallel to a plane wall—I Motion through a quiescent fluid*. Chemical Engineering Science, 22(4):637–651, Apr. 1967.
- [142] M. Lisicki, B. Cichocki, S. A. Rogers, J. K. G. Dhont, and P. R. Lang, *Translational and rotational near-wall diffusion of spherical colloids studied by evanescent wave scattering*. Soft Matter, 10(24):4312–4323, May 2014.
- [143] E. R. Dufresne, D. Altman, and D. G. Grier, *Brownian dynamics of a sphere between parallel walls*. Europhys. Lett., 53(2):264–270, Jan. 2001.
- [144] S. Delong, F. B. Usabiaga, R. Delgado-Buscalioni, B. E. Griffith, and A. Donev, *Brownian dynamics without Green’s functions*. The Journal of Chemical Physics, 140(13):134110, Apr. 2014.
- [145] S. L. Dettmer, S. Pagliara, K. Misiunas, and U. F. Keyser, *Anisotropic diffusion of spherical particles in closely confining microchannels*. Phys. Rev. E, 89(6):062305, June 2014.
- [146] S. L. Eichmann, S. G. Anekal, and M. A. Bevan, *Electrostatically Confined Nanoparticle Interactions and Dynamics*. Langmuir, 24(3):714–721, Feb. 2008.

- [147] A. E. Cervantes-Martínez, A. Ramírez-Saito, R. Armenta-Calderón, M. A. Ojeda-López, and J. L. Arauz-Lara, *Colloidal diffusion inside a spherical cell*. Phys. Rev. E, 83(3):030402, Mar. 2011.
- [148] F. Feuillebois and A. Sellier, editors. *Theoretical Methods for Micro Scales Viscous Flows*. Transworld Research Network, 2009. Google-Books-ID: y4taygAACAAJ.
- [149] C. Aponte-Rivera and R. N. Zia, *Simulation of hydrodynamically interacting particles confined by a spherical cavity*. Phys. Rev. Fluids, 1(2):023301, June 2016.
- [150] A. Imperio, J. T. Padding, and W. J. Briels, *Diffusion of spherical particles in microcavities*. The Journal of Chemical Physics, 134(15):154904, Apr. 2011.
- [151] H. B. Eral, J. M. Oh, D. van den Ende, F. Mugele, and M. H. G. Duits, *Anisotropic and Hindered Diffusion of Colloidal Particles in a Closed Cylinder*. Langmuir, 26(22):16722–16729, Nov. 2010.
- [152] P. Walden, *Organic solutions- and ionisation means. III. Chapter: Internal friction and its connection with conductivity*. Zeitschrift Fur Physikalische Chemie–Stoichiometrie Und Verwandtschaftslehre, 55(2):207–249, Apr. 1906. WOS:000201330700003.
- [153] C. Schreiner, S. Zugmann, R. Hartl, and H. J. Gores, *Fractional Walden Rule for Ionic Liquids: Examples from Recent Measurements and a Critique of the So-Called Ideal KCl Line for the Walden Plot*. J. Chem. Eng. Data, 55(5):1784–1788, May 2010.
- [154] A. Benouar, M. Kameche, and M. A. Bouhlala, *Molar conductivities of concentrated lithium chloride–glycerol solutions at low and high temperatures: application of a quasi-lattice model*. Physics and Chemistry of Liquids, 54(1):62–73, Jan. 2016.
- [155] N.-S. Cheng, *Formula for the Viscosity of a Glycerol-Water Mixture*. Ind. Eng. Chem. Res., 47(9):3285–3288, May 2008.
- [156] *Calculate density and viscosity of glycerol/water mixtures*. [http://www.met.reading.ac.uk/~sws04cdw/viscosity\\_calc.html](http://www.met.reading.ac.uk/~sws04cdw/viscosity_calc.html). [Accessed Apr. 2017].
- [157] P. J. Lu, M. Shutman, E. Sloutskin, and A. V. Butenko, *Locating particles accurately in microscope images requires image-processing kernels to be rotationally symmetric*. Opt. Express, OE, 21(25):30755–30763, Dec. 2013.
- [158] J. Clayden. *Organic chemistry*. Oxford Oxford University Press, 2001.
- [159] M. W. Rutland and R. M. Pashley, *The charging properties of monodisperse colloidal silica in symmetrical quaternary ammonium ion solutions*. Journal of Colloid and Interface Science, 130(2):448–456, July 1989.
- [160] P. Mazur and U. Geigenmüller, *A simple formula for the short-time self-diffusion coefficient in concentrated suspensions*. Physica A: Statistical Mechanics and its Applications, 146(3):657–661, Dec. 1987.
- [161] S. Thiberge, A. Nechushtan, D. Sprinzak, O. Gileadi, V. Behar, O. Zik, Y. Chowers, S. Michaeli, J. Schlessinger, and E. Moses, *Scanning electron microscopy of cells and tissues under fully hydrated conditions*. PNAS, 101(10):3346–3351, Mar. 2004.

- [162] T. J. Woehl, J. E. Evans, I. Arslan, W. D. Ristenpart, and N. D. Browning, *Direct in Situ Determination of the Mechanisms Controlling Nanoparticle Nucleation and Growth*. ACS Nano, 6(10):8599–8610, Oct. 2012.
- [163] H. Zheng, R. K. Smith, Y.-w. Jun, C. Kisielowski, U. Dahmen, and A. P. Alivisatos, *Observation of Single Colloidal Platinum Nanocrystal Growth Trajectories*. Science, 324(5932):1309–1312, June 2009.
- [164] T. Kraus and N. de Jonge, *Dendritic Gold Nanowire Growth Observed in Liquid with Transmission Electron Microscopy*. Langmuir, 29(26):8427–8432, July 2013.
- [165] F. Wu and N. Yao, *Advances in sealed liquid cells for in-situ TEM electrochemical investigation of lithium-ion battery*. Nano Energy, 11:196–210, Jan. 2015.
- [166] B. W. Smith and D. E. Luzzi, *Electron irradiation effects in single wall carbon nanotubes*. Journal of Applied Physics, 90(7):3509–3515, Sept. 2001.
- [167] J. C. Meyer, F. Eder, S. Kurasch, V. Skakalova, J. Kotakoski, H. J. Park, S. Roth, A. Chuvilin, S. Eychen, G. Benner, A. V. Krasheninikov, and U. Kaiser, *Accurate Measurement of Electron Beam Induced Displacement Cross Sections for Single-Layer Graphene*. Phys. Rev. Lett., 108(19):196102, May 2012.
- [168] C. P. Royall, B. L. Thiel, and A. M. Donald, *Radiation damage of water in environmental scanning electron microscopy*. Journal of Microscopy, 204(3):185–195, Dec. 2001.
- [169] E. U. Donev and J. T. Hastings, *Electron-Beam-Induced Deposition of Platinum from a Liquid Precursor*. Nano Lett., 9(7):2715–2718, July 2009.
- [170] T. Delclos, C. Aimé, E. Pouget, A. Brizard, I. Huc, M.-H. Delville, and R. Oda, *Individualized Silica Nanohelices and Nanotubes: Tuning Inorganic Nanostructures Using Lipidic Self-Assemblies*. Nano Lett., 8(7):1929–1935, July 2008.
- [171] G. B. Alexander, W. M. Heston, and R. K. Iler, *The Solubility of Amorphous Silica in Water*. J. Phys. Chem., 58(6):453–455, June 1954.
- [172] P. A. Bazuła, P. M. Arnal, C. Galeano, B. Zibrowius, W. Schmidt, and F. Schüth, *Highly microporous monodisperse silica spheres synthesized by the Stöber process*. Microporous and Mesoporous Materials, 200:317–325, Dec. 2014.
- [173] S. Romeis, J. Paul, M. Hanisch, V. R. R. Marthala, M. Hartmann, R. N. K. Taylor, J. Schmidt, and W. Peukert, *Correlation of Enhanced Strength and Internal Structure for Heat-Treated Submicron Stöber Silica Particles*. Part. Part. Syst. Charact., 31(6):664–674, June 2014.
- [174] L. Zhang, M. D’Acunzi, M. Kappl, A. Imhof, A. van Blaaderen, H.-J. Butt, R. Graf, and D. Vollmer, *Tuning the mechanical properties of silica microcapsules*. Physical Chemistry Chemical Physics, 12(47):15392–15398, 2010.
- [175] K. Zheng, C. Wang, Y.-Q. Cheng, Y. Yue, X. Han, Z. Zhang, Z. Shan, S. X. Mao, M. Ye, Y. Yin, and E. Ma, *Electron-beam-assisted superplastic shaping of nanoscale amorphous silica*. Nature Communications, 1:ncomms1021, June 2010.

- [176] T. van Dillen, A. Polman, C. M. van Kats, and A. van Blaaderen, *Ion beam-induced anisotropic plastic deformation at 300 keV*. Appl. Phys. Lett., 83(21):4315–4317, Nov. 2003.
- [177] J. Zečević, K. P. de Jong, and N. de Jonge, *Manipulating Size and Shape of Silica Nanoparticles with Liquid-Phase Transmission Electron Microscopy*. Microscopy and Microanalysis, 21(S3):1129–1130, Aug. 2015.
- [178] M. W. P. van de Put, C. C. M. C. Carcouët, P. H. H. Bomans, H. Friedrich, N. de Jonge, and N. A. J. M. Sommerdijk, *Writing Silica Structures in Liquid with Scanning Transmission Electron Microscopy*. Small, 11(5):585–590, Feb. 2015.
- [179] J. Zečević, J. Hermannsdörfer, T. Schuh, K. P. de Jong, and N. de Jonge, *Anisotropic Shape Changes of Silica Nanoparticles Induced in Liquid with Scanning Transmission Electron Microscopy*. Small, 13(1):n/a–n/a, Jan. 2017.
- [180] S. W. Chee, Z. Baraissov, N. D. Loh, P. T. Matsudaira, and U. Mirsaidov, *Desorption-Mediated Motion of Nanoparticles at the Liquid–Solid Interface*. J. Phys. Chem. C, 120(36):20462–20470, Sept. 2016.
- [181] D. Koziej, A. Lauria, and M. Niederberger, *25th Anniversary Article: Metal Oxide Particles in Materials Science: Addressing All Length Scales*. Adv. Mater., 26(2):235–257, Jan. 2014.
- [182] C. A. Cadigan, A. R. Corpuz, F. Lin, C. M. Caskey, K. B. H. Finch, X. Wang, and R. M. Richards, *Nanoscale (111) faceted rock-salt metal oxides in catalysis*. Catal. Sci. Technol., 3(4):900–911, Mar. 2013.
- [183] G. E. Brown, V. E. Henrich, W. H. Casey, D. L. Clark, C. Eggleston, A. Felmy, D. W. Goodman, M. Grätzel, G. Maciel, M. I. McCarthy, K. H. Nealson, D. A. Sverjensky, M. F. Toney, and J. M. Zachara, *Metal Oxide Surfaces and Their Interactions with Aqueous Solutions and Microbial Organisms*. Chem. Rev., 99(1):77–174, Jan. 1999.
- [184] G. E. Brown, *How Minerals React with Water*. Science, 294(5540):67–69, Oct. 2001.
- [185] G. A. Waychunas, C. S. Kim, and J. F. Banfield, *Nanoparticulate Iron Oxide Minerals in Soils and Sediments: Unique Properties and Contaminant Scavenging Mechanisms*. J Nanopart Res, 7(4-5):409–433, Oct. 2005.
- [186] A. M. Ruminski, K.-J. Jeon, and J. J. Urban, *Size-dependent CO<sub>2</sub> capture in chemically synthesized magnesium oxide nanocrystals*. J. Mater. Chem., 21(31):11486–11491, July 2011.
- [187] G. C. Kennedy, *The brucite-periclase equilibrium*. Am J Sci, 254(9):567–573, Sept. 1956.
- [188] J. A. Schramke, D. M. Kerrick, and J. G. Blencoe, *Experimental determination of the brucite = periclase + water equilibrium with a new volumetric technique*. American Mineralogist, 67(3-4):269–276, 1982.
- [189] S. Guillot and K. Hattori, *Serpentinites: Essential Roles in Geodynamics, Arc Volcanism, Sustainable Development, and the Origin of Life*. Elements, 9(2):95–98, Apr. 2013.
- [190] O. Plümpfer, A. Røyne, A. Magrasó, and B. Jamtveit, *The interface-scale mechanism of reaction-induced fracturing during serpentization*. Geology, 40(12):1103–1106, Dec. 2012.

- [191] R. Hacquart and J. Jupille, *Hydrated MgO smoke crystals from cubes to octahedra*. Chemical Physics Letters, 439(1–3):91–94, May 2007.
- [192] P. Geysersmans, F. Finocchi, J. Goniakowski, R. Hacquart, and J. Jupille, *Combination of (100), (110) and (111) facets in MgO crystals shapes from dry to wet environment*. Phys. Chem. Chem. Phys., 11(13):2228–2233, Mar. 2009.
- [193] N. H. de Leeuw, G. W. Watson, and S. C. Parker, *Atomistic Simulation of the Effect of Dissociative Adsorption of Water on the Surface Structure and Stability of Calcium and Magnesium Oxide*. J. Phys. Chem., 99(47):17219–17225, Nov. 1995.
- [194] R. Hacquart and J. Jupille, *Morphology of MgO smoke crystallites upon etching in wet environment*. Journal of Crystal Growth, 311(21):4598–4604, Oct. 2009.
- [195] S. O. Baumann, J. Schneider, A. Sternig, D. Thomele, S. Stankic, T. Berger, H. Grönbeck, and O. Diwald, *Size Effects in MgO Cube Dissolution*. Langmuir, 31(9):2770–2776, Mar. 2015.
- [196] A. Fedoročková and P. Raschman, *Effects of pH and acid anions on the dissolution kinetics of MgO*. Chemical Engineering Journal, 143(1–3):265–272, Sept. 2008.
- [197] G. Yamaguchi and T. Tokuda, *Electron Microscopic Study of the Dehydration of Brucite and the Recrystallization of Periclase upon Further Heating*. Bulletin of the Chemical Society of Japan, 37(3):399–403, 1964.
- [198] J. F. Goodman, *The Decomposition of Magnesium Hydroxide in an Electron Microscope*. Proceedings of the Royal Society of London. Series A, Mathematical and Physical Sciences, 247(1250):346–352, Sept. 1958.
- [199] U. Dahmen, M. G. Kim, and A. W. Searcy, *Microstructural evolution during the decomposition of Mg(OH)<sub>2</sub>*. Ultramicroscopy, 23(3–4):365–370, 1987.
- [200] K. Refson, R. A. Wogelius, D. G. Fraser, M. C. Payne, M. H. Lee, and V. Milman, *Water chemisorption and reconstruction of the MgO surface*. Phys. Rev. B, 52(15):10823–10826, Oct. 1995.
- [201] R. A. Wogelius, K. Refson, D. G. Fraser, G. W. Grime, and J. P. Goff, *Periclase surface hydroxylation during dissolution*. Geochimica et Cosmochimica Acta, 59(9):1875–1881, May 1995.
- [202] P. A. van Aken and F. Langenhorst, *Nanocrystalline, porous periclase aggregates as product of brucite dehydration*. European Journal of Mineralogy, 13(2):329–341, Apr. 2001.
- [203] A. V. G. Chizmeshya, M. J. McKelvy, R. Sharma, R. W. Carpenter, and H. Bearat, *Density functional theory study of the decomposition of Mg(OH)<sub>2</sub>: a lamellar dehydroxylation model*. Materials Chemistry and Physics, 77(2):416–425, Jan. 2003.
- [204] K. Jug, B. Heidberg, and T. Bredow, *Cyclic Cluster Study on the Formation of Brucite from Periclase and Water*. J. Phys. Chem. C, 111(35):13103–13108, Sept. 2007.

- 
- [205] M. J. McKelvy, R. Sharma, A. V. G. Chizmeshya, R. W. Carpenter, and K. Streib, *Magnesium Hydroxide Dehydroxylation: In Situ Nanoscale Observations of Lamellar Nucleation and Growth*. *Chem. Mater.*, 13(3):921–926, Mar. 2001.
- [206] M. Gajdardziska-Josifovska and R. Sharma, *Interaction of oxide surfaces with water: environmental transmission electron microscopy of MgO hydroxylation*. *Microsc. Microanal.*, 11(6):524–533, Dec. 2005.
- [207] *WebEMAPS*. <http://emaps.mrl.uiuc.edu/>, Oct. 2015. [Accessed Oct. 2015].
- [208] J. T. Newberg, D. E. Starr, S. Yamamoto, S. Kaya, T. Kendelewicz, E. R. Mysak, S. Porsgaard, M. B. Salmeron, G. E. Brown, A. Nilsson, and H. Bluhm, *Autocatalytic Surface Hydroxylation of MgO(100) Terrace Sites Observed under Ambient Conditions*. *J. Phys. Chem. C*, 115(26):12864–12872, July 2011.
- [209] S. J. Zinkle and C. Kinoshita, *Defect production in ceramics*. *Journal of Nuclear Materials*, 251:200–217, Nov. 1997.
- [210] D. B. Williams and C. B. Carter. *Transmission Electron Microscopy*. Springer US, Boston, MA, 2009.



---

# Summary

---

For the work described in this thesis, we synthesized and studied collections of colloidal particles and analyzed single particle dynamics. Particles with typical sizes in the nanometer ( $10^{-9}$  m) range up to (approximately) a micrometer ( $10^{-6}$  m) are considered ‘colloidal.’ In this range, thermal fluctuations are sufficient to perturb particles and their collective arrangements and are thereby sufficient to nudge them towards equilibrium. By using *confocal laser scanning microscopy*, particle positions, motions and interparticle distances were obtained. We extracted particle properties and calculated interparticle interactions from the (collective) behavior of these particles. Additionally, we used *electron microscopy* to study colloidal particles, which offered far superior resolution. Recently, it has become possible to also observe dispersions of particles (in *liquids*) in the electron microscope, whereas before, examination was restricted to dry samples. However, the electron beam used to form the images is not innocent like the beam of light in optical microscopy and liquid samples often exhibit unpredicted behavior caused by the high-energy electrons.

In **chapter 2**, the synthesis of (fluorescently labeled) silica spheres is described along with a new method to transfer these particles to the low-polar solvent cyclohexyl chloride (CHC). This method utilized another solvent, trimethylolpropane ethoxylate triacrylate (ETPTA), which can be deionized and which does not decompose into ions when sonicated. Additionally, ETPTA is a convenient solvent because it can be polymerized using a photo-initiator and UV light, thereby instantaneously immobilizing a large volume of particle dispersion. Moreover, this new method to transfer particles to CHC did not require the particles to be covered with a hydrophobic coating. The particle (zeta) potential was measured in several different ways for various volume fractions and was found to be independent of volume fraction. However, the particle charge reduced considerably after the particles had been stored (in ethanol) for 35 months. This experimental system is a step towards a dispersion of long range repulsive fluorescent silica nanoparticles that can be arrested using UV light, allowing direct measurement of the interparticle potential of nanoparticles.

The synthesis of silica particles was continued - and modified - in **chapter 3**. By incorporating a silane coupling agent (SCA), N-[3-(trimethoxysilyl)propyl]ethylenediamine (EDAPTMS), during the growth reaction, a

different type of silica was synthesized. Such organically modified silica ('ormosil') has been found to be more sensitive to hydrofluoric acid (HF) etching, allowing it to be removed more quickly than regular 'pure' silica. However, ormosil and pure silica were found to etch at nearly the same rate in NaOH solution. In order to maximize the difference in HF etching sensitivity between regular and doped silica, the SCA content was optimized allowing up to 25 mol% to be incorporated. By synthesizing particles containing an ormosil layer in between a pure silica core and outer shell and subsequently etching with HF solution, the ormosil layer could be removed leaving fluorescently labeled pure silica 'yolk-shell' particles: a small dyed particle inside a large shell with a void space in between. Unlike methods that remove the layer with a thermal treatment, removal of the ormosil layer with HF left fluorescent dyes intact. The removal of the ormosil layer by HF etching was found to occur through two etching pathways: it was either removed homogeneously from all sides through the shell, or from a single point/line. Additionally, dumbbell particles were found to be more sensitive to HF etching than single spherical particles. This was attributed to a thinner/weaker outer silica shell in the neck region in the middle of the dumbbells. These observations indicate that the structure of the outer silica shell varied considerably between particles and was crucial for determining its etching behavior.

Besides the different etching sensitivities, doped and pure silica also differed in their charge. Under neutral conditions, pure silica was negatively charged due to its silanol groups. However, because of the amine groups of the incorporated SCA the ormosil silica was positively charged. Coating a pure silica particle with only a few nanometers of ormosil was sufficient to reverse the particle potential from  $-80$  to  $+58$  mV. Mild HF etching of particles that contained an ormosil layer, allowed the net particle charge to be gradually tuned from negative to positive. The ormosil layer was likely made more accessible by the mild HF etching, thus allowing it to acquire more charge and gradually alter the particle potential. This reversal of the particle charge completed before morphological changes occurred.

The particles synthesized in chapter 3 were used in **chapter 4** to study the diffusion of a particle confined by a spherical shell. The fluorescent core particles were imaged at various salt concentrations using confocal laser scanning microscopy and the images were analyzed using particle tracking computer code. The motion of the core particle was found to have slowed down more strongly than expected based purely on hydrodynamic coupling with the shell. This was likely related to the additional electrostatic repulsion which also affected particle motion. Moreover, the range of the electrostatic repulsion was found to be stronger than expected for all salt concentrations. Surprisingly, the diffusivity of the particle did not change with particle-wall separation.

In **chapter 5**, a dispersion of silica yolk-shell particles in water was imaged using *Scanning Transmission Electron Microscopy* (STEM). Prior to the measurements, the particles were fully condensed to  $\text{SiO}_2$  by heating

to 900 °C. When dispersed in liquid water, the particles were drastically affected by the electron beam. Exposure to the e-beam initially resulted in an increase in particle diameter by 10%, followed by gradual and sustained shrinkage. This occurred for both the core and the shell, although the transformation of the shell occurred more quickly. Identical particles of a lower material density - having only been heated to 500 °C - demonstrated a swelling of only 2-3% before shrinking, indicating that the initial increase in particle size was related to a decrease in density of the material. The changes to the particle were found to be induced by the electron beam, as they only occurred in the scanned area and scaled with total electron dose, independent of dose rate. The observations were explained by electron beam induced breaking of chemical bonds in the silica matrix. In the initial stages of e-beam exposure, bonds in the high-density silica matrix were broken which led to the uptake of water into the structure by the formation of silanol groups, resulting in a decrease in material density and a corresponding increase in particle size. Prolonged e-beam exposure and further breaking of bonds led to parts of the silica matrix becoming completely disconnected and going into solution. This loss of material led to the gradual shrinking of the particle. Surprisingly, the shell remained spherical during these transformations, demonstrating that the silica matrix was capable of extensive internal restructuring in order to accommodate such plastic deformations. Furthermore, a particle with a broken shell also exhibited these changes, directly showing that these effects were not the result of differences between the particle interior and exterior. Additionally, particles became elongated along the scanning direction of the STEM probe. This occurred immediately and the effect was stronger at higher dose rate.

In **chapter 6**, the chemical reaction of magnesium oxide (MgO) with water to its hydroxide, Mg(OH)<sub>2</sub> was studied. MgO nanocrystals (NCs) were exposed to water vapor at ambient pressure and monitored at the single particle level in real time and real space by *in situ Transmission Electron Microscopy* (TEM). Upon exposure to both water vapor and the electron beam, MgO nanocrystals converted to amorphous Mg(OH)<sub>2</sub>. The reaction was observed to take place at the outer surface of the NC resulting in the formation of a Mg(OH)<sub>2</sub> layer around the MgO NC. As the reaction continued, the MgO-Mg(OH)<sub>2</sub> interface moved steadily inwards, consuming the MgO core and producing a thicker Mg(OH)<sub>2</sub> coating layer that extended beyond the particles original dimensions. The strength of the electron beam was varied and no reaction was found to take place below 70 electrons nm<sup>-2</sup> s<sup>-1</sup>. Above this threshold, the reaction rate of the hydration reaction was found to depend linearly on the dose rate. The electron beam irradiation is expected to have promoted the reaction through the generation of defects at the MgO{100} surface, thereby activating the MgO for hydroxylation and subsequently full hydration. The roughly linear relation between reaction rate and dose rate - as well as the dose rate threshold - could be explained by a surface defect formation mechanism.



---

# Samenvatting

---

Het werk dat uiteengezet is in dit proefschrift omvat synthese en bestudering van colloïdale deeltjes waarbij het dynamische gedrag geanalyseerd wordt op het niveau van individuele deeltjes. Wanneer deeltjes een karakteristieke afmeting hebben ruwweg tussen de nanometer ( $10^{-9}$  m) en micrometer ( $10^{-6}$  m) worden ze als ‘colloïdaal’ beschouwd. In dit regime zijn thermische fluctuaties voldoende om de deeltjes - en collecties van deeltjes - opnieuw onderling te rangschikken en zo een evenwichtssituatie te bereiken. Met behulp van *confocale laser scanning microscopy* worden de posities, bewegingen en onderlinge afstanden van de deeltjes geregistreerd. Door te kijken naar het gedrag van (collecties van) deeltjes kunnen eigenschappen van deeltjes achterhaalt worden en interactiepotentialen berekend worden. Daarnaast hebben we ook gebruik gemaakt van *elektronen microscopie* om colloïdale deeltjes te bestuderen, omdat hierbij een veel hogere resolutie te behalen valt. Hoewel het lange tijd slechts mogelijk was om materialen in droge toestand te bestuderen, is het sinds kort ook mogelijk om deeltjes in een vloeistof te bekijken met de elektronen microscoop. Echter, in tegenstelling tot de lichtbundel die bij optische microscopie wordt gebruikt om afbeeldingen te maken is de elektronenbundel van de elektronenmicroscoop alles behalve onschuldig. Vloeistoffen, en daarin gedispergeerde deeltjes, vertonen dan ook vaak verrassend gedrag ten gevolge van de bestraling met hoogenergetische elektronen.

In **hoofdstuk 2** wordt de syntheseprocedure van (fluorescente) silica bollen beschreven samen met een nieuwe methode om deze deeltjes over te brengen naar de relatief apolaire vloeistof cyclohexylchloride (CHC). Deze methode maakt gebruik van trimethylolpropaan ethoxylaat triacrylaat (ETPTA). Deze vloeistof kan relatief vrij van ionen worden gemaakt en valt niet uiteen in nieuwe ionen als deze wordt blootgesteld aan hoge-frequentie geluidsgolven in een ultrasoonbad. Bovendien kan ETPTA in combinatie met een fotoinitiator en UV licht worden gepolymeriseerd waarbij een groot volume van een dispersie in een oogwenk kan worden vastgezet. Een ander bijkomend voordeel aan deze nieuwe methode is dat er geen hydrofobe coating vereist is op de deeltjes. Er zijn verschillende manieren gebruikt om de (zeta) potentiaal van de deeltjes te meten. Deze potentiaal bleek niet af te hangen van de volumefractie. Echter, na 35 maanden (in

ethanol) opgeslagen te zijn geweest bleek de lading op de deeltjes significant lager te zijn geworden. Dit systeem is een stap in de richting van een experimenteel systeem van sterk afstotende silica nanodeeltjes die met behulp van UV licht vastgezet kunnen worden. Op die manier zal het mogelijk worden om de interactiepotentiaal tussen nanodeeltjes direct te meten.

De synthese van silica deeltjes with in **hoofdstuk 3** voortgezet een uitgebreid. Door tijdens de groeireactie een ‘*silane coupling agent*’ (SCA), N-[3-(trimethoxysilyl)propyl]ethyleendiamine (EDAPTMS), in te bouwen wordt een ander type silica gemaakt. Zulk organisch gemodificeerd silica (‘ormosil’) kan makkelijker worden verwijderd dan ‘puur’ silica door te etsen met waterstoffluoride (HF). Daarentegen etsen ormosil en puur silica even snel in loog. Er is getracht het verschil in gevoeligheid voor HF zo groot mogelijk te maken door een zo groot mogelijke hoeveelheid SCA in te bouwen, waarbij 25 mol% het maximum bleek. Door een laag ormosil te maken tussen een puur silica kern en buitenste schil, en deze ormosil laag vervolgens weg te etsen met HF, was het mogelijk om ‘*yolk-shell*’ deeltjes te maken, d.w.z. een fluorescent deeltje dat opgesloten zit in een schil waarbinnen deze nog enige bewegingsvrijheid heeft. In tegenstelling tot andere methodes die gebruik maken van hoge temperaturen om de tussenlaag te verwijderen blijft bij verwijdering met HF de fluorescente kleurstof intact. Het verwijderen van de tussenlaag met HF bleek op twee mogelijke manieren te verlopen. In sommige gevallen werd de laag even snel weggehaald vanaf alle kanten door de buitenste schil. In andere gevallen gebeurde dat vanaf één punt of lijn in de buitenste schil. Ook bleken ‘dumbbell’ deeltjes gevoeliger voor etsen met HF dan individuele bollen. Dit werd waarschijnlijk veroorzaakt door een dunnere/zwakkere silica schil in het gedeelte waar de twee bollen samen komen. Deze observaties geven aan dat de structuur van de buitenste silica schil behoorlijk kan variëren van deeltje tot deeltje en dat deze cruciaal is voor de manier waarop de deeltjes etsten.

Naast de verschillende snelheden waarmee ormosil en puur silica etsten in HF verschilden ze ook in hun lading. In neutraal medium was puur silica negatief geladen door de silanol groepen en zorgden de aminogroepen in de ormosil structuur juist voor een positieve lading. Een laagje van slechts enkele nanometers was al voldoende om de netto potentiaal om te doen slaan van  $-80$  naar  $+58$  mV. De lading van deeltjes met een ormosil laag en een buitenste laag van puur silica kon geleidelijk worden veranderd door licht met HF te etsen. Dit werd waarschijnlijk veroorzaakt doordat de ormosil laag langzaam beter toegankelijk werd, waardoor deze meer en meer bijdroeg aan de totaallading van het deeltje. Deze ladingsveranderingen vonden allemaal plaats voor er veranderingen in de morfologie van het deeltje optraden.

De deeltjes die in hoofdstuk 3 werden gesynthetiseerd zijn in **hoofdstuk 4** gebruikt om de diffusie te bestuderen van deeltjes in een sferische schil. De fluorescente deeltjes werden gemeten bij verschillende zoutcon-

centraties met confocale laser scanning microscopie en de afbeeldingen werden geanalyseerd met behulp van ‘*particle tracking*’ computer code. De beweging van de deeltjes bleek sterker vertraagd te zijn dan verwacht op basis van de hydrodynamische koppeling met de schil. Dit hangt waarschijnlijk samen met de elektrostatische afstoting. Daarnaast was ook de dracht van de elektrostatische repulsie langer dan verwacht. De diffusiesnelheid nam verrassend genoeg niet af als het deeltje dichtbij de muur bewoog.

In **hoofdstuk 5** wordt een dispersie van silica yolk-shell deeltjes bestudeerd met ‘*Scanning Transmissie Elektronen Microscopie*’ (STEM). De deeltjes zijn volledig verhard tot SiO<sub>2</sub> door ze te verhitten tot 900 °C alvorens ze te bestuderen. De deeltjes in water werden sterk beïnvloed door de elektronenbundel: eerst nam de diameter van de deeltjes met 10% toe, gevolgd door een gestage krimp. Dit gebeurde zowel voor het kern deeltje als voor de schil, hoewel de veranderingen van de schil zich sneller voltrokken. Dezelfde deeltjes die slechts tot 500 °C waren verhit - en daardoor een lagere dichtheid hadden - namen slechts 2-3% toe in afmeting voordat ze begonnen te krimpen. Dit duidt erop dat de initiële toename in grootte het gevolg was van een afname in dichtheid van het silica. De elektronenbundel bleek verantwoordelijk voor deze veranderingen, aangezien ze alleen optraden op de plekken waar de elektronenbundel scheen en recht evenredig schaalden met de elektronendosis, onafhankelijk van de sterkte van de bundel. Deze observaties konden worden verklaard door een verbreking van chemische bindingen in de silica structuur ten gevolge van de elektronenbestraling. In het begin van de bestraling, wanneer silica van een hoge dichtheid werd blootgesteld aan de elektronenbundel, werden chemische verbindingen verbroken wat leidde tot de opname van water door middel van de vorming van silanol groepen. Dit proces ging gepaard met een verlaging van de dichtheid en daarmee ook een uitzetting van het materiaal. Verdere bestraling met elektronen zorgde voor de verbreking van nog meer bindingen waarbij stukken van de structuur volledige los kwamen en in oplossing gingen. Hierdoor verloor het deeltje langzaam materiaal, wat resulteerde in een gestage krimp. Verrassend genoeg bleef de schil gedurende deze transformaties sferisch. Dit getuigt ervan dat de interne structuur van de silica matrix in staat is tot verregaande herstructurering om zulke plastische deformaties te kunnen ondergaan. Een deeltje waarbij een deel van de buitenste schil afgebroken was vertoonde dezelfde verschijnselen, waaruit af te leiden valt dat een verschil in de ruimte binnen en buiten het deeltje niet ten grondslag lag aan de observaties. Daarnaast rekte de deeltjes uit in scanrichting van de STEM bundel. Dit gebeurde direct en de uitrekking werd langer bij sterkere bundels.

De chemische reactie van magnesiumoxide (MgO) met water tot de hydroxide, Mg(OH)<sub>2</sub>, werd bestudeerd in **hoofdstuk 6**. MgO nanokristallen (NCs) werden blootgesteld aan waterdamp bij atmosferische druk en hun omzetting werd gevolgd op het niveau van individuele deeltjes door middel van *in situ Transmissie Elektronen Microscopie* (TEM). Wanneer

MgO NCs omgeven waren door waterdamp en tegelijkertijd beschenen werden met elektronen zetten ze om naar amorf  $\text{Mg}(\text{OH})_2$ . Deze reactie vond plaats aan het oppervlak van de NCs waardoor er een laag  $\text{Mg}(\text{OH})_2$  ontstond rondom het deeltje. Naarmate de reactie vorderde bewoog het  $\text{MgO-Mg}(\text{OH})_2$  grensvlak naar binnen, waarbij de MgO kern verdween en plaatsmaakte voor een groeiende laag  $\text{Mg}(\text{OH})_2$  die zich verder uitstreekte dan de originele afmetingen van het deeltje. De sterkte van de elektronenbundel was van invloed op de reactie: bij bundelsterktes lager dan  $70 \text{ elektronen nm}^{-2} \text{ s}^{-1}$  vond er geen reactie plaats terwijl daarboven de reactie recht evenredig was met de bundelsterkte. Naar verwachting heeft de elektronenbundel de reactie bevordert door defecten te creëren op het  $\text{MgO}\{100\}$  oppervlak en hiermee het oppervlak te hebben geactiveerd voor verdere hydroxylering en uiteindelijk volledige omzetting. Zowel de minimaal benodigde sterkte van de elektronenbundel als de recht evenredige afhankelijkheid van de bundelsterkte met de reactiesnelheid konden worden verklaard met een mechanisme van bundelgeïndiceerde defecten op het MgO oppervlak.

---

# Acknowledgments

---

Een promotietraject is niet zomaar iets. Het is een intensief proces met pieken en dalen waarbij je hoe dan ook jezelf zult tegenkomen. Ik heb ontzettend veel geleerd, genoten van internationale congressen, vriendschappen gemaakt die mij zeer dierbaar zijn en in alle heerlijke vrijheid fundamentele wetenschap mogen bedrijven. Zelfs had ik het voorrecht om twee internationale reizen te organiseren waar ik fantastische herinneringen aan heb. Daarnaast waren er ook tijden waarop ik het zwaar had. Op die momenten heb ik kunnen vertrouwen op de steun van veel mensen om mij heen, waardoor ik er toch doorheen gekomen ben. Zonder al deze anderen had ik het niet gekund. Bij deze wil ik een aantal mensen bedanken, voor de geweldige periode van groei, plezier en ontwikkeling, en voor de momenten waarop ik bijgestaan ben bij het halen van de eindstreep.

Allereerst wil ik mijn promotor, Alfons van Blaaderen, bedanken voor de mogelijkheid om mijn promotieonderzoek uit te voeren in zo'n geweldige groep. Jouw inzicht in waar mogelijkheden liggen voor vernieuwend onderzoek is inspirerend en zorgt er bovendien voor dat wij beschikking hebben over hypermoderne apparatuur. Je hebt ongelooflijk veel kennis paraat, en ik word dan ook continu verbaasd door zowel jouw kennis van de vakliteratuur als van ontzettend veel onderwerpen die niets met ons werkveld te maken hebben. Ik heb in de laatste jaren enorm veel van je geleerd, zowel inhoudelijk als over wetenschap en onderzoek in het algemeen, als ook over mijzelf. Dank je wel.

Daarbij wil ik ook mijn copromotor, Marijn van Huis, bedanken voor alle hulp, adviezen en zelfs praktische ondersteuning bij het solderen van kleine contactjes aan nog veel kleinere draadjes. Dank je wel dat je mij kennis hebt laten maken met liquid cell TEM. Ik had vooraf niet verwacht dat het zo'n belangrijk onderdeel van mijn proefschrift zou worden, maar ik ben blij dat het zo gelopen is.

Ik wil ook Marjolein Dijkstra bedanken voor haar waardevolle input. Ik heb veel profijt gehad van jouw uitgebreide kennis over interacties van deeltjes en van statistische fysica. Dank je wel voor je wetenschappelijke input, voor het bevorderen van sociale interacties en samenwerking binnen onze groep en voor steun in moeilijke tijden. Hierbij wil ik ook de rest van de wetenschappelijke stafleden, Arnout Imhof, Laura Filion, Patrick Baesjou en Krassimir Velikov, bedanken voor het creëren van een

zeer diverse vakgroep, het stimuleren van erg goed onderzoek en voor het tot stand brengen van een sfeer van collaboratie en collegialiteit. Hans Gerritsen, Gerhard Blab, Dave van den Heuvel en Jantina Fokkema van de Biophysics groep, jullie wil ik ook bedanken voor de wetenschappelijke discussies, (bokbier)borrels en voor de altijd gezellige koffiepauzes. Additionally, I'd like to thank Gerhard for the use of the 3D printer and his appreciation of quality coffee. Daarbij wil ik ook René van Roij, Bram Bet en Mathijs Janssen van het Instituut voor Theoretische Fysica zeer bedanken voor de prettige en verhelderende gesprekken over alle onderliggende theoretische aspecten. Peter Helfferich, hartelijk bedankt voor alle hulp met alles wat met computers, programma's en netwerken te maken heeft. Ik ben Relinde Moes-van Dijk en (gedeeltelijk) Fabian Hagemans zeer dankbaar voor het in goede conditie houden van onze labs. Dit is een soms vervelende en lastige klus die bovendien nooit ophoudt en maar weinig lof krijgt. Toch ben ik er zeker van dat ik voor alle experimentalisten spreek als ik zeg dat ik blij en dankbaar ben dat jullie het doen. Chris Schneijdenberg en Hans Meeldijk, het onverslaanbare burmanteam dat beter is dan wel tien verre vrienden. Ik wil jullie graag bedanken voor alle hulp en morele steun als de liquid cell weer eens... nou ja, de liquid cell was. Voor de snoepjes, gezellige gesprekken, koffiekaart, het terughalen van de bundel als die weer eens in Bunnik stond en voor de fantastische ondersteuning met alles omtrent de microscopen. Wij zijn rijk met jullie. Ook wil ik graag Thea Pozzi, Marion Wijburg, Dianne Ickenroth en Hester van der Putte bedanken voor alle administratieve ondersteuning. Dank jullie wel voor al het werk dat wij nooit te zien krijgen en waar wij desalniettemin veel profijt van hebben. Judith Wijnhoven, ik heb veel gehad aan jouw steun. Ik heb mogen profiteren van jouw kennis en ervaring van silica synthese en van ondersteuning met experimenten en ander praktisch werk. Ik heb altijd met veel plezier met je samengewerkt en steun aan je gehad, daar ben ik je ontzettend dankbaar voor. Het voelt als een groot gemis dat je er nu niet bij bent.

Ik ben Stichting FOM enorm dankbaar voor alle mogelijkheden, trainingen en ondersteuning. In het bijzonder Lydia van der Vlist en Maria Teuwissen, dank jullie wel voor de hulp en altijd razendsnelle respons. Harry Linders, jij bedankt voor je hulp en inzicht. Ik heb ontzettend veel geleerd van mijn tijd in de centrale ondernemingsraad. Ik ben heel dankbaar dat ik de mogelijkheid heb gekregen om deze kant van mijzelf te ontwikkelen en nieuwe vaardigheden op te doen in een prettige omgeving. Sjoerd, Veer, Leo, Gerben, Han, Ben, Joost, Paula, Monique, Christiaan, Maarten, Marieke, Nadine, Niels, Johan, Jan Just en natuurlijk Ineke, bedankt voor de fijne en leerzame tijd. Heel erg bedankt voor jullie vertrouwen in mij als voorzitter. Win van Saarloos en Renée-Andrée Koornstra, jullie beide ook enorm bedankt voor de prettige samenwerking. Ik heb veel van jullie geleerd.

Ook wil ik hier Huub Biessels, van het practicum van de bachelor

Scheikunde, enorm bedanken voor het aanwakkeren van mijn enthousiasme voor experimenteel onderzoek in het begin van mijn opleiding. Ik had het geluk om nog van jou les te krijgen. Daarbij heb ik zowel inhoudelijk veel geleerd als gemerkt hoe leuk experimenteel werk kan zijn. Jouw altijd vriendelijke en positieve uitstraling zijn dingen waar ik tot op de dag van vandaag nog aan terugdenk.

I'm grateful to all of the SCM group members over the years for creating a pleasant atmosphere and stimulating work environment. Therefore, I'd like to thank the past groups members Bart, Thijs, Anjan, Marlous, John, Zdenek, Johan, Nina, Simone, Henriette, Guido, Wiebke, Nick, Harini, Vasillis, and all of the current members, who have become too numerous to list. I have benefited from the advice and expertise of many of you, and you have been a tremendous help throughout. Thank you all for the assistance and support, ever-enjoyable coffee breaks, dinners at work, and a deep feeling of companionship. I'm thankful to have worked in such a social and supportive group. And of course, thank you all for the essential relaxation provided by the foosball games, in particular for the high-quality A-league games. Of all my skills, this is probably the one that has improved the most throughout my PhD! Additionally, I would like to thank all the experimentalists who welcomed me with a smile and a wave from inside the lab when I was walking up to our building in the morning; it made all the difference.

Much of the time at work was spent in the office, and I have been very fortunate to have had such fantastic office mates: Jissy, Johan, Nina, Henriette, Jessi, Pepijn, and Anna. Thank you for putting up with the daily coffee grind and the continual foot traffic caused by the cookie bucket. Johan, het was heerlijk om met jou het kantoor te delen. Zeker in het begin had ik heel veel vragen waarvoor ik altijd bij jou terecht kon. Vaak kreeg ik dan direct het antwoord, of anders in ieder geval goed advies. Heel erg bedankt. Nina, Henriette en Jessi: de power-vrouwen van het OL. Ik ben altijd van jullie onder de indruk. Jullie zijn toonbeelden van doorzettingsvermogen, er altijd keihard voor gaan en toch dicht bij jezelf blijven. Ik ben jullie ontzettend dankbaar voor de steun in moeilijke tijden, voor de aanmoediging en voor de gezelligheid. Anna, thank you for nice chats, cookies, sweets, and for being an all-round nice office mate. It's a shame we shared the office only briefly. Pepijn, je bent er niet vaak, maar als je er bent is het altijd direct gezellig. Ik heb genoten van het samen bespreken en uitleggen van intrigerende metingen en van je aanstekelijke enthousiasme over het bedrijven van wetenschap en bedenken van nieuwe ideeën.

I'm deeply grateful to my Master student, Chiara Raffaelli, for all her hard work which led to chapter 3, and indirectly also to chapter 4. I was fortunate that you chose to do your project in our group. You were a pleasure to work with, and I have learned much from being your supervisor. Simone, thank you for your advice, critical attitude and friendship. It has been a pleasure to experience (and be the object of) your drive, keen

observations and quick wit. Thank you for all the encouragement and for your streng maar rechtvaardig urging on. Vasillis, my Peripatetic friend. I'm very grateful for our regular excursions. You have had a tremendous influence on my all-round personal development. I've learned a great deal from our conversations and adventures and I hope there will be many more. Wiebke, thank you for your help with many things over the years, from physics to theses to life stuff. You've supported me greatly with organizing social events and other extracurricular activities. I had a great time with you at EMAT, for which I'd also like to thank Da. Fabian (andere gedeelte), bedankt voor de prettige samenwerking m.b.t. de silica synthese. Het was fijn om op het lab of in de wandelgangen met je te overleggen, experimenten af te stemmen, en dat je zo nu en dan een TEM gridje voor me mee kon nemen. Naveed, thank you for the constant positivity.

Ik ben gezegend met een ontzettend fijne en trouwe vriendenkring waar ik de laatste jaren meermaals op terug heb kunnen vallen. Jessica, bedankt voor de hulp en belangstelling door de jaren heen. Als het zwaar was kon ik altijd bij je terecht. Tjaard, de spelletjesmiddagen/-avonden die jij organiseerde waren momenten waarop ik altijd weer even op kon laden. Dank je wel voor je interesse en vriendschap. Pepijn en Marieke, ik ben jullie beide heel erg dankbaar voor jullie steun en voor het faciliteren van luchtige ontspanning. Als ik van jullie vandaan weer naar huis ging kon ik er weer een tijdje tegenaan. Anniek, ik geniet altijd enorm van onze gesprekken. Jouw nuchtere en kritische blik werkt relativerend en plaatst de zaken in perspectief juist wanneer dat nodig is. Dank je wel. Anna en Dennis, hartelijk bedankt voor de ontzettend fijne ontbijtjes op zondag en voor de onvoorwaardelijke steun en interesse. Willem-Rein, dank je wel voor het stimuleren van de zoektocht naar goede koffie, waar die ook vandaan moge komen. Jasmijn, Andreas, Luc, Vincent, Daniël, Ido, Danielle, Arjen, Judith, Thomas, Liselotte, Rogier, jullie allemaal heel erg bedankt voor de ontspanning, gezelligheid, spelletjes en steun gedurende al de jaren. Ik reken mijzelf rijk met jullie als mijn vrienden. Ook wil ik graag mijn huisgenootjes Eva, Alice, Annemiek, Karolien, Aron, Carolina en Anne bedanken. De vele huisetentjes, brakke brunches in de tuin, en algemene gezelligheid in huis over de jaren hebben mij goed gedaan. En Aron, bedankt voor je hulp bij het ontwerpen van de cover!

Ik ben bijzonder dankbaar voor de steun van mijn paranimfen Ernest en Lydia. Ernest, dank je wel voor de fijne samenwerking, adviezen, dumbbell annihilator, openheid en vriendschap. Wat er ook was, ik kon bij je terecht. Als ik weer eens een vraag had of graag leuke resultaten aan iemand kwijt moest was je altijd beschikbaar. Ik liep dan ook geregeld bij jullie naar binnen. Het kwam dan ook goed uit dat je in het kantoor direct naast dat van mij zat. Ik heb met veel plezier vastgesteld dat het laatste jaar dat verkeer ook vaker de andere kant op was en ik jou van dienst kon zijn. Ik had me geen fijnere kamergenoot kunnen wensen als we op inter-

nationale congressen een hotelkamer deelden, waar we vrijwel iedere avond onze slaap opofferden om tot diep in de nacht maatschappelijke zaken te bespreken. Lydia, bedankt voor de benodigde ontsnapping aan de werkdruk in de vorm van fietstochtjes, wandelingen en terrasbezoeken waarbij het altijd gepaard ging met lekker eten (en soms zelfs alleen maar bestond uit lekker eten). Ik heb veel gehad aan al onze gesprekken en zelfreflectie. Heel erg bedankt.

Lieve papa en mama, ik ben jullie ongelofelijk dankbaar voor de onvoorwaardelijke steun en liefde. Voor het voeden van mijn nieuwsgierigheid en om niet bang te zijn om anders te zijn. Al sinds de middelbare school hebben jullie mij de vrijheid gegeven om mijn eigen weg te vinden en altijd klaargestaan om me aan te moedigen. Hoewel ik mijn onderzoek niet altijd volledig helder uit kon leggen luisterde jullie altijd geïnteresseerd naar de laatste ontwikkelingen. En als jullie iets wetenschappelijk interessants gelezen hadden werden voor mij de krantenknipsels bewaard. Jullie hebben de moeilijke balans tussen loslaten en betrokkenheid goed weten te vinden, waardoor ik mij immer vrij en toch geborgen heb gevoeld. Eva, lieve zus, Jij hebt deze paden allemaal al bewandeld. Hierdoor heb ik al jaren een beetje van je kunnen afkijken en kon ik mijn PhD perikelen direct bij je kwijt waarbij ook een half woord voldoende was. Je bent mijn grote voorbeeld, en ik zou me geen betere zus kunnen wensen.



---

# List of publications

---

This thesis is partly based on the following publications:

- W. Vlug, C. Raffaelli, and A. van Blaaderen, *Synthesis of oppositely charged colloidal silica and yolk-shell particles*, manuscript in preparation (chapter 3)
- W. Vlug, C. Raffaelli, and A. van Blaaderen, *Diffusion of colloidal particles in spherical shells*, manuscript in preparation (chapter 4)
- W. Vlug, S. Sadighikia, K. Watanabe, D. Nagao, M. van Huis, and A. van Blaaderen, *Beam induced dissolution of silica in liquid cell Scanning Transmission Electron Microscopy*, manuscript in preparation (chapter 5)
- W. Vlug, O. Plmper, M. Kandianis, A. van Blaaderen, and M. van Huis, *Hydration of MgO Nanocrystals to  $\alpha$ -Mg(OH)<sub>2</sub> Monitored at Ambient Pressure by In Situ Transmission Electron Microscopy*, manuscript in preparation (chapter 6)

Other publications by the author:

- F. Hagemans, W. Vlug, C. Raffaelli, A. van Blaaderen, and A. Imhof, *Sculpting Silica Colloids by Etching Particles with Nonuniform Compositions*, *Chem. Mater.*, 29 (7), 3304-3313, 2017 (chapter 3)
- D. J. Kraft, W. S. Vlug, C. M. van Kats, A. van Blaaderen, A. Imhof, and W. K. Kegel, *Self-Assembly of Colloids with Liquid Protrusions*, *JACS*, 131 (3), 1182-1186, 2009



---

# About the author

---

Wessel Vlug was born on September 23<sup>rd</sup>, 1985 in Amsterdam, the Netherlands. In 2004, he graduated from the Pieter Nieuwland College (VWO, Atheneum) and started studying Chemistry at Utrecht University that same year. He obtained his bachelor's degree with a minor "Nanomaterials" in 2007 after completing his bachelor's project at the Soft Condensed Matter group entitled "Colloidal PMMA dumbbells" under supervision of Prof. dr. Alfons van Blaaderen and Carlos van Kats. In 2007, he enrolled in the master's program "Nanomaterials: Chemistry & Physics" at Utrecht University. He performed his research at the group Inorganic Chemistry and Catalysis, under supervision of Prof. dr. ir. Bert Weckhuysen and dr. Andrew Beale, resulting in a thesis titled "Ionothermal synthesis of AlPOs." As part of the master's degree, he spent a year studying abroad at UC Berkeley, USA, with Prof. dr. Gabor Somorjai, writing a thesis entitled "Nanoparticles and supports for heterogeneous catalysis." In March 2012, he started his PhD project at Utrecht University in the Soft Condensed Matter group under the supervision of Prof. dr. Alfons van Blaaderen and dr. Marijn van Huis, the results of which are described in this thesis. His research focused on the synthesis of (nano)particles and studying these particles in real space using confocal and electron microscopy. In line with his research, he made use of an emerging technique which enables particles to be studied in the electron microscope while they are dispersed in a liquid. Aside from conducting research, he was the chairman of the Central Works Council of Stichting FOM for two years, representing the interests of all its employees, roughly half of which were other PhD candidates.